THÈSE

Présentée pour obtenir
LE GRADE DE DOCTEUR EN SCIENCES
DE L'UNIVERSITÉ PARIS-SUD XI

École Doctorale de Physique de la Région Parisienne

avec

INSTITUT DE PHYSIQUE THÉORIQUE DU CEA

Spécialité: Physique théorique

par

Ekaterina Retinskaya

soutenue publiquement le Mardi 10 juin 2014

Reverse engineering of heavy-ion collisions: Unraveling initial conditions from anisotropic flow data

Composition du jury

Rapporteurs:	Prof. Piotr Bozek
	Prof. Urs Wiedemann
Examinateurs:	Prof. Bruno Espagnon
	Dr. Boris Hippolyte
Directeur de thèse:	Dr. Jean-Yves Ollitrault

Thèse préparée à
l’Institut de Physique Théorique
Commissariat à l’énergie atomique et
aux énergies alternatives,
Orme des Merisiers bâtiment 774
Point courrier 136
CEA/DSM/IPhT, CEA/Saclay
F-91191 Gif-sur-Yvette Cedex

To my family...

Remerciements

Je voudrais commencer par remercier mon directeur de thèse Jean-Yves Ollitrault. Merci pour ton soutien pendant ces trois années passées, pour ta gentillesse et ta patience, merci de m'avoir appris beaucoup de choses. Pendant ces trois années chaque minute je pouvais venir dans ton bureau pour poser des questions stupides et t'as toujours eu des bonnes réponses, tu n'es pas que un très bon chercheur mais aussi un très bon directeur de thèse, très pédagogique et attentif, j'ai eu vraiment de la chance d'être prise au CEA sous ta direction. Merci aussi pour nos discussions à propos de la vie, je ne vais pas oublier aussi notre voyage en Bretagne en voiture chez toi avec Adrien, Li et Daniel. Merci aussi pour toutes les conférences qu'on a fait ensemble et je ne vais pas oublier comment on a couru ensemble a l'aéroport de Madrid pour avoir notre avion. Merci aussi pour le concert de la musique classique à Paris. J'espère aussi d'entendre comment tu jous du piano encore une fois de plus.

Merci à Piotr Bozek et Urs Wiedemann pour avoir accepté d'être mes rapporteurs de thèse ainsi que les membres de mon jury Bruno Espagnon et Boris Hippolyte pour le travail qu'ils ont fait en lisant ma thèse et pour les questions très intéressantes et profondes qu'on a discuté pendant ma soutenance de thèse.

Merci aux membres du groupe de QCD pour les discussions scientifiques et journal club qui m'a permi d'apprendre un peu dans de nouveaux domaines. Merci pour m'avoir donné la possibilité de voyager en conférences. Merci à Jean-Paul Blaizot, Edmond Iancu, Francois Gelis, Grégory Soyez, Robi Peschanski, Mattew Luzum, Yacine Mehtar-Tani, Fabio Dominguez, Bin Wu, Li Yan, Leonard Fister, Jose Madrigal, Javier Albacete, Jihun Kim, Thomas Epelbaum, Piotr Warhol, Daniel Kroff Fogaga et Manoel Rodriguez.

Merci aussi à Hervé Moutarde, Franck Baj et Jean-Yves pour leurs aides précieuse dans la recherche d'un futur poste.

Merci à touts les participants de nos rencontres d'ions lourds de région parisienne dont j'ètais l'organisatrice pendant 1 an et demi ensemble avec Igor Lakomov et Nicolas Filipovic, qui je remercie pour l'aide et bon travail en equipe.

Je remercie le directeur de l'IPhT Michel Bauer pour m'avoir accueilli au laboratoire et m'avoir donné la possibilité d'apprendre le français au CNRS et pour la formation en neutronique au CEA. Merci aux résponsables des thésards Olivier Golinelli et Stéphane Nonnenmacher pour les discussions et conseils très utils. Un grand merci pour l'équipe administrative : Sylvie Zaffanella, Catherine Cataldi, Laure Sauboy, Anne Capdepon, Morgane Moulin, Emilie Quéré, Loic Bervas et Emmanuelle De Laborderie; Merci à nos "IT": Patrick Berthelot, Philippe Caresmel, Pascale Beurtet et Laurent Sengmanivanh. Vous êtes toujours sur place pour répondre à nos problèmes immédiatement, toujours avec le sourire, très attentifs, un grand merci pour ça.

Je remercie mes professeurs russes de l'université de Moscou pour m'avoir fait découvrir et aimer la physique.

Merci à mes parents, ma maman et son soutient qui m'a permie de recevoir l'éducation la plus haute possible en Russie et merci a toi, papa, même si tu n'es plus avec nous, je sais que tu serais fier de moi, ton "petit boson", maintenant. Merci à ma soeur Olga, docteur en biologie, pour l'inspiration de faire la science et aussi à mes trois neveux pour l'amour et soutient durant ces années, même si on se voit pas très souvent.

Merci à mon chéri, mon futur mari Adrien, pour ces 3 heureuses années ensemble, merci pour tout, c'est grâce à toi que je découvre beaucoup de choses : ce pays qui devient ma deuxième maison, la nouvelle langue, les sports, la musique, la cuisine éxotique et encore beaucoup de choses. Je sais que j'aurais toujours ton soutien dans touts les moments de ma vie. C'est un grand merci pour chaque jour que t'es à mes cotés. Et bien sûr merci pour avoir relu ma thèse et mes remerciements.

Pendant ces trois années en France j'ai eu de la chance de rencontrer beaucoup de gens très intéressants et trouver beaucoup d'amis.

Premièrement merci à mes amis "le barbu" Axel, "le dieu" Antoine et "général malin" Benjamin pour ces jours passés ensemble chez nous, et en voyages à Prague, en Suisse, en Dordogne et au Pays Basque. Merci à mes chers voisins du 2ème Olga et Gabriel, c'est en grand partie grâce à vous que je suis en France maintenant et que j'ai rencontrè mon Adrien. Merci pour les journées de bonheurs ensemble, pour votre disponibilité et votre infaillible soutien pendant toutes ces années depuis CERN Summer Student School 2009 ou on c'est rencontrè. Merci à mes amis pour une grande surprise qui m'attendait chez moi le soir après la soutenance, mon petit chaton Albert Einstein (Al), qui Adrien préfère appeler Attila et on sait pourquoi. Merci à mes amis Hanna, Pierre, Sasha, Igor, Jérémie et Galina, Ramuntxo et Inaki pour tous les moments et soirées passées ensemble. Merci aussi à toi Sébastineau. Merci à Bertrand pour nous avoir supporté pendant deux années de colocation, j'espère que tu auras des colocataires plus calmes à Jyvaskyla. Merci à Maxime pour m'avoir éviter les problèmes de RER cette année et m'avoir tout appris sur les sections efficaces de pions pendant les trajets fait en covoiturage ensemble.

Merci aux thésards de l'IPhT, c'était vraiment l'atmosphère très chalereuse pendant nos déjeuners. Merci à mes co-bureaux Romain, Nicolas, Thomas et Andrey pour m'avoir supporté. Surtout à Thomas qui s'est retrouvé enfermé avec deux russes bavardes. Merci à mes co-déjeuners Piotr (le papi de thésards, toujours avec ses blagues), Alexandre (le barbu qui mange beaucoup de desserts et qui aime bien les blagues de Piotr), Benoît (qui aime bien faire des cicatrices en rugby et toujours rigolo), Antoine (avec son vélo sous la pluie et sushi aux baconnets jusqu'à explosion du ventre), Jérôme (toujours à la mode), Rémi (avec un accent parfaitement anglais), Julien (avec son sens de l'humour à lui), Thiago (avec sa moto en compétition avec la voiture de Julien), Eric (avec ces apparitions inattendues dans le bureau de Benoît), Junfeng (avec son "kak sam" en russe sans accent), Hélène (qui a demenagé chez les astronautes), Guillaume (qui vient parfois quand il ne fait pas de trucks de bio) et Raphael (qui vient aussi parfois), nos stagaires Francesca, Mathilde et Somya et d'autres encore pour une bonne ambiance et pour des histoires toujours rigolotes et discussions intéressantes, c'était un véritable plaisir de rencontrer les gens comme vous. Merci aussi aux autres thésards que je n'ai pas eu la chance de mieux connaître.

Merci et bonne continuation à vous tous vous allez me manquer!

Katia

Acknowledgments

I'd like to start my acknowledgments by my PhD advisor Jean-Yves Ollitrault. I thank you for your support during all three years passed, for you kindness and patience, thank you for teaching me all I know now. During these three years each minute I could come to your office and ask stupid questions and you always had good answers, you are not only a very good researcher, but also a good advisor, very pedagogic and attentive. I was really lucky to be offered the PhD position under your guidance. Thank you also for our discussions about life, I will not forget also our trip to Bretagne by car to your house with Adrien, Li and Daniel and thank you also for the concert of classical music in Paris. I also hope to hear how you play piano one more time.

I thank Piotr Bozek and Urs Wiedemann for accepting to be the reporters of my thesis together with the members of the defence committee Bruno Espagnon and Boris Hippolyte for the huge work that they have done by reading my thesis and for very interesting and profound questions which were discussed during my defence.

Thank you to the members of QCD group of IPhT for the scientific discussions during Journal Clubs which allowed me to learn new fields of physics. Thank you for giving me the opportunity to travel to numerous conferences. Thank you to Jean-Paul Blaizot, Edmond Iancu, Francois Gelis, Grégory Soyez, Robi Peschanski, Mattew Luzum, Yacine Mehtar-Tani, Fabio Dominguez, Bin Wu, Li Yan, Leonard Fister, Jose Madrigal, Javier Albacete, Jihun Kim, Thomas Epelbaum, Piotr Warhol, Daniel Kroff Fogaga et Manoel Rodriguez.

Thank you to Hervé Moutarde, Franck Baj and Jean-Yves for their help in the research of the futur job.

Thank you to all the participants of our "heavy-ion meetings" which I was organising for one year and a half together with Igor Lakomov and Nicolas Filipovic, whom I thank a lot for their help and our work in team.

I thank the director of IPhT Michel Bauer for welcoming me at the IPhT and for giving me a possibility to learn French at CNRS and to participate in the nuclear engineering school of CEA. Thank you to the responsible for the PhD students Olivier Golinelli and Stephane Nonnenmacher for their discussions and very useful advices. A big thank you to the administrative team: Sylvie Zaffanella, Catherine Cataldi, Laure Sauboy, Anne Capdepon, Morgane Moulin, Emilie Quéré, Loic Bervas et Emmanuelle De Laborderie; Thank you to our

"IT" team: Patrick Berthelot, Philippe Caresmel, Pascale Beurtet et Laurent Sengmanivanh. You all are always on your place to immediately help us with our problems, always with smile, very attentive, thank you all a lot for this.

I thank my Russian professors from Lomonosov Moscow State University for teaching me how to study and love physics.

Thank you to my parents, my mom and her support which allowed me to get the best eduction possible in Russia, thank you also to you, papa, even if you are not any more with us, I know that you would be proud of me, your "small boson", now. Thank you also to my elder sister, PhD in biology, for inspiring me to do science and to her three children, my nephews for their love and support during their years, even if I do not come so often to Moscow.

Thank you to my dear, my future husband Adrien, for these three happy years together, thank you for all, it is thanks to you that I discover a lot of new: this country which becomes my second home, a new language, different sports, music, exotic food and a lot of other things. I know that I will always have your support in all the moments of my life. Thank you for each day that you are with me. And of course thank you for reading my thesis and these acknowledgements.

During these three years in France I was lucky to meet a lot of interesting people and to find a lot of friends. At first I thank my friends "le barbu" Axel, "le dieu" Antoine and "general malin" Benjamin for our trips together to Praha, Basque country, to Dordogne, skiing in Switzerland and for all the days passed together at our home. Thank you to my dear neighbours from the second floor Olga end Gabriel, it's partly thanks to you that I am now in France and that I have met my Adrien. Thank you for all happy days together for you availability and your support for these years starting from CERN Summer Student School 2009 where we have met. Thank you to my friends for the big surprise which was waiting for me the evening after my defence, small kitten Albert Einstein (Al) which Adrien prefer to call Attila and we know why. Thank you to my friends Hanna, Pierre, Sasha, Igor, Jeremie and Galina, Ramuntxo and Inaki for all the moments together. Thank you also to you, Sebastineau. Thank you to our neighbour Bertrand for tolerating us for two years, I hope you will have less noisy neighbours in Jyvaskyla. Thank you to Maxime for the opportunity to avoid problems of RER this year and teaching us about cross-sections of pions during our root together in carpooling.

Thank you to the PhD students of IPhT, it was really a warm atmosphere during our lunches together. Thank you to my co-office Romain, Nicolas, Thomas and Andrey for the patience. Expecially to Thomas who has found himself enclosed with two talkative russians at the same time. Thank you to my co-lunchers Piotr (the grandpa of the students, always with his jokes), Alexandre (bearded, who likes a lot to eat several deserts and who likes a lot the jokes of Piotr), Benoît (who likes to get cuts in rugby and who is always funny), Antoine (always with his bike even under the rain and with sushi aux baconnets until the explosion of the stomach), Jérôme (always chic), Rémi (with his perfect british accent), Julien (with this sense of humour of him), Thiago (with his moto competing with the car of Julien), Eric (with unexpected appearances in the office of Benoît), Junfeng (with his perfect Russian "kak sam" without any accent), Hélène (who moved from us to the astronauts), Guillaume (who appears sometimes in IPhT when he is not doing biology stuff) et Raphael (who also appears sometimes), our internship students Francesca, Mathilde and Somya for a good company and a lot of others for the good ambience, funny stories and interesting discussions, it was a real pleasure for me to meet you all. Thank you also to other students whom unfortunately I did not have a chance to know better.

Thank you and good luck to you all, I will miss you.

Katya

Abstract

Ultra-Relativistic heavy-ion physics is a promising field of high energy physics connecting two fields: nuclear physics and elementary particle physics. Experimental achievements of the last years have provided an opportunity to study the properties of a new state of matter created in heavy-ion collisions called quark-gluon plasma.

The initial state of two colliding nuclei is affected by fluctuations coming from wave-functions of nucleons. These fluctuations lead to the momentum anisotropy of the hadronic matter which is observed by the detectors. The system created in the collision behaves like a fluid, so the initial state is connected to the final state via hydrodynamic evolution. In this thesis we model the evolution with relativistic viscous hydrodynamics. Our results, combined with experimental data, give non trivial constraints on the initial state, thus achieving "reverse engineering" of the heavy-ion collisions.

The observable which characterizes the momentum anisotropy is the anisotropic flow v_n. We present the first measurements of the first harmonic of the anisotropic flow called directed flow v_1 in Pb-Pb collisions at the LHC. We then perform the first viscous hydrodynamic modeling of directed flow and show that it is less sensitive to viscosity than higher harmonics. Comparison of these experimental data with the modeling allows to extract the values of the dipole asymmetry of the initial state, which provides constraints on the models of initial states. A prediction for directed flow v_1 in Au-Au collisions is also made for RHIC. We then perform a similar modeling of the second and third harmonics of the anisotropic flow, called respectively elliptic v_2 and triangular v_3 flow. A combined analysis of the elliptic and triangular flow data compared with viscous hydrodynamic calculations allows us to put constraints on initial ellipticity and triangularity of the system. These constraints are then used as a filter for different models of initial state. At the end of this thesis, we show perspectives in the studies of the initial state which are opened by recent measurements of event-plane correlations which could shed light on the initial state fluctuations.

Key words: *anisotropic flow, relativistic heavy-ion collisions, relativistic viscous hydrodynamics, initial state, event-plane correlations.*

Contents

List of Figures

List of Tables

Chapter 1

Introduction

1.1 Experimental overview

The story of heavy-ion collisions starts with the pioneering works of Enrico Fermi and Lev Landau on the hot matter and multi particle production in the 50's. Theoretical works motivated the experiments and in the 70's the first experiments on heavy-ion collisions were done at Berkeley in LBNL and at Dubna in JINR, where the first studies of compressed and excited matter were done. The further research programs at higher energies were launched in the 80's in Brookhaven and at CERN. In the 90's "beam-target" experimental high energy collisions were run in Brookhaven (AGS, gold beams on gold target) and at CERN (SPS, lead beam on lead target and later uranium beam on uranium target). In 2000, the first "beam–beam" heavy ion collider RHIC (The Relativistic Heavy Ion Collider) started to run in Brookhaven, opening a new era in the experimental studies of heavy-ion physics. Nowadays, RHIC and LHC (The Large Hadron Collider) located in CERN, constitute the two relativistic heavy ion colliders. The main heavy ions which are used in these colliders are respectively gold and lead ions.

1.1.1 RHIC

Launched in 2000, RHIC has provided a lot of important results on the study of matter created in the relativistic heavy-ion collisions [21, 22, 23]. Thus it was found out that this matter is behaving more like a strongly coupled liquid than a gas as it was considered earlier [24, 25].

RHIC is designed to collide AuAu nuclei with a center-of-mass energy of 200 GeV per nucleon pair. During the first year of running this energy was not achieved, and the first runs were made at the energy 130 GeV. Later during several years RHIC was running with designed energy of 200 GeV per nucleon

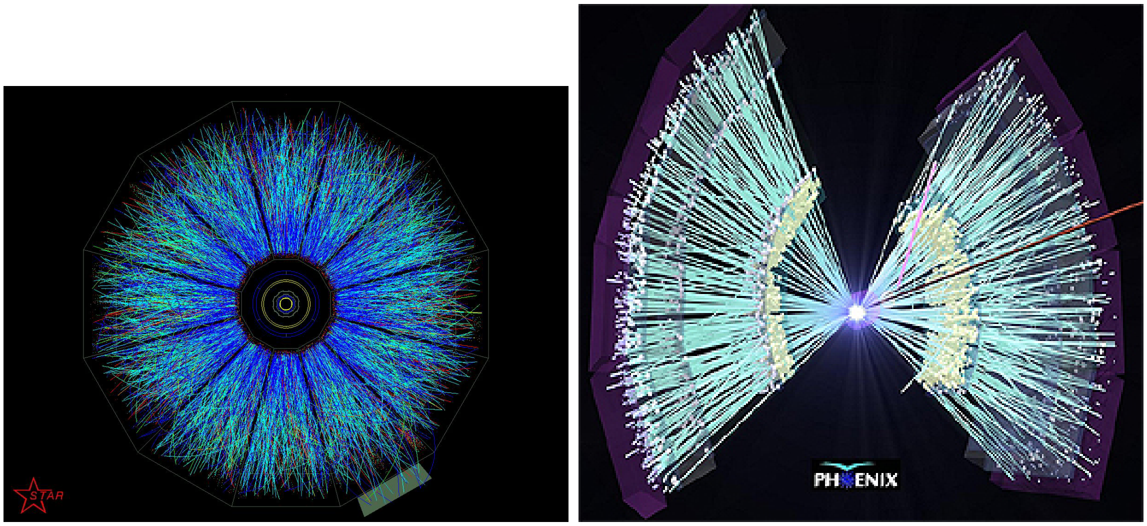

Figure 1.1: STAR and PHENIX events.

pair. During all these years RHIC was running not only AuAu systems, but also dAu, pp, CuCu and recently CuAu as well as UU collisions.

Initially, there were four experiments at RHIC: PHOBOS, BRAHMS, PHENIX and STAR. The experiments PHOBOS, BRAHMS have finished their programs and were closed. The STAR experiment [21] is measuring the hadron production over a large solid angle whereas the PHENIX experiment [22] focuses mainly on the measure of muons, electrons, photons and hadrons.

The project eRHIC, designed to collide electrons with heavy-ions [26, 27, 28, 29, 30, 31, 32], offers new perspectives for the RHIC collider.

1.1.2 LHC

The present and the future of the heavy-ion physics is connected with the new collider LHC, built at CERN, Geneva. The first PbPb collisions started at the end of 2010. The designed energy of 5.5 TeV per pair of nucleons was not reached and runs were made at the energy 2.76 TeV per pair. At the end of 2012 runs of pPb collisions at 5 TeV were also made before the planned stop of the collider for the renovations until 2015.

There are three experiments at the LHC participating in the heavy-ion program: ALICE, designed especially for heavy-ion collisions [33], CMS [34] and ATLAS [35]. Although CMS and ATLAS designed in a first place for the discovery of the Higgs boson, they have also an important role in the heavy-ion program. The LHC has already provided remarkable results. Indeed, in august 2012 the highest temperature ever achieved in a lab was reached: 5.5 trillion degrees [36]. This value, corresponding to $T = 304 \pm 51$ MeV was obtained from the exponential fit of the measured direct photons in PbPb collisions by ALICE collaboration.

The high energy obtained at the LHC allows to probe the quark-gluon plasma properties with a better accuracy. Theoretical understanding of these measurements is challenging and is one of the most important questions in heavy ion physics today.

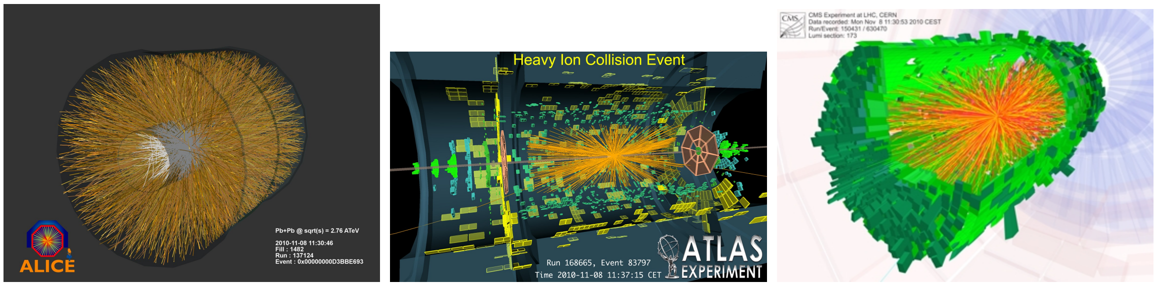

Figure 1.2: ALICE, ATLAS and CMS heavy-ion events.

1.1.3 Experimental observables

Geometry and kinematics of heavy-ion collisions

During the development of the heavy-ion physics, a basic dictionary was created and is commonly used among the physicists of the field. In this section, we will present the common terminology used [37, 38].

The standard picture of a nucleus-nucleus (AA) collision is the following: the two nuclei are accelerated close to the speed of light and due to the Lorentz contraction of distances in the boost direction, the two nuclei collide as two flat "pancakes" in their center of mass frame. The distance in the transverse plane between the centers of two colliding ions of radius R is called *impact parameter* and usually is denoted b. A collision where b is close to zero is called a *central* collision. For $0<b<2R$, collisions are *non-central* and for b close to 2R collisions are called *peripheral*. The nucleons that participate in the collision are called *participants*, other nucleons which are passing by without collision are called *spectators*. The participants which had at least one inelastic interaction are called *wounded nucleons*.

We denote "z" the axis parallel to the beam direction and "x" the axis parallel to the impact parameter vector. The plane defined by the $z-$ and $x-$axis is called the *reaction plane* of the collision.

A single collision is called an *event*. The number of particles produced in one event is called *multiplicity*.

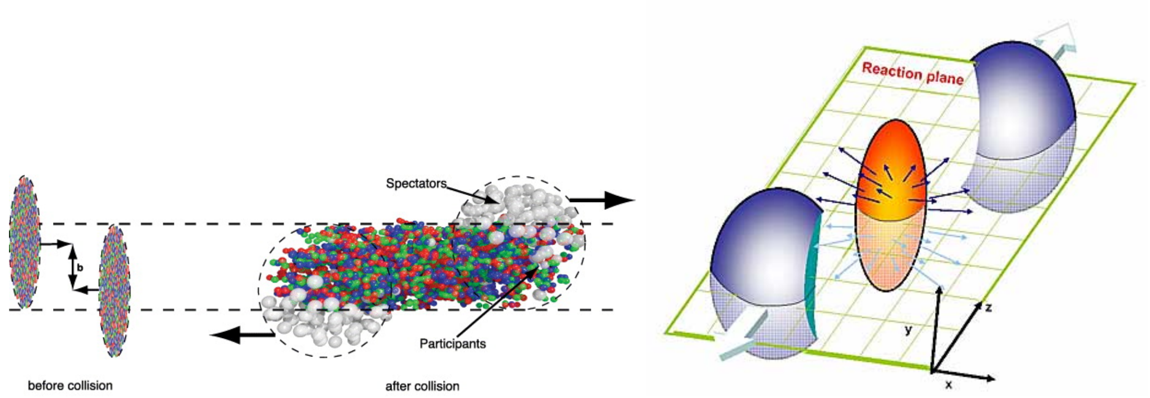

Figure 1.3: Schematic view on a heavy-ion collision.

In order to make a description of the kinematics of heavy-ion collisions the definition of *rapidity* is used. Rapidity is defined through the longitudinal component of momentum p_z and the energy $E = \sqrt{m^2 + |\mathbf{p}|^2}$ of particle

$$y = \frac{1}{2} \ln \frac{(E + p_z)}{(E - p_z)} = \text{Atanh} \left(\frac{p_z}{E} \right) . \tag{1.1}$$

In order to calculate the rapidity, one needs to know the value of the total energy which is not always available in the experiments. In the experiment usually one measures the momentum $\mathbf{p}$ of the particles but not their masses, i.e. their energy. The momentum components of one of these so-called *non-identified* particles reads

$$p_x = p_t \cos \phi, \tag{1.2}$$

$$p_y = p_t \sin \phi, \tag{1.3}$$

$$p_z = p_t \sinh \eta, \tag{1.4}$$

where p_t is the *transverse momentum*, ϕ is the *azimuthal angle* in the transverse plane and η is the *pseudorapidity* which can actually be measured.

For this reason, in experiment, it is more convenient to use an observable called the pseudorapidity, which is defined in a similar way

$$\eta = \frac{1}{2} \ln \frac{(|\mathbf{p}| + p_z)}{(|\mathbf{p}| - p_z)} = \ln \left(\cot \frac{\theta}{2} \right) = \ln \left(\tan \frac{\theta}{2} \right) = \text{Atanh} \left(\frac{p_z}{|\mathbf{p}|} \right) , \tag{1.5}$$

where θ is the polar angle, or the scattering angle, $p_z = |\mathbf{p}| \cos \theta$.

Experimental measurements are usually expressed in terms of pseudorapidity distribution. In hydrodynamic calculations, we deal with identified particles, in particular pions, kaons, protons and their anti-particles, thus we simulate the rapidity distribution and not the pseudorapidity distribution. In order to compare to experimental data, we need to derive pseudorapidity distribution from rapidity distribution [39]. From the two definitions above (1.1), (1.5), it can be obtained

$$dy = \frac{|\mathbf{p}|}{E} \cdot d\eta \, . \tag{1.6}$$

Using eq. (1.6), one obtains

$$\begin{aligned} \frac{dN}{p_t\, dp_t\, d\eta}(p_t) &= \frac{dN}{p_t\, dp_t\, dy}(p_t) \cdot \frac{|\mathbf{p}|}{E} \\ &= \frac{dN}{p_t\, dp_t\, dy}(p_t) \cdot \frac{|\mathbf{p}|}{\sqrt{m^2 + |\mathbf{p}|^2}} \\ &= \frac{dN}{p_t\, dp_t\, dy}(p_t) \cdot \frac{p_t \cosh\eta}{\sqrt{m^2 + p_t^2 \cosh^2\eta}} \, . \end{aligned} \tag{1.7}$$

Note that the factor

$$\frac{p_t \cosh\eta}{\sqrt{m^2 + p_t^2 \cosh^2\eta}} \, ,$$

is less than 1, leading to a distribution in pseudorapidity smaller than the distribution in rapidity.

In the region where $y \approx \eta \approx 0$ (called *midrapidity* region) the relation between the pseudorapidity distribution and the rapidity distribution reads

$$\frac{dN}{p_t\, dp_t\, d\eta}(p_t) = \frac{dN}{p_t\, dp_t\, dy}(p_t) \cdot \frac{p_t}{\sqrt{m^2 + p_t^2}} . \tag{1.8}$$

The rapidity distribution has an experimental Gaussian structure, the transformation of eq. (1.8) leads to a flat pseudorapidity distribution [40, 41] as it is shown in fig. 1.4.

Multiplicity and centrality

In theoretical calculations, it is needed to make a connection between such concepts as centrality and impact parameter.

The total inelastic cross-section is defined as

$$\sigma_{in} = \int_0^\infty 2\pi b' db' P(b'), \tag{1.9}$$

where $P(b')$ is the probability of inelastic collision and b' is the impact param-

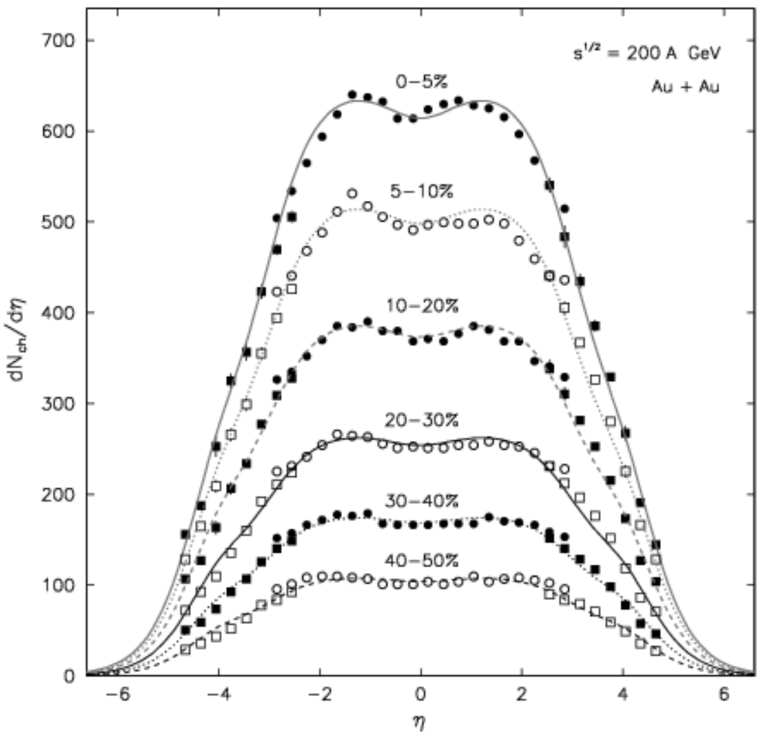

Figure 1.4: Pseudorapidity distribution for AuAu collisions at RHIC [1].

eter.

The centrality $c(\%)$ is generally defined as

$$c(\%) = \frac{\sigma_{in}^{b_{max}}}{\sigma_{in}}, \tag{1.10}$$

where b_{max} is a cut-off on the b' integral defining

$$\sigma_{in}^{b_{max}} = \int_0^{b_{max}} 2\pi b' db' P(b') \,. \tag{1.11}$$

If b_{max} is not too large, then the probability to have an inelastic collision is close to 1 due to the fact that the number of participants is large when $b' \to 0$, i.e. $P(b') = 1$. Then the formula eq. (1.10) can be simplified as

$$c(\%) \sim \frac{\pi b_{max}^2}{\sigma_{in}} \,. \tag{1.12}$$

The range of centrality is usually indicated as $0 - c\%$ and the maximum value of the impact parameter b_{max} in this range. For example thel central collisions are the collisions with a centrality range of $0 - 10\%$ and peripheral with a range of $90 - 100\%$. Note that the approximated definition (1.12) stops to work after

$\sim 80\%$ for the peripheral regions.

The definition (1.12) is suitable for theoretical calculations but not for experiments as the impact parameter is not directly measured but estimated via Monte Carlo models. One of the most common methods used in experiments is the definition of centrality as the % of events with the largest multiplicity recorded by detectors or with the largest number of participants [42].

1.2 Theoretical overview

In the last decades, there were a lot of attempts to describe the matter created in heavy-ion collisions. Different theoretical methods suitable for the description of large macroscopic systems were used, such as thermodynamics, hydrodynamics, transport theory, field theory at finite temperature and density, non-equilibrium field theory, Monte-Carlo simulations, etc. None of these approaches has provided as good description of the dynamic properties of quark-gluon plasma as relativistic viscous hydrodynamics [43, 44].

After a short introduction into basics of the fundamental theory of strong interactions, I will focus on the hydrodynamic description of the heavy-ion collisions which is the approach used in this thesis.

Basics of QCD

The system created in heavy-ion collisions seems to behave as a strongly coupled liquid. The fundamental theory of strong interactions is called QCD (Quantum Chromodynamics). QCD describes the interactions between quarks and gluons, which constitute the hadronic matter. The strong force is carried by gluons which are the vector bosons of the SU(3) color gauge group of QCD. Quarks and antiquarks carry respectively color and anti-color charges. Quarks, antiquarks and gluons are generically called partons.

Two main properties in QCD are the confinement of the colored particles in color singlet states and the so-called asymptotic freedom of QCD. Although it is not yet proven analytically, confinement is considered to be true because it explains the nonexistence of free quarks and can be shown in lattice QCD.

Asymptotic freedom is the fact that the strong coupling between partons decreases with the energy of the interaction.

If one adjusts the energy to the system, at some point the distance between the quarks is so increased, that it become energetically favorable to create another quark-antiquark pair, which will join these two separated quark-antiquarks and thus creates 2 hadrons. This can be illustrated with the so-called string model shown in the Fig. 1.5.

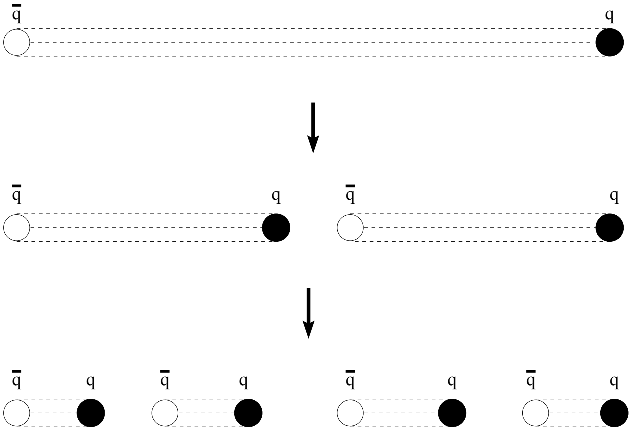

Figure 1.5: Schematic picture of the confinement. The pair $q\bar{q}$ stretches the string and breaks into two pairs of $q\bar{q}$ [2].

The name *quark-gluon plasma* (QGP) was introduced by Shuryak [45, 46] in 1978. One of the main interest of the heavy-ion collisions is the observation of the phase transition between the hadronic phase and the quark-gluon plasma. This phase transition can take place if one increases the temperature or the baryon density (or both of them at once) [47, 48, 49]. The phase transition that happened in the Early Universe appears to be a cross-over as it is shown in fig. 1.6.

The lattice calculations has shown the extremely high temperature $T \approx 175MeV$ (though recent calculations show $T \approx 155MeV$) needed to pass this transition from the hadronic phase to the quark-gluon plasma [50, 51, 52]. Such a high temperature is complicated to reach in the lab, the matter cannot be heated until this level by any chemical or nuclear reaction. The only way is to accelerate the matter, as we can see from the energy definition

$$E = \frac{mc^2}{\sqrt{1 - v^2/c^2}}. \tag{1.13}$$

In 2012 during Quark Matter 2012 it was announced by ALICE collaboration that 5.5 trillion $(5.5 \cdot 10^{12})$ degrees Celsius was reached at the LHC, what is 100000 times higher than the temperature in the center of the Sun [36]. This fact has been marked as the Guinness record.

In order to describe quark-gluon plasma one needs to define the equation of state (EoS). Equation of state is relating thermodynamic parameters, i.e. ε and P. If it isconsidered that the medium expands as a pure conformal

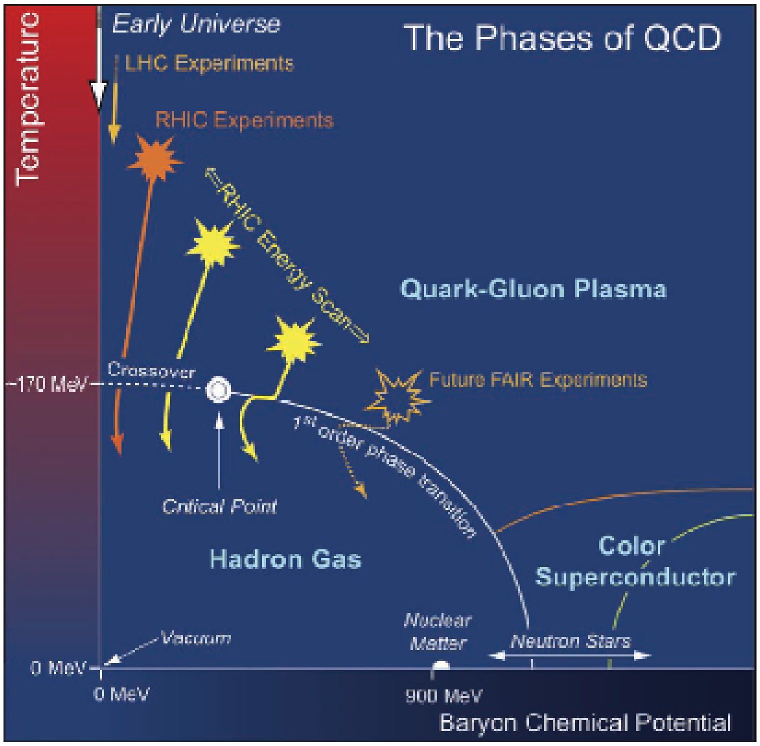

Figure 1.6: QCD phase diagram [3].

gas without a phase-transition, the conformal equation of state reads as $\varepsilon = 3P$. In order to have more realistic description it is needed to characterize the color confinement phase transition and the hadron gas at the later time of the evolution, i.e. at lower temperatures. In this case one consider the equation of state from lattice QCD. There are a number of different groups working with the EoS from lattice QCD. Some of the results of these groups are shown in figs. 1.7. In our calculations we use the equation of state from lattice QCD by Laine and Schroeder [53] shown in fig. 1.7 left, denoted as "Laine". This equation is obtained from the concept of a hadron resonance gas at low temperatures, a high-order weak-coupling perturbative QCD calculation at high temperatures and an analytic crossover regime interpolating between the high and low temperature regime. One of the most modern lattice QCD equations of state [5] using the physical quark masses is shown in fig. 1.7 right, but such equations are not considered in this thesis.

One of the most remarkable evidences of the existence of the quark-gluon plasma is the appearance of the so-called *anisotropic flow*. In this phenomenon the initial anisotropy of the coordinate space resulting from the geometry of non-central collisions is transformed into anisotropy in the momentum space. This effect is caused by the interactions in the created matter, that would not be the case for the hadron gas [21, 23, 54, 22].

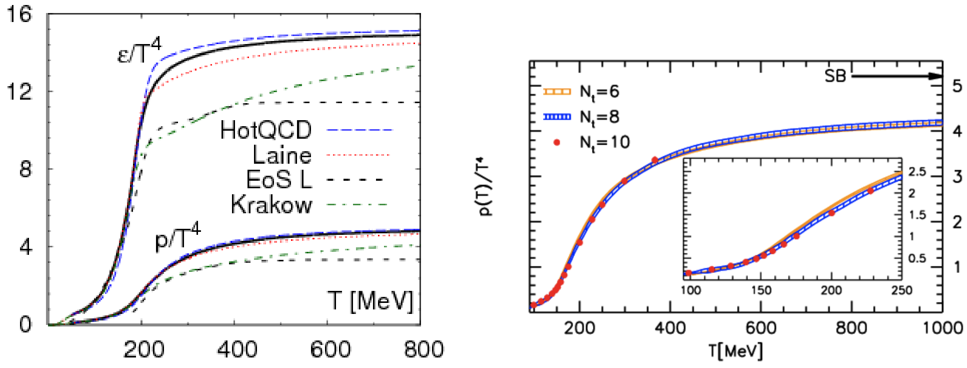

Figure 1.7: Left: Normalized energy density and pressure vs temperature from the lattice QCD, full line represents results from ref. [4]. Right: the normalized pressure vs temperature from the Wuppertal-Budapest group [5].

The main observable we study in this thesis is the anisotropic flow which we present in the next section.

1.3 Anisotropic flow

Collective flow characterizes the collective expansion as the response to the fluctuating initial geometry [55, 56]. After the collision the system starts to expand and later breaks down into the outgoing hadronic particles. Within a pure hydrodynamic approach these particles are emitted independently. Due to the fluctuations in the initial state there is no azimuthal symmetry, so the azimuthal distribution of these particles can be written as a Fourier series with respect to the azimuthal angle ϕ of the momentum of the outgoing particle

$$\frac{2\pi}{N}\frac{dN}{d\phi} = 1 + \sum_{n=1}^{\infty} 2v_n(p_t,\eta)\cos n\left(\phi - \Psi_n(p_t,\eta)\right), \tag{1.14}$$

where Ψ_n is the reference angle (usually referred to as *event-plane*) for each harmonic n that is defined [57, 58] as the phase of the complex Fourier coefficient[1] $\left\langle e^{in\phi}\right\rangle = v_n e^{in\Psi_n}$, or equivalently $\langle \sin n(\phi - \Psi_n)\rangle = 0$. Defined this way, both Ψ_n and v_n can be dependent on transverse momentum and pseudorapidity. The coefficients v_k are called *flow coefficients* and characterize the momentum anisotropy. v_1 is called directed flow, v_2 - elliptic flow, v_3 - triangular flow etc. Note that event-by-event anisotropic flow is well defined only in hydrodynamics. The event-by-event v_n, as defined above from the single-particle distribution,

---

[1] The brackets indicate an average over the probability density in a single event.

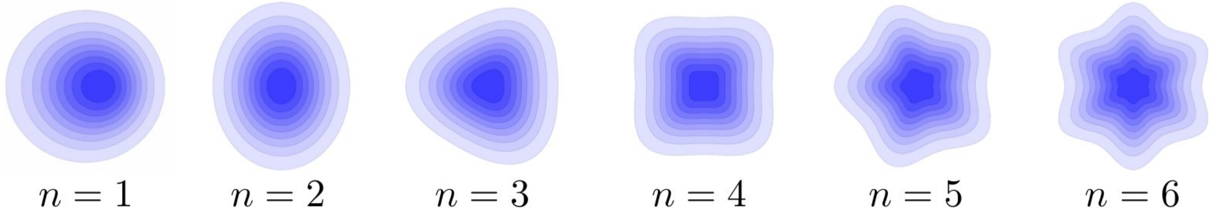

Figure 1.8: Flow coefficients v_n.

cannot be measured experimentally. Indeed, one measures the system after thermalization when a single event has already turned out into a thermal ensemble. The number of particles per event in the experiment is too small to measure both differential and integrated flow v_n. Anisotropic flow can only be measured through event-averaged azimuthal correlations between particles as this will be discussed later in this chapter.

The interest to the studies of the particle momentum anisotropy in the directions transverse to the beam has grown after the first observation of elliptic flow [38] which was first suggested by Ollitrault [55]. The anisotropy of the flow is the only observable that allows to unravel the early state of the collective system. This is due to the fact that it can only be generated at first few fm/c of the system evolution, before the spatial asymmetries of the system decrease. The anisotropic flow must be sensitive to the particle interactions in the early system evolution. It is a unique hadronic observable which can provide information on the properties of the quark-gluon plasma present in the early stage of collisions.

1.3.1 Directed flow

In the absence of fluctuations, the directed flow v_1 is believed to arise from the aside deflection of the colliding ions [38] and develops along the direction of the impact parameter [59]. Due to the collision symmetry, directed flow is an odd function of pseudorapidity

$$v_1^{odd}(\eta) = -v_1^{odd}(-\eta)\,. \tag{1.15}$$

The illustration of the v_1^{odd} is shown in the fig. 1.9. We see the deflection of the participants of the incoming nucleus, positive in rapidity with $x > 0$ and negative in rapidity for the zone $x < 0$.

Fluctuations in the initial state have an influence on the reference angles Ψ_n

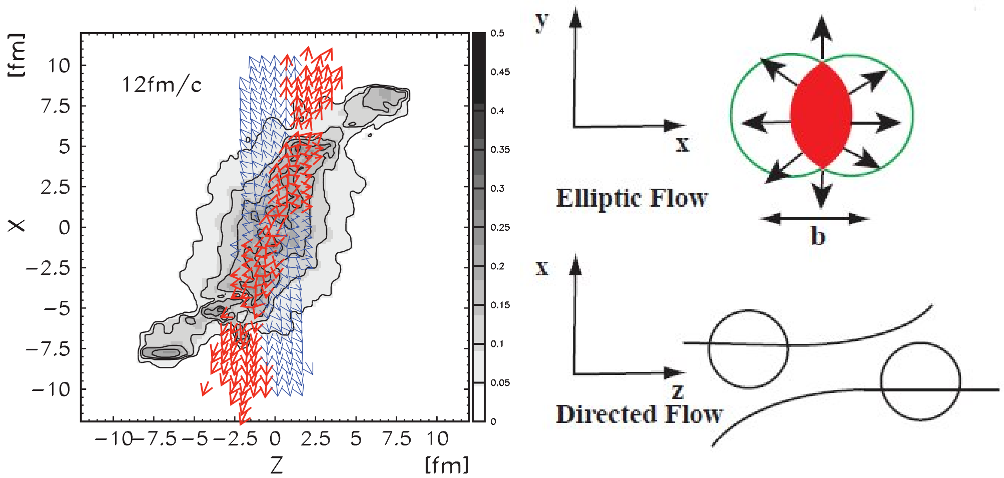

Figure 1.9: Net baryon density in the reaction plane illustrating v_1^{odd} with velocity arrows for midrapidity fluid elements, bold red arrows corresponds to the flow [6] (left). Schematic picture of elliptic and directed flow v_1^{odd} (right).

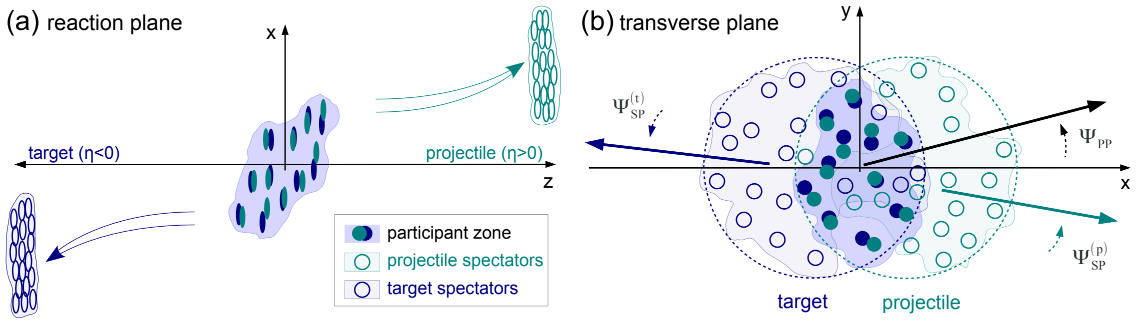

Figure 1.10: Schematic picture of the v_1^{even} component in the reaction (a) and the transverse (b) plane. Ψ_{PP} is the participant plane angle defined by the dipole asymmetry of the initial energy density. Ψ_{SP}^p and Ψ_{SP}^t are projectile ($\eta > 0$) and target ($\eta < 0$) spectators plane angles respectively.

for all n, see fig. 1.10. As a consequence, one can expect an additional contribution to the directed flow from the fluctuations [60]. With the fluctuations taken into account, the directed flow has additional component which is even function of pseudorapidity [61]

$$v_1^{even}(\eta) = v_1^{even}(-\eta)\,. \tag{1.16}$$

This additional even component is not vanishing at midrapidity, while the odd component is zero due to the symmetry. The even component of the directed flow is the subject of studies in the Chapters 2 and 3.

The directed flow can be written as a sum of the odd and even components [61]

$$v_1(\eta)e^{i\psi_1(\eta)} = v_1^{even}(\eta)e^{i\Psi_1^{even}(\eta)} + v_1^{odd}(\eta)e^{i\Psi_1^{odd}(\eta)}\,. \tag{1.17}$$

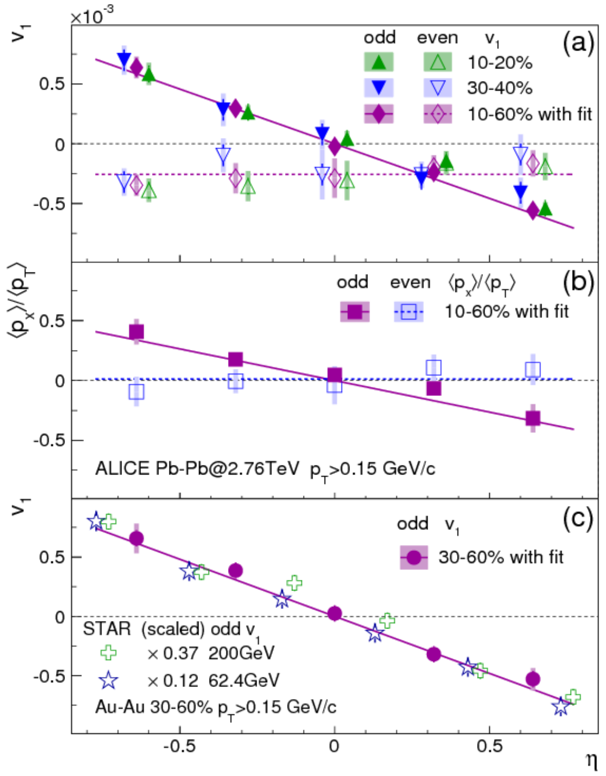

Figure 1.11: v_1^{odd} and v_1^{even} with dependence on pseudorapidity for Pb-Pb collisions at $\sqrt{s_{NN}} = 2.76$ TeV (a), the $\langle p_x \rangle / \langle p_t \rangle$ dependence on pseudorapidity for Pb-Pb collisions at $\sqrt{s_{NN}} = 2.76$ TeV (b), v_1^{odd} comparison of ALICE Pb-Pb measurements with the STAR data (scaled) [7] for Au-Au collisions at $\sqrt{s_{NN}} = 200(62.4)$ GeV (c), taken from [8].

Recent studies show that both $v_1(\eta)^{odd}$ and $v_1(\eta)^{even}$ have a weak centrality dependence.

The component $v_1(\eta)^{odd}$ has shown a negative slope [7, 8] in the experimental measurements whereas a positive slope was expected in the model calculations [62, 63], though some of them had also a negative slope [64]. The even component $v_1(\eta)^{even}$ measured at ALICE was found to be negative and independent of pseudorapidity within uncertainties. Both behaviours are illustrated in the figs. 1.11(a) and 1.11(c).

At the beginning of 2012, v_1^{odd} was already measured [65, 66, 67, 68, 7, 69, 70, 71] and studied [64] for RHIC energies. At that time, v_1^{even} was not measured yet neither at RHIC nor at LHC.

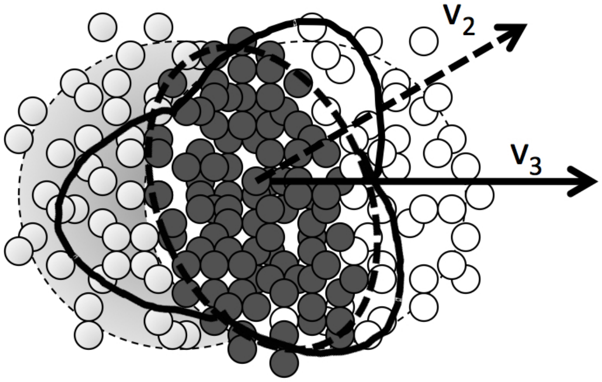

Figure 1.12: Elliptic and triangular flows from fluctuated initial state [9].

1.3.2 Elliptic and triangular flows

The second Fourier coefficient v_2, elliptic flow, is the most studied flow coefficient. The origin of the elliptic flow in non-central collisions is the spatial anisotropy of initial distribution [55] which has an elliptic form. If the collision is central, the overlap area has a round form, in this case the origin of elliptic flow is connected with fluctuations which are coming from the wave-functions of nucleons in each event.

Recent studies have shown some remarkable features of the elliptic flow. It was shown that v_2 increases with centrality percentage for small centralities as we can see from the fig. 1.13. This can be explained by the fact that elliptic flow is proportional to the initial eccentricity. Indeed, when eccentricity is smaller, i.e. for bigger centrality percentage, the flow is growing. For more peripheral collisions the system becomes so small that the viscous effects become more important. Indeed, the viscous effects are inversely proportional to the size of the system. These viscous effect decrease the flow. In the same time, the eccentricity is larger for peripheral collisions, leading to a bigger flow. These two processes are in competition. For peripheral collisions, the viscous effect dominates.

Elliptic flow is growing with energy of collisions, thus we have bigger values of v_2 with LHC energies than with lower energies [72] as we can see in fig. 1.14. Indeed, with higher energies of collisions, the initial temperature of the system is higher so that the system will take more time to cool down to the freeze out temperature meaning that its life-time is increased.

As shown in fig. 1.15 the v_2 is growing linearly for low p_t range which is what one expects from hydrodynamics. However, at high p_t the flow is not anymore linear which can be explained by the presence of hard probes, particularly the

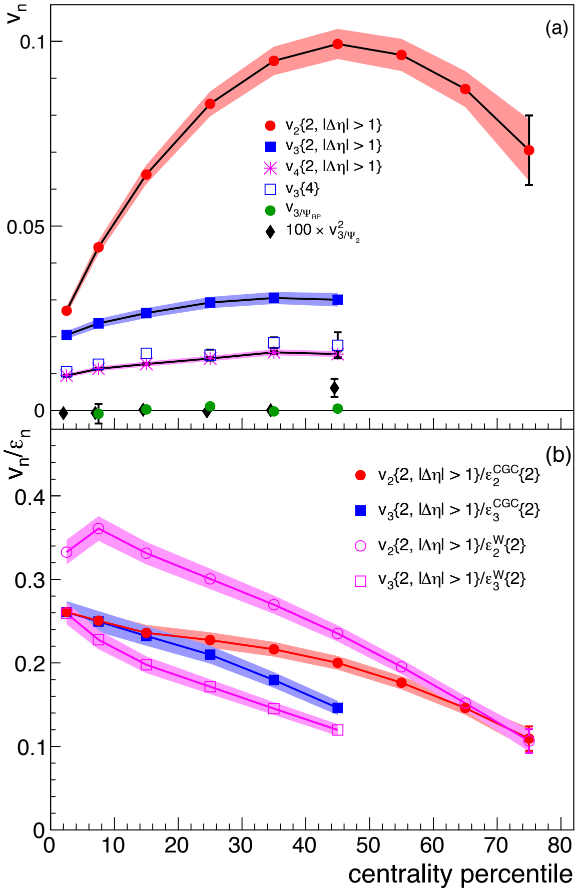

Figure 1.13: v_2 and v_3 dependence on centrality, ALICE collaboration [10].

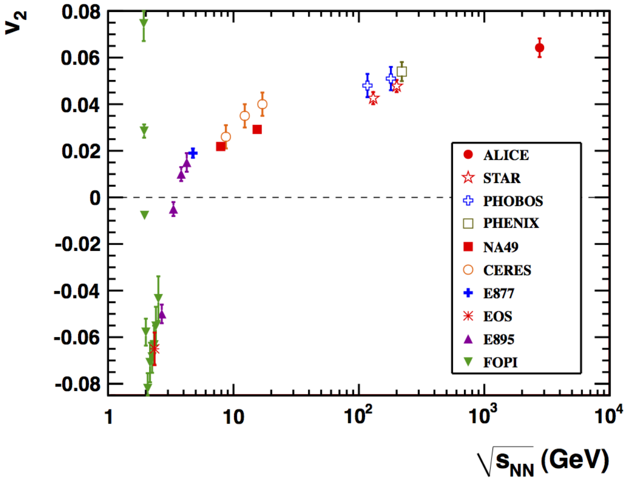

Figure 1.14: Integrated v_2 by ALICE collaboration compared with lower energy results [72], 20–30% centrality range.

presence of jets.

The triangular flow, v_3, was first discovered during the studies of the two-particle correlations as an explanation of the structures "ridge" and "shoulders"

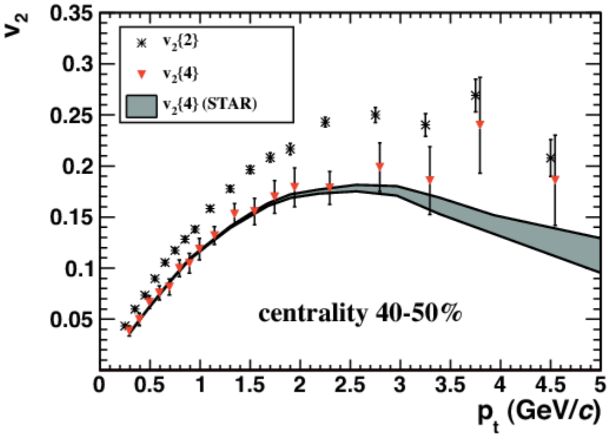

Figure 1.15: $v_2(p_t)$ by ALICE collaboration compared [72], 40–50% centrality range.

appeared in the correlations [73], see later in this Chapter. The triangular flow v_3 is understood as the response of a triangular deformation which is caused by fluctuations of initial geometry [73]. The physics of v_3 was found to have a lot of similar features with the physics of elliptic flow v_2. Here I only mention the main properties of the triangular flow. The magnitude of the integrated values of v_2 and v_3 is similar for central collisions [74], and is the largest among all the Fourier coefficients. The triangular flow v_3 is also linear with p_t, though it grows quicker with p_t than v_2 as it can be seen in fig. 1.16.

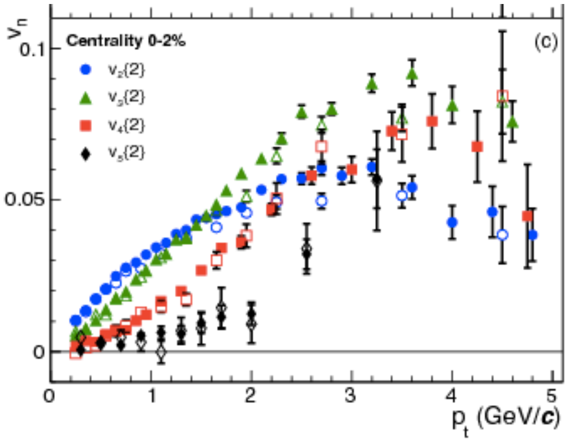

Figure 1.16: $v_n(p_t)$, $n = 2, 3, 4, 5$ by ALICE collaboration for central collisions [10].

The v_3 is growing more slowly than v_2 with centrality percentage as we can see on fig. 1.13. In the central collisions, the system is larger and thus it has less fluctuations, i.e. the triangularity is smaller. For smaller systems at peripheral collisions fluctuations become more important and as a consequence v_3 increases with centrality percentage. The v_3 is also dependent on the energy of the collisions and it is higher for LHC energies.

The elliptic and triangular flow are the subjects of studies described in the Chapter 4.

1.3.3 Flow measurements

Two-particle correlations

The study of the two-particle correlations in $\Delta\phi$ and $\Delta\eta$ has been a very debated topic of the heavy-ion physics of the last years [75]. Indeed, it was found out that the measured two-particle correlation behavior for proton-proton collisions and heavy-ion collisions is different. As it is shown in fig. 1.17 the distribution in *pp* collisions is almost flat in the azimuth with the specific ridge around $\Delta\eta = 0$ for all $\Delta\phi$ range. For AA collisions, the distribution presents additional structures at large $\Delta\eta$. The structure around $\Delta\phi \sim 0$ wide in $\Delta\eta$ is called the *ridge*, while the structure at $\Delta\phi \sim \pi$ is called the *shoulders* [76, 77, 78, 79]. The explanation of these phenomena can be found in the flow-harmonics studies [80, 81, 82, 83, 84, 85, 73, 74]. Recently the ridge structures were also found in pp-collisions at LHC [86].

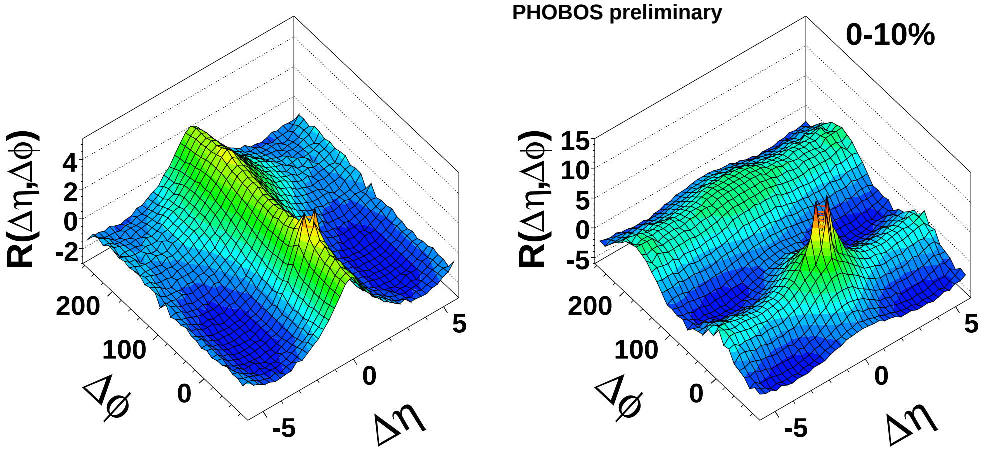

Figure 1.17: Two-particle correlations for pp (200 GeV) and AuAu (200 GeV) collisions at RHIC [11].

The flow harmonics v_n can be measured from two or many particle correlations. The simplest method in order to extract the flow coefficients v_n is the *two-particle correlations* method. The measured anisotropy from the two-particle azimuthal distribution reads

$$\frac{dN^{pairs}}{d\Delta\phi} \propto \left(1 + \sum_{n=1}^{\infty} 2V_{n\Delta}(p_t^a, p_t^b) \cos(n\Delta\phi)\right) , \tag{1.18}$$

where a pair of particles is correlated. The relative azimuthal angle is $\Delta\phi = \phi_a - \phi_b$ and the pseudorapidity is $\Delta\eta = \eta_a - \eta_b$ [78]. Thus, the two-particle correlations denoted as $V_{n\Delta}$ can be represented as

$$V_{n\Delta} \equiv \langle \cos[n\,\Delta\phi] \rangle \ . \tag{1.19}$$

This value $V_{n\Delta}$ can be measured as a function of p_t for both particles a and b.

If the anisotropy is driven by the collective motion, the $V_{n\Delta}$ should factorize into the product of two single-particle correlation [87].

$$V_{n\Delta} = v_n(p_t^a) v_n(p_t^b) \, . \tag{1.20}$$

In the two-particle correlation method, the left hand side of eq.(1.20) represents an $N \times N$ symmetric matrix which can be generally fitted by the right hand side of the equation with the N parameters v_n where N is the number of p_t bins [14].

The azimuthal correlations $V_{n\Delta}$ which factorizes as (1.20) is called "flow" correlation. The two-particle correlation usually has a contribution called "non-flow" which breaks this factorization. Thus, the two-particle correlation with the non-flow contribution reads

$$V_{n\Delta} = v_n(p_t^a) v_n(p_t^b) + \delta_n \, . \tag{1.21}$$

The non-flow contribution leads to fluctuation of the magnitude and the direction of the anisotropic flow at fixed centrality, from one event to another. The equation (1.21) can also be used in the two-particle correlation method with an additional parameter taken into account. This method will be used in our calculations in the Chapter 2.

Other methods

The flow can be also measured by other methods. One of them is the multi-particle correlations method described in ref. [88]. The advantage of higher order cumulants is that one can separate the so-called "flow" from the "non-flow" correlations that will be discussed in the next section. In this thesis we will mainly focus on the two-particle correlation method and therefore we will not detail other methods such as: Lee-Yang Zeros, q-distributions, Bessel, Fourier, for which one can find more details in ref. [38] and therein.

1.4 Initial conditions

In order to make a study of the initial state, one has to model all the evolution of the quark-gluon plasma from the initial stage to the freeze-out. By comparing the model results with the experimental data, one could draw conclusions about the initial state.

The first step of any hydrodynamic modeling is to specify initial conditions. Since we work with ultra-relativistic hydrodynamics, we need the energy-density profile as an input for the hydrodynamic equations.

For a long time smooth and symmetric profile was used in hydro simulation, showing quite reasonable results. Only recently it was realized that due to the fluctuations existing in initial state the geometry of initial profile is not smooth and symmetric, and changes from one event to another, this statement gave life to numerous models of initial state, taking into account initial fluctuations [89, 90, 73] .

Here we are going to speak about two main types of models of initial conditions: The Glauber type of models and the QCD-inspired type of models. Typically these models are using the Monte Carlo approach. As it was shown [43], both types of models give a reasonable description of the spectra but they give different predictions for initial spatial eccentricity which leads to different values of the differential flow. We discuss here the main features of each type of models.

1.4.1 Glauber model

The Glauber model [91, 92, 93] is one of the oldest models of initial state. In this thesis, we use two implementations of the Glauber model: the optical Glauber model used in our calculations, and the Monte Carlo variation of the Glauber model [93] called PHOBOS Monte Carlo model [94], tested in the Chapter 4.

In the optical Glauber model, densities of participants and binary collisions are calculated directly from the probability distribution as one can see from eqs.(1.25), (1.26).

In the Glauber model the nuclei can be described by Woods-Saxon density distribution

$$\rho_A(x) = \frac{\rho_0}{1 + exp[(|x| - r_0)/a]} \tag{1.22}$$

where we take A=208, $r_0 = 6.56$ fm and $a = 0.45$ fm for the lead nucleus. The value of ρ_0 is chosen in such a way that

$$A = \int d^3x \, \rho_A(x) \, . \tag{1.23}$$

We define the nuclear thickness function as

$$T_A(x) = \int_{-\infty}^{\infty} dz \, \rho_A(x) \, . \tag{1.24}$$

The density of nucleons participating in the collision n_{part} reads

$$\begin{aligned} n_{part}(x,y,b) = T_A\left(x+\frac{b}{2},y\right)&\left[1-\left(1-\frac{\sigma\, T_A\left(x-\frac{b}{2},y\right)}{A}\right)^A\right] \\ +T_A\left(x-\frac{b}{2},y\right)&\left[1-\left(1-\frac{\sigma\, T_A\left(x+\frac{b}{2},y\right)}{A}\right)^A\right] \, . \end{aligned} \tag{1.25}$$

The density of binary collisions n_{coll} reads

$$n_{coll}(x,y,b) = \sigma\, T_A\left(x+\frac{b}{2},y\right) T_A\left(x-\frac{b}{2},y\right) \tag{1.26}$$

where b is the impact parameter and σ is the nucleon-nucleon cross section. For Pb-Pb collisions we take the value $\sigma = 67.7$ mb at $\sqrt{s} = 2.76$ TeV per nucleon pair.

The total number of participating nucleons

$$N_{part}(b) = \int n_{part}(x,y,b) dxdy \tag{1.27}$$

is used to characterize the centrality class of the collision.

The total number of binary collisions is

$$N_{coll}(b) = \int n_{coll}(x,y,b) dxdy \, . \tag{1.28}$$

As an initial condition for the energy density, the following parametrization is used

$$\epsilon(\tau = \tau_0, x, y, b) = Const\, n_{coll}(x,y,b) \tag{1.29}$$

which gives a good description of the multiplicity distribution of the experimental data. The constant is chosen in such a way that at zero impact parameter the energy density $\epsilon(\tau_0, 0, 0, 0)$ corresponds to a temperature T_i, defined from the equation of state. T_i is used as a free parameter which is tuned during the calculations in such a way that the final value of the multiplicity corresponds to the experimental value.

In some particular cases, we need to have more precise results in our calculations. In this case we use the parametrization for entropy density, combining both density of participant nucleons and the density of binary collisions

$$s(\tau = \tau_0, x, y, b) = A\, n_{part}(x, y, b) + B\, n_{coll}(x, y, b)\,. \tag{1.30}$$

The coefficients A and B are corresponding to the values used by the collaborations.

In the Monte Carlo version of the Glauber model, the positions of nucleons within nuclei are sampled according to the Monte Carlo method and their positions in the transverse plane are used to decide if there is interaction between the nucleons. In this way the total number of participants N_{part} and the total number of binary collisions N_{coll} can be calculated. Typically each nucleon is modeled as a Gaussian source so that the resulting energy density is the sum of Gaussians. The comparison of the initial energy density profiles from Monte Carlo and Optical Glauber models is represented in the fig. 1.18.

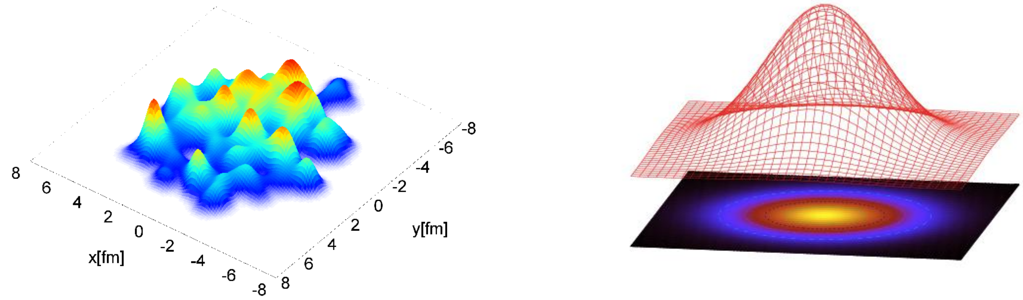

Figure 1.18: Monte Carlo Glauber (left) [12, 13] and Optical Glauber (right) initial energy density profile.

Recently the Glauber approach has been developed further by taking into account additional fluctuations [95] but we do not consider such models in this thesis.

1.4.2 Color-Glass-Condensate

The Color-Glass-Condensate (CGC) model belongs to the large class of the QCD-inspired models. This model is based on the idea of the gluon saturation at high energy. “Color” refers to a type of the charges carried by gluons. “Glass” refers to a material that is disordered and acts like a solid on short time scales but as a liquid on long time scales. Indeed, during heavy-ion collisions, the gluons themselves are disordered and do not change their positions rapidly because of the Lorentz time dilation. “Condensate” means that the density of gluons is very high. These gluons can be packed until their phase space density is so high that interactions prevent higher gluon occupation. With increasing density, the gluons are forced to occupy higher momenta where the coupling becomes weak. The density saturates at $dN/d^2p_td^2r_t \sim 1/\alpha_s \gg 1$ [96]. Within this QCD inspired model, the energy density is proportional to the density of gluons.

The oldest CGC model of initial state is KLN (Kharzeev-Levin-Nardi) model which is using k_T-factorization [97, 98].

Different implementations of this and other QCD-inspired models will be discussed in the Chapter 4.

1.5 Hydro approach

The hydrodynamic approach proposed historically in the 50’s by Landau and continued by Bjorken, gives a reasonable description of the matter created in the heavy-ion experiments. Today’s hydrodynamic calculations continue the general concepts proposed by Landau and Bjorken, including the recent knowledge about the initial conditions, transverse expansion and the modern equation of state from the lattice QCD.

1.5.1 Hydrodynamic models

Nowadays, the hydrodynamic approach is the most popular and has been intensively studied in the last decade.

There are several types of the hydrodynamic codes that exist in order to simulate the heavy-ion collisions. Usually it is 2+1D and 3+1D which can be ideal hydrodynamics codes, or the codes taking into account different transport phenomena, such as viscosity etc.

Currently, a major role in this area is played by the codes taking into account the viscosity and fluctuations. For our purposes we use a 2+1D viscous hydrodynamic code created by U. and P. Romatschke and modified by M. Luzum [99]. The code has been used for several years and provides a good description of experimental data [43].

1.5.2 Event-by-event hydrodynamic versus single-shot hydrodynamic

Until recently, event-by-event fluctuations were taken into account only as an average of an ensemble of events [100, 101, 102, 103, 104, 89]. This type of hydrodynamics is called *single-shot* hydrodynamics. In these calculations the initial density profile is smooth and propagated hydrodynamically. In the single-shot hydrodynamic only average values of flow components can be computed. Another type of hydrodynamics got the name *event-by-event hydrodynamics*. In this case flow fluctuations can be computed from event to event [105, 106, 107, 108, 13, 109, 110, 111, 9, 112, 113, 114].

In the experiment, heavy-ion collisions take place event by event, in theory often hydrodynamic evolution is not computed for each event, but approximately by generating a single smooth initial density distribution, from where the mean values of flow coefficients are extracted, corresponding to mean participant eccentricities. This value is not measured in experiment. What can be measured is the average of an ensemble of events. Though the single-shot hydrodynamic calculations give a good qualitative picture and agreement with data, there is a difference of a few % for peripheral collisions in results for flow components and eccentricities [18].

1.5.3 Hydro evolution

According to Landau [115], the dynamic state of a liquid is determined by the fluid velocity $\mathbf{v} = \mathbf{v}(x, y, z, t)$ and by any two thermodynamic properties such as pressure p(x,y,z,t) and fluid density $\rho(x, y, z, t)$. Indeed, the equation of state relates the thermodynamic quantities so that the definition of $\mathbf{v}$, p and ρ is enough to uniquely define the dynamic state of liquid. These quantities are connected by the continuity equation

$$\frac{\partial \rho}{\partial t} + div\, \mathbf{j} = \mathbf{0}, \tag{1.31}$$

where $\mathbf{j} = \rho \mathbf{v}$ is the current density.

The equation of motion, or Euler equation is defined as

$$\frac{\partial \mathbf{v}}{\partial t} + (\mathbf{v}\partial)\,\mathbf{v} = -\frac{1}{\rho}\,\mathbf{grad}(p)\,. \tag{1.32}$$

By adjusting the equation of state $p = p(\rho)$, we get a complete system of equations for the ideal liquid.

In the relativistic case the system is not anymore described by the mass density $\rho(x, y, z, t)$ because it ignores kinetic energy which becomes important for high velocities. In the relativistic case, the description is made through the energy density $\epsilon(x, y, z, t)$ which transforms back to the mass density in non-relativistic limit. In the same way the velocity $\mathbf{v}(x, y, z, t)$ has to be replaced by 4-velocity u^μ which is defined as[2]

$$u^0 = \frac{1}{\sqrt{1-\mathbf{v}^2}}\,, \tag{1.33}$$

$$\mathbf{u} = \frac{\mathbf{v}}{\sqrt{1-\mathbf{v^2}}}\,, \tag{1.34}$$

which satisfies

$$u^2 = u^\mu u_\mu = \left(u^0\right)^2 - \mathbf{u^2} = \mathbf{1}. \tag{1.35}$$

In order to get the relativistic equations [116, 117], we work with the energy-momentum tensor $T^{\mu\nu}$ where $T^{00} = T_{00}$ is the energy density, $T^{0\alpha} = -T_{0\alpha}$ is the density of the momentum component, $T^{\alpha\beta} = T_{\alpha\beta}$ is the pressure tensor of the flux along the α axis of the momentum component and $T^{\alpha 0}$ is the energy flux along the α axis. In the local rest frame the tensor of energy-momentum is

$$T^{\mu\nu} = \begin{pmatrix} \epsilon & 0 & 0 & 0 \\ 0 & P & 0 & 0 \\ 0 & 0 & P & 0 \\ 0 & 0 & 0 & P \end{pmatrix}\,. \tag{1.36}$$

For an arbitrary fluid velocity the energy-momentum tensor can be written as

$$T^{\mu\nu} = (\epsilon + P)\,u^\mu u^\nu - P\,g^{\mu\nu}\,, \tag{1.37}$$

where $g^{\mu\nu} = \mathrm{diag}(1, -1, -1, -1)$ is the Minkowski metric tensor.

The conservation of energy and momentum reads

$$\partial_\mu T^{\mu\nu} = 0\,. \tag{1.38}$$

---

[2] The natural units $c = \hbar = 1$ are used.

In order to generalize the continuity equation to the relativistic case, we define a baryon density n in the rest frame such that in the moving frame the density reads $n\,u^0$. We replace then the density ρ by $n\,u^0$ and use the equation $\mathbf{u} = u^0\mathbf{v}$. Thus, we obtain the equation of conservation of the baryon number

$$\partial_\mu \left(nu^\mu\right) = 0\,, \tag{1.39}$$

where nu^μ is the 4-vector, nu^0 is the baryon density and $n\mathbf{u}$ is the baryon flux, and we denote $\mathbf{j} = n\mathbf{u}$. Eqs. (1.37), (1.38) and (1.39) adjusted by the equation of state of the fluid, provide the full system of equations of ideal relativistic hydrodynamics.

Viscous hydrodynamics

For a non-ideal fluid where dissipation takes place, the equation of motion is generalized by the Navier-Stokes equation [117, 43]

$$\rho\left(\frac{\partial v_i}{\partial t} + v_k\frac{\delta v_i}{\delta x_k}\right) = -\frac{\partial p}{\partial x_i} + \frac{\partial}{\partial x_k}\left(\eta\left(\frac{\partial v_i}{\partial x_k} + \frac{\partial v_k}{\partial x_i} - \frac{2}{3}\delta_{ik}\frac{\partial v_l}{\partial x_l}\right)\right) + \frac{\partial}{\partial x_i}\left(\zeta\frac{\partial v_l}{\partial x_l}\right)\,, \tag{1.40}$$

where the dissipation part is usually written in terms of the viscous stress tensor

$$\Pi_{ki} = -\eta\left(\frac{\partial v_i}{\partial x_k} + \frac{\partial v_k}{\partial x_i} - \frac{2}{3}\delta_{ik}\frac{\partial v_l}{\partial x_l}\right) - \zeta\delta_{ik}\frac{\partial v_l}{\partial x_l}\,, \tag{1.41}$$

where i=1,2,3, mean space directions, η is the shear viscosity and ζ is the bulk viscosity.

The energy-momentum tensor for a non-ideal fluid reads

$$T^{\mu\nu} = T_0^{\mu\nu} + \Pi^{\mu\nu} \tag{1.42}$$

where $T_0^{\mu\nu}$ is the energy-momentum tensor for an ideal liquid while $\Pi^{\mu\nu}$ is the viscous stress tensor that contains the dissipation effects.

Considering a system at zero chemical potential, the conservation of energy-momentum reads

$$u_\mu T^{\mu\nu} = \epsilon u^\nu\,, \qquad u_\mu \Pi^{\mu\nu} = 0\,. \tag{1.43}$$

For a relativistic viscous fluid dynamics then the continuity equation reads

$$D\epsilon + (\epsilon + p)\,\partial_\mu u^\mu - \Pi^{\mu\nu}\nabla_{(\mu u_\nu)} = 0\,, \tag{1.44}$$

where [43]

$$\nabla_{(\mu u_\nu)} = \frac{1}{2}\left(\nabla_\mu u_\nu + \nabla_\nu u_\mu\right) , \tag{1.45}$$

and the relativistic Navier-Stokes equation reads

$$(\epsilon + p)\, Du^\alpha - \nabla^\alpha p + \Delta^\alpha_\nu \partial_\mu \Pi^{\mu\nu} = 0 \, , \tag{1.46}$$

with $D \equiv u^\alpha D_\alpha$ and $\nabla^\mu \equiv \Delta^{\mu\alpha} D_\alpha$ where we denote the covariant derivative $D_\alpha = \frac{\partial}{\partial x^\alpha}$.

The viscous tensor can be represented as a sum of a traceless term $\pi^{\mu\nu}$ and the remainder Π

$$\Pi^{\mu\nu} = \pi^{\mu\nu} + \Delta^{\mu\nu}\Pi \, , \tag{1.47}$$

where

$$\pi^{\mu\nu} = \eta \nabla^{<\mu u^\nu>} \, , \qquad \Pi = \zeta \nabla_\alpha u^\alpha \, , \tag{1.48}$$

with η the shear viscosity and ζ the bulk viscosity, where [43]

$$\nabla_{<\mu u_\nu>} = 2\nabla_{(\mu u_\nu)} - \frac{2}{3}\delta_{\mu\nu}\nabla_\alpha u^\alpha \, . \tag{1.49}$$

Numerical solution

Navier-Stokes equations are difficult to solve numerically [43, 118]. In order to overcome the numerical instabilities, higher gradient terms are added to the shear and bulk viscosity terms as following

$$\begin{aligned}\pi^{\mu\nu} = {} & \eta\sigma^{\mu\nu} - \eta\tau_\pi \left({}^{<}D\sigma^{\mu\nu>} + \frac{4}{3}\left(\nabla \cdot u\right)\sigma^{\mu\nu} \right) \\ & - \frac{\lambda_1}{2}\sigma^{<\mu}_{\lambda}\sigma^{\nu>\lambda} + \frac{\lambda_2}{2}\sigma^{<\mu}_{\lambda} w^{\nu>\lambda} - \frac{\lambda_3}{2}\omega^{<\mu}_{\lambda}\omega^{\nu>\lambda} \\ & - \eta\tau^{*}_{\pi}\frac{4}{3}\left(\nabla \cdot u\right)\sigma^{\mu\nu} + \frac{\lambda_4}{2}\nabla^{<\mu}\ln s \nabla^{\nu>}\ln s\end{aligned} \tag{1.50}$$

$$\begin{aligned}\Pi = {} & \zeta\left(\nabla \cdot u\right) - \zeta\tau_\Pi D\left(\nabla \cdot u\right) - \xi_1\sigma^{\mu\nu}\sigma_{\mu\nu} - \xi_2\left(\nabla \cdot u\right)^2 \\ & - \xi_3\omega^{\mu\nu}\omega_{\mu\nu} + \xi_4\nabla_\mu \ln s \nabla^\mu \ln s \, .\end{aligned} \tag{1.51}$$

In eqs. (1.50) and (1.51), the entropy density is denoted $s = (\epsilon + p)/T$ in zero chemical potential. In these equations we consider a flat space. In addition to the first-order transport coefficients, η and ζ, there are 11 second-order transport coefficients introduced: τ_π,τ_π^*, λ_1, λ_2, λ_3, λ_4, τ_Π, ξ_1, ξ_2, ξ_3 and ξ_4. We denote $\sigma^{\mu\nu} = \nabla^{<\mu}u^{\nu>}$ and the fluid vorticity is defined $\omega^{\mu\nu} = -\nabla^{[\mu}u^{\nu]}$, where the brackets are defined as

$$A^{[\mu}B^{\nu]} = \frac{1}{2}\left(A^\mu B^\nu - A^\nu B^\mu\right) . \tag{1.52}$$

The transport coefficients should be in principle calculated from the underlying theory (QCD) which is generally not possible. These coefficients are thus considered as free parameters. In order to reduce the number of parameters, the positive divergence of the entropy can be required to provide two constraints [119] leaving only 9 free parameters.

The ratio ζ/s, bulk viscosity over entropy density is generally small in comparison to the shear viscosity over entropy density η/s [120, 121, 122]. Thus we put $\zeta = 0$, and consider conformal fluids. Under these assumptions, one gets [123]:

$$\begin{aligned}\Pi^{\mu\nu} = \pi^{\mu\nu} = \eta\sigma^{\mu\nu} - \eta\tau_\pi\left[{}^{\langle}D\sigma^{\mu\nu\rangle} + \frac{4}{3}(\nabla\cdot u)\sigma^{\mu\nu}\right] \\ - \frac{\lambda_1}{2}\sigma_\lambda^{\langle\mu}\sigma^{\nu\langle\lambda} + \frac{\lambda_2}{2}\sigma_\lambda^{\langle\mu}\omega^{\nu\rangle\lambda} - \frac{\lambda_3}{2}\omega_\lambda^{\langle\mu}\omega^{\nu\rangle\lambda} .\end{aligned} \tag{1.53}$$

It is valid to replace $\sigma^{\mu\nu} \to \pi^{\mu\nu}/\eta = \Pi^{\mu\nu}/\eta$, in order to solve it numerically:

$$\begin{aligned}\Pi^{\mu\nu} = \eta\nabla^{<\mu}u^{\nu>} - \tau_\pi\left(\nabla_\alpha^\mu\nabla_\beta^\nu D\Pi^{\alpha\beta} + \frac{4}{3}\Pi^{\mu\nu}\left(\nabla_\alpha u^\alpha\right)\right) \\ - \frac{\lambda_1}{2\eta^2}\Pi_\lambda^{<\mu}\Pi^{\nu>\lambda} + \frac{\lambda_2}{2\eta}\Pi_\lambda^{<\mu}\omega^{\nu>\lambda} - \frac{\lambda_3}{2}\omega_\lambda^{<\mu}\omega_\lambda^{<\mu}\omega^{\nu>\lambda}.\end{aligned} \tag{1.54}$$

Note, that only 4 second-order coefficients left: $\tau_\pi, \lambda_1, \lambda_2, \lambda_3$.

The hydrodynamic code that we use for the calculations presented in this thesis is based on eq. (1.54). It was found that λ_1, λ_2, λ_3 do not affect the boost-invariant hydrodynamic evolution in heavy-ion collision systems [124] so their values were set to zero. The value of relaxation time τ_π is expected to lie in the range $\frac{\tau_\pi}{\eta}(\epsilon + p) = 2.6 - 6$ [124] and is set to $\frac{\tau_\pi}{\eta}(\epsilon + p) = 4$ in our calculations [99].

1.6 Freeze-out

During its expansion the matter created in a heavy-ion collision at some stage reaches the point where hadrons almost stop to interact. This stage is called *thermal* or *kinetic* freeze-out, since after this point the momenta of particles does not change anymore (freeze). It is a phase transition from the strongly coupled matter to a weakly coupled one. The thermal freeze-out takes place when the collision time τ_{coll} becomes larger than the expansion time τ_{exp}. It is common to say that the thermal freeze-out takes place when the mean free path of particles is of the same order of size as the system.

The freeze-out process is complicated, for example particles with different cross sections may freeze-out at a different time and similarly different types of processes may be turned off at different times.

The thermal freeze-out happens after the so-called *chemical* freeze-out. As the system expands and cools down, the inelastic collisions are decreasing and stop at some point, this point is called chemical freeze-out. The temperature of chemical freeze-out is higher than the temperature of thermal freeze-out $T_{ch} > T_{th}$. During the time between chemical and thermal freeze-out, elastic processes and strong decays of heavier resonances are taking place.

In practice the most popular concept is to use fixed final temperature T_f for the thermal freeze-out. It means that all processes in the fluid element stop when the system reaches the temperature T_f during cooling. At the point $T = T_f$ we have a 3D hypersurface in the Minkowski space, where due to hydrodynamic calculations we know the values of hydrodynamic parameters and flow on this hypersurface. After this information is obtained, it is possible to calculate different observables and compare them with existing data. The formalism is based on the utilization of Cooper-Frye formula [37].

The number of particles that decouple on the freeze-out hyperface Σ is

$$N = \int \frac{d^3p}{E_p} \int d\Sigma_\mu(x) p^\mu f(x,p), \tag{1.55}$$

where $f(x,p)$ is the equilibrium distribution.

When system is close to equilibrium, it is possible to describe it with the equilibrium function of Bose or Fermi distribution with an additional viscous correction which must vanish in the limit of ideal hydrodynamics

$$f(p) = f_0 + \delta f(p). \tag{1.56}$$

The correction $\delta f(\mathbf{p})$ depends on the interactions between the particles [125]. There are several types of ansatzs used, the most traditional way is the quadratic ansatz, $\delta f(\mathbf{p}) \propto p^2$ [126], however, a linear ansatz $\delta f(\mathbf{p}) \propto p$ is also often used and gives a good agreement with the data [127].

1.6.1 Other models

Other models exist in order to describe heavy-ion collisions. The so-called hybrid models give a good description of the bulk properties of the quark-gluon plasma. These models are based on hydrodynamics for the early stage and on transport theory for the late stages where the matter is out of equilibrium [112]. Here is an non-exhaustive list of other different approaches:

- transport theory: AMPT [128],
- hybrid models: UrQMD [129],
- thermal models: HRGM [130],
- string decay models: HIJING [131], RQMD [132], HIJET [133], MCMHA [134].

Chapter 2

Directed flow measurements

In hydrodynamics the anisotropic flow is defined through the Fourier decomposition

$$v_n e^{in\Psi_n} = \langle e^{in\phi} \rangle \,, \tag{2.1}$$

where v_n is the magnitude of anisotropic flow [135] and Ψ_n is the reference angle in harmonic n. The average is taken over the distribution of particles. The coefficient v_1 is called the *directed flow*.

The theoretical description of the directed flow was given in the Chapter 1. Thus, it was discussed that due to the fluctuations the directed flow has the component which is even in rapidity, see eq. (1.16). This component was not measured yet by 2012. In this Chapter, we present the first measurements of the v_1^{even} at the LHC. The results of this Chapter were published in ref. [136].

2.1 Two-particle correlations

In order to measure v_1^{even} component of the directed flow, the measurements should be done in such a way that it would be average over rapidity in order to make the odd component v_1^{odd} vanishing. The symmetry of the detector ALICE allows such measurements. v_1^{even} can thus be measured from ALICE data.

In the standard picture of the heavy-ion collisions, the created matter expands and breaks into particles. In hydrodynamics these particles are emitted independently in each event with an azimuthal distribution which fluctuates from one event to another. The two-particle correlation factorizes into the product of two single-particle distributions v_n

$$V_{n\Delta}(p_t^t, p_t^a) = v_n(p_t^t) v_n(p_t^a) \,, \tag{2.2}$$

here we follow a standard practice in correlation studies [14], where one particle

$p_t^{a,t}(N)$	$p_t^a(1)$	$p_t^a(2)$	$p_t^a(3)$	...
$p_t^t(1)$	$V_{n\Delta}(11)$	...	...	...
$p_t^t(2)$	$V_{n\Delta}(21)$	$V_{n\Delta}(22)$	...	...
$p_t^t(3)$	$V_{n\Delta}(31)$	$V_{n\Delta}(32)$	$V_{n\Delta}(33)$	...
...	...	...	...	...

Table 2.1: The $N \times N$ symmetric matrix $V_{n\Delta}$.

is referred to as "trigger" particle and labeled with t and another particle is referred to as "associated" particle denoted as a. These particles can be taken from different p_t bins. Currently, the flow is the only known mechanism that produces a factorized correlation at low p_t.

The factorization (2.2) was studied at the LHC in Pb-Pb collisions [14, 137]. The values of $V_{n\Delta}$ are measured for N p_t bins for the trigger and the associated particles. This data are presented in a $N \times N$ symmetric matrix as illustrated in Table. 2.1.

The ALICE collaboration has tested the factorization by fitting the matrix $V_{n\Delta}$ by the expression (2.2) with the v_n as N fit parameters. In the figures 2.1 we see the values of $V_{n\Delta}$ and the values of the ratios $V_{n\Delta}/fit$ where "fit" is $v_n(p_t^t)v_n(p_t^a)$. This ratio is supposed to be close to 1 if the factorization works well. All the values far from 1 means that the factorization breaks and can be considered as a non-flow contribution, see Chapter 1. As it was shown by ALICE, the factorization works well for the low p_t range for $n = 2, 3, 4, 5$, but breaks for $n = 1$ even at low p_t. In the high p_t range the difference can be explained by the presence of jets or by flow fluctuations [138, 139]. The explanation of the results for $n = 1$ can be found in the fact that the first flow harmonic is affected by the additional long-range term due to the momentum conservation [85]. The study of the momentum conservation contribution will be discussed in the next Section.

2.2 Momentum conservation

In this section we rederive the contribution of momentum conservation to $V_{1\Delta}$ [85].

The two-particle distribution can be written as the sum of a factorized product of single particle distributions and the two-particle correlation function in

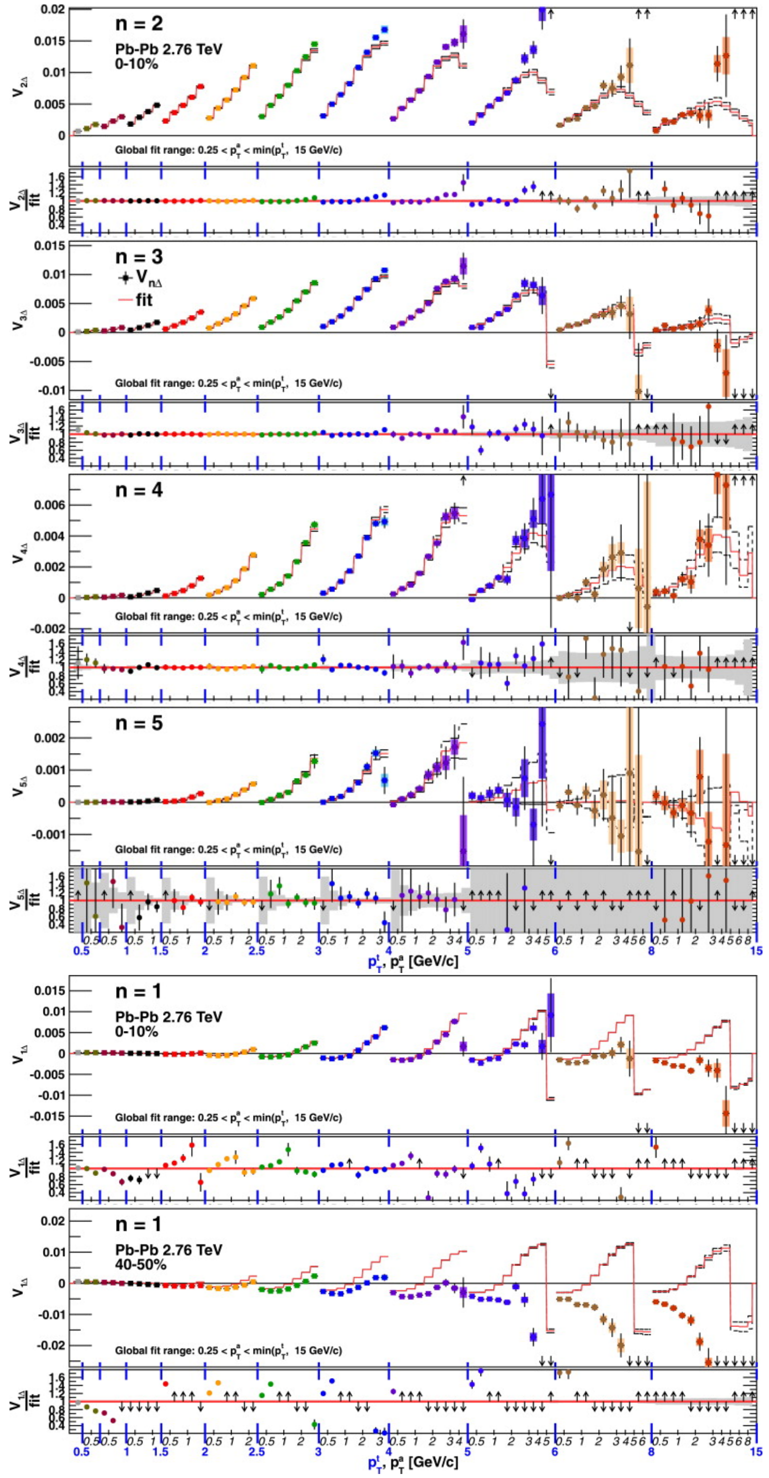

Figure 2.1: Fit results from ALICE collaboration [14]: the measured $V_{n\Delta}$ coefficients plotted on p_t axis (upper plots) and the ratio of the data to the fit $V_{n\Delta}/fit$ (lower plots).

the following way:

$$\frac{dN_{jk}}{d^3\mathbf{p_1}d^3\mathbf{p_2}} = \frac{dN_j}{d^3\mathbf{p_1}}\frac{dN_k}{d^3\mathbf{p_2}}\left(1 + C_{jk}(\mathbf{p}_1, \mathbf{p}_2)\right) \,, \tag{2.3}$$

where $C_{jk}(\mathbf{p}_1, \mathbf{p}_2)$ is the connected two-particle correlation function responsible for the non-flow contribution. We denote $\mathbf{p}_1, ...\mathbf{p}_N$ the momenta of N particles emitted in a heavy ion collision. We are interested in azimuthal correlations, so we consider only the transverse momenta $\mathbf{p_t}_1, ...\mathbf{p_t}_N$. Global momentum conservation yields back-to-back correlations between the outgoing particles. Following ref. [85] we compute the momentum conservation contribution $C_{jk}^{\sum p_t}(\mathbf{p}_1, \mathbf{p}_2)$ to the $C_{jk}(\mathbf{p}_1, \mathbf{p}_2)$ function. The transverse momentum conservation reads:

$$\mathbf{p_t}_1 + ... + \mathbf{p_t}_N = 0\,. \tag{2.4}$$

We want to calculate two-particle distribution of $\mathbf{p}_1, \mathbf{p}_2$, namely $f(\mathbf{p}_1, \mathbf{p}_2)$. If momentum conservation is the only source of correlations then the distribution of $\mathbf{p}_1, ...\mathbf{p}_N$ is defined as

$$f_c(\mathbf{p}_1, ..., \mathbf{p}_k) = \frac{\left(\prod_{i=1}^{k} f(\mathbf{p}_i)\right) \int \delta^2(\mathbf{p_t}_1 + ... + \mathbf{p_t}_N) \prod_{i=k+1}^{N} (f(\mathbf{p}_i) d^3\mathbf{p}_i)}{\int \delta^2(\mathbf{p_t}_1 + ... + \mathbf{p_t}_N) \prod_{i=1}^{N} (f(\mathbf{p}_i) d^3\mathbf{p}_i)}\,, \tag{2.5}$$

where $k < N$ and $f(\mathbf{p})$ is the single particle normalized transverse momentum distribution. The average transverse momentum is assumed to be zero:

$$\langle \mathbf{p_t} \rangle \equiv \int \mathbf{p_t} f(\mathbf{p}) d^3\mathbf{p} = 0\,. \tag{2.6}$$

The statement (2.6) is in agreement with experimental results [8].

The transverse momentum distribution is assumed isotropic in the transverse plane because the effect of azimuthal asymmetries is of the order of a few percent. According to the central limit theorem, the sum of M uncorrelated momenta

$$\mathbf{P_t} = \sum_{i=1}^{M} \mathbf{p_t}_i \tag{2.7}$$

has a gaussian distribution if M is large:

$$F_M(\mathbf{P_t}) = \int \delta^2 \left(-\mathbf{P_t} + \sum_{i=1}^{M} \mathbf{p_t}_i \right) \prod_{i=1}^{M} \left(f\left(\mathbf{p}_i\right) d^3\mathbf{p}_i \right) = \frac{1}{\pi\sigma^2} \exp\left(-\frac{\mathbf{P_t}^2}{\sigma^2} \right)\,, \tag{2.8}$$

where the square of the width reads

$$\sigma^2 = \left\langle \mathbf{P_t}^2 \right\rangle = M \left\langle p_t^2 \right\rangle \tag{2.9}$$

Taking into account eqs. (2.8) and (2.9) the distribution (2.5) can be written as

$$\begin{aligned}
f_c(\mathbf{p}_1, ..., \mathbf{p}_k) &= \frac{\left(\prod_{i=1}^{k} f(\mathbf{p}_i)\right) \int \delta^2 \left(\sum_{i=1}^{k} \mathbf{p_t}_i + \sum_{i=k+1}^{N} \mathbf{p_t}_i\right) \prod_{i=k+1}^{N} \left(f\left(\mathbf{p}_i\right) d^3\mathbf{p}_i\right)}{\int \delta^2 \left(0 + \sum_{i=1}^{N} \mathbf{p_t}_i\right) \prod_{i=1}^{N} \left(f\left(\mathbf{p}_i\right) d^3\mathbf{p}_i\right)} \\
&= \left(\prod_{i=1}^{k} f(\mathbf{p}_i)\right) \frac{F_{N-k}\left(-\sum_{i=1}^{k} \mathbf{p_t}_i\right)}{F_N\left(0\right)} \\
&= \left(\prod_{i=1}^{k} f(\mathbf{p}_i)\right) \frac{\sigma_N^2}{\sigma_{N-k}^2} \exp\left(-\frac{(\sum_{i=1}^{k} \mathbf{p_t}_i)^2}{\sigma_{N-k}^2}\right) \\
&= \left(\prod_{i=1}^{k} f(\mathbf{p}_i)\right) \frac{N}{N-k} \exp\left(-\frac{(\sum_{i=1}^{k} \mathbf{p_t}_i)^2}{(N-k)\left\langle {p_t}^2\right\rangle}\right). \qquad (2.10)
\end{aligned}$$

Now the expressions for the cases $k = 1$ and $k = 2$ can be obtained.

In the case $k = 1$, expanding the expression to the leading order $1/N$ we get

$$f_c(\mathbf{p}) = f(\mathbf{p}) \frac{N}{N-1} \exp\left(-\frac{\mathbf{p_t}^2}{(N-1)\left\langle {p_t}^2\right\rangle}\right) \sim f(\mathbf{p}) \left(1 + \frac{1}{N} - \frac{\mathbf{p_t}^2}{N\left\langle p_t^2\right\rangle}\right). \qquad (2.11)$$

For the case with two particles the distribution (2.10) reads as

$$\begin{aligned}
f_c(\mathbf{p}_1, \mathbf{p}_2) &= f(\mathbf{p}_1) f(\mathbf{p}_2) \frac{N}{N-2} \exp\left(-\frac{(\mathbf{p_t}_1^2 + \mathbf{p_t}_2^2)}{(N-2)\left\langle {p_t}^2\right\rangle}\right) \\
&\sim f(\mathbf{p}_1) f(\mathbf{p}_2) \left(1 + \frac{2}{N} - \frac{(\mathbf{p_t}_1^2 + \mathbf{p_t}_2^2)}{N\left\langle p_t^2\right\rangle}\right). \qquad (2.12)
\end{aligned}$$

According to (2.3), the two-particle correlation due to momentum conservation has a form:

$$C^{\sum p_t}(\mathbf{p}_1, \mathbf{p}_2) = \frac{f_c(\mathbf{p}_1, \mathbf{p}_2)}{f_c(\mathbf{p}_1) f_c(\mathbf{p}_2)} - 1 = -\frac{2\mathbf{p_t}_1 \mathbf{p_t}_2}{N\left\langle p_t^2\right\rangle}. \qquad (2.13)$$

The first Fourier coefficient $V_{1\Delta}(p_t^t, p_t^a) = \langle \cos\Delta\phi\rangle$ can be written in a way (2.2):

$$\langle \cos\Delta\phi\rangle = v_1(p_t^t) v_1(p_t^a) + \langle \cos\Delta\phi\rangle_{corr}, \qquad (2.14)$$

where the correction $\langle \cos\Delta\phi\rangle_{corr}$ due to momentum conservation (2.13) reads

$$\langle \cos\Delta\phi\rangle_{corr} = -\frac{p_t^t p_t^a}{N\left\langle p_t^2\right\rangle}. \qquad (2.15)$$

Thus (2.2) can be rewritten in the final form with the additional non-flow term:

$$V_{1\Delta}(p_t^t, p_t^a) = v_1(p_t^t)v_1(p_t^a) - k p_t^t p_t^a \,, \tag{2.16}$$

where k is the coefficient of momentum conservation [140]. Note that the non-flow correlation also factorizes in this particular case, but the sum does not.

Following (2.15), coefficient k can be calculated as

$$k = \frac{1}{N \left\langle p_t^2 \right\rangle} \,. \tag{2.17}$$

This coefficient will be estimated in two different ways in the following section.

2.3 Extraction of directed flow from two-particle correlations

In order to extract v_1 from the values of two-particle correlations measured by ALICE collaboration, we use the formula (2.16). The left side of this equation represents the $N \times N$ matrix which we fit with the right part of the equation using $N + 1$ parameter: N values of $v_1(p_t)$ and one additional parameter k. Note, that the fit of ALICE collaboration

$$V_{1\Delta}(p_t^t, p_t^a) = v_1(p_t^t)v_1(p_t^a) \tag{2.18}$$

had N parameters instead of $N + 1$. Table 2.2 compares the quality of the χ^2 fit to $V_{1\Delta}$ using the eqs. (2.18) and (2.16) respectively. One more additional parameter k noticeably improve the fit for all the centralities. It was checked that the values of the fit parameters v_1 and k depend little on the chosen p_t window. However if we include higher p_t values, the quality of the fit gets worse [14]. The entire range of valuesis included as a systematic error bar, this uncertainty is obtained by varying the lower value of p_t cutoff between $0.25 - 0.75$ GeV, and the upper cutoff in the range of $2.5 - 15$ GeV. These uncertainties are presented in the table 2.2. The same procedure was used also later in order to estimate systematic uncertainties in the extracted values of v_1.

The second way to extract the parameter k uses the theoretical definition (2.17) which we rewrite in the following way:

$$k = \frac{1}{\left\langle \sum_i p_t^2 \right\rangle} \,, \tag{2.19}$$

where the sum runs over all particles emitted in one event, and angular brackets denote an average over events in the centrality class. In order to calculate the momentum conservation coefficient, it is needed to know the total number of particles. The problem is that experiments measure only charged particles and only in a restricted phase-space window. Due to this fact, only rough estimation could be done with the eq. (2.19). A computation of the number of particles in the full p_t range is needed. For this, the extrapolatation of the spectra outside the p_t acceptanceis required. In order to extrapolate the spectra the analytic function in order to fit the spectra should be found. In order to fit the preliminary identified particle p_t spectra measured by ALICE collaboration at midrapidity [15] we have tested 3 functions.

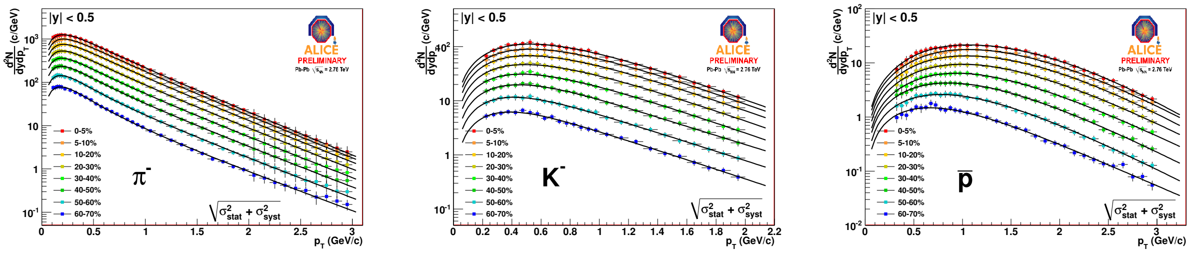

Figure 2.2: The preliminary identified particle spectra measured by ALICE collaboration at midrapidity [15], from left to right: pions, kaons, protons.

First, the following functions were tested:

$$\frac{d^2N}{dydp_t} = A \cdot p_t e^{-\frac{\sqrt{p_t^2+m^2}}{T}} \tag{2.20}$$

and

$$\frac{d^2N}{dydp_t} = B \cdot p_t \left(1 + \frac{p_t}{p_0}\right)^{-n}, \tag{2.21}$$

where A, B, p_0 are fit parameters. Then, the fits were performed with Levy (or Tsallis) fit functions [141]:

$$\frac{d^2N}{dydp_t} = N_0 p_t \frac{(n-1)(n-2)}{nC(nC + m(n-2))} \left(1 + \frac{\sqrt{p_t^2 + m^2} - m}{nC}\right)^{-n}, \tag{2.22}$$

where $N_0 = dN/dy$, n and C are the parameters of Levy function and m is the mass of particles used in the spectra: pions, kaons and protons.

The Levy formula gave better fit than other functions. This is in agreement with ref. [142]. This function is now widely used by collaborations [141]. With the Levy function fit, the spectra was extrapolated outside the p_t acceptance of the detector. In order to calculate $\langle p_t^2 \rangle$ for each type of the particles we use

$$\langle p_t^2 \rangle = \frac{\int p_t^2 \frac{d^2N}{dydp_t} dp_t}{\int \frac{d^2N}{dydp_t} dp_t} . \tag{2.23}$$

In order to extrapolate the spectra to all rapidities, we assume that p_t spectra are independent of rapidity. We use the total charged multiplicity N_{ch}^{tot} from the fig. 2.3 calculated by ALICE collaboration [143].

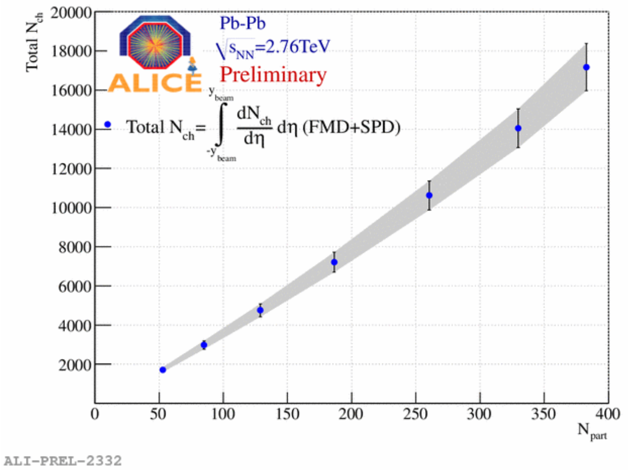

Figure 2.3: Total number of charged particles N_{ch}^{tot} as a function of number of participants N_{part}.

In order to take into account the neutral particles we assumed isospin symmetry and neglected the contribution of particles heavier than nucleons.

Knowing dN/dy as a fit parameter of the Levy function eq. (2.22) for each type of the particles, calculating $\langle p_t^2 \rangle$ with eq. (2.23) and extracting the N_{ch}^{tot}, we finally get

$$\left\langle \sum p_t^2 \right\rangle = N_{ch}^{tot} \frac{3[\langle p_t^2 \rangle dN/dy]_\pi + 4[\langle p_t^2 \rangle dN/dy]_K + 4[\langle p_t^2 \rangle dN/dy]_p}{2[dN/dy]_\pi + 2[dN/dy]_K + 2[dN/dy]_p} , \tag{2.24}$$

where the coefficients in the numerator mean total number of particles and in the denominator mean the number of charged particles.

The resulting estimated value of k is shown in the last column of the table 2.2. The fit results have the same order of magnitude as the estimated value and they increase with the centrality procentage. However, the fit values of k are increasing quicker than for estimated k. Unfortunately, we do not know the reason of such behavior. The discrepancy in k has almost no effect on the

Centrality	χ^2, Eq.(2.18)	χ^2, Eq.(2.16)	k_{fit}	$\langle\sum p_t^2\rangle^{-1}$
0–10%	6	2.0	$2.5^{+1.1}_{-0.3}$	6.2
10–20%	16	1.7	$4.7^{+1.4}_{-0.4}$	8.9
20–30%	45	2.2	$10.2^{+2.1}_{-0.5}$	13
30–40%	75	2.2	$20.6^{+3.2}_{-1.6}$	21
40–50%	126	2.4	$41.5^{+4.7}_{-3.0}$	35

Table 2.2: From left to right: χ^2 per degree of freedom of the fit to the ALICE $V_{1\Delta}$ (restricted to $p_t < 4$ GeV$/c$) using Eq. (2.18), and using Eq. (2.16); value of k from the fit; estimated value of k from momentum conservation, both in units of $10^{-5}(\text{GeV}/c)^{-2}$.

extracted directed flow values and this ambiguity was also included in the error bar for the extracted v_1 values which is shown in fig. 4.1.

The resulting extracted values of the directed flow are presented in the fig. 2.4. The v_1 component is showing negative results at low p_t unlike the v_2 and v_3 components which are positive in all the p_t range. This is explained by the condition that the net transverse momentum of the system is zero, i.e. $\langle p_t v_1(p_t)\rangle = 0$ which implies that low p_t particles flow in the opposite direction to the high p_t particles. From the fig. 2.4 we can see the dependence of v_1 on centrality, showing larger values of v_1 for more peripheral collisions. The v_1 components originates from the fluctuations, and the fluctuations are more important for smaller systems, i.e. for more peripheral collisions. The magnitude of v_1^{even} is several times more than the measured v_1^{odd} magnitude which is denoted as "odd" in fig. 2.6.

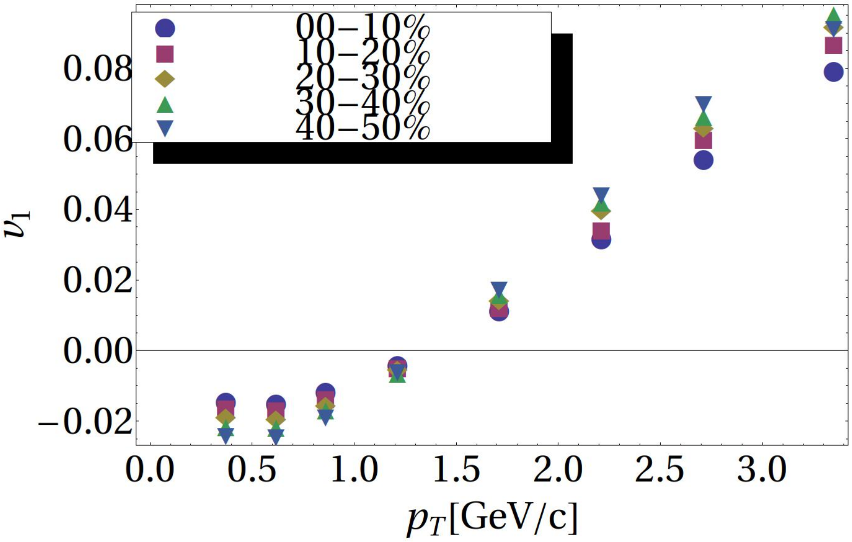

Figure 2.4: First measurement of v_1 at the LHC.

The resulting $v_1(p_t)$ can be considered as a reliable measurement of directed flow v_1 for the LHC. These data were later confirmed by the ATLAS collabo-

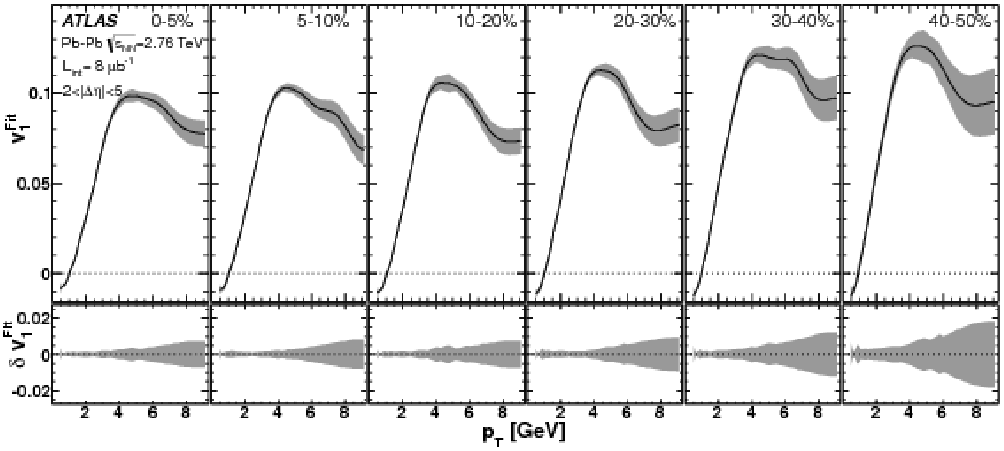

Figure 2.5: v_1 at the LHC: ATLAS with two-particle correlations method [16].

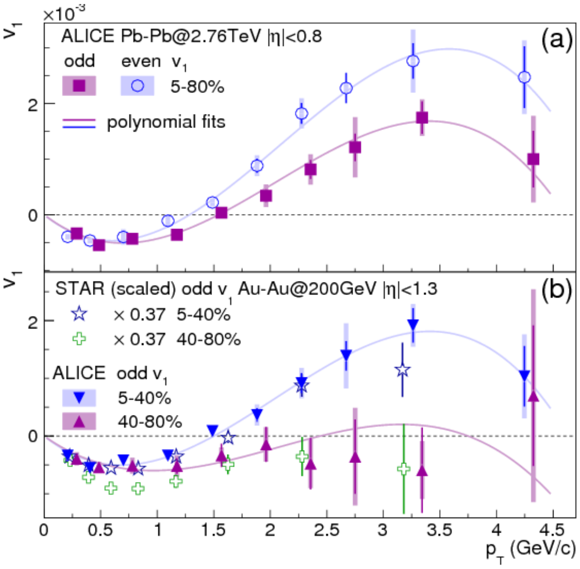

Figure 2.6: v_1 at ALICE with the spectators method [8].

ration [16] which also used the method of two-particle correlations in order to extract the v_1 values.

Later in 2013, another attempt to measure the v_1^{even} was done by ALICE collaboration [8]. They used the detector ZDC which registers the spectators. If for ATLAS results the v_1 component changes of sign at transverse momenta around 1 GeV/c, for ALICE the cross-point is at 1.2-1.5 GeV/c. The magnitude that was observed in this estimation was 40 times smaller than at ATLAS and in our calculations, see fig. 2.6. The measurements of ALICE were done with respect to the collision plane defined by the spectator nucleons Ψ_{SP}, see fig. 1.10, while the measurements of ATLAS were done with respect to the collision plane defined by participants $\Psi_{PP}^{(1)}$. This difference in the magnitudes of measured directed flow gives $\langle\cos\left(\Psi_{PP}^{(1)}-\Psi_{SP}\right)\rangle = v_1\{\Psi_{PP}^{(1)}\}v_1\{\Psi_{SP}\} << 1$, i.e. that fluctuating participant and spectator collision symmetry planes are weakly correlated.

Chapter 3

First viscous hydrodynamic modeling of the directed flow v_1

Relativistic viscous hydrodynamics has been a successful theory for the predictions of flow coefficients v_n for $n = 2, 3, 4$ [13]. Here I present the first viscous hydro calculations of directed flow v_1.

By definition in hydrodynamics v_1 is

$$v_1 e^{i\Psi_1} \equiv \langle e^{i\phi} \rangle \,, \tag{3.1}$$

where Ψ_1 is the corresponding event-plane angle and the average is taken over the momentum distribution [144]. At midrapidity for AA collisions the symmetry $\phi \to \phi + \pi$ takes place, so odd flow harmonics like v_1 and v_3 are naturally zero. These odd flow components appear due to initial geometry fluctuations. In order to study the initial states we perform hydrodynamic simulations of the directed flow v_1 which can be compared to experimental data on v_1, extracted in the previous Chapter. These calculations could also show the dependence of directed flow on viscosity which is unknown.

The results of this Chapter were published in ref. [136].

3.1 Hydrodynamic modeling of directed flow at LHC

The hydrodynamic modeling usually has 3 main steps: one put energy density profile as initial conditions, then one evaluates the system with hydrodynamics and finally one converts the fluid into particles at freeze-out.

In event-by-event ideal hydro calculations v_1 was found with good approximation to be proportional [61] to the dipole asymmetry of the system ε_1

$$v_1 \propto \varepsilon_1 \,, \tag{3.2}$$

where the dipole asymmetry ε_1 is defined as [60]:

$$\varepsilon_1 \equiv \frac{|\{r^3 e^{i\phi}\}|}{r^3}, \tag{3.3}$$

the average is taken over initial energy density after recentering the coordinate system, $\{re^{i\phi}\} = 0$.

We use 2+1D single-shot viscous hydrodynamic calculations with a smooth initial profile $\epsilon(r, \phi)$. This profile is taken from the optical Glauber model [93] and is symmetric with respect to the reaction plane, see fig. 1.18. With such profile the value of ε_1 and accordingly the value of v_1 is zero due to the symmetry. In order to create the dipole asymmetry we deform the profile in the following way:

$$\epsilon(r, \phi) \to \epsilon\left(r\sqrt{1 + \delta\cos\left(\phi - \Phi_1\right)}, \phi\right), \tag{3.4}$$

where δ is a small parameter and $\varepsilon_1 \propto \delta$ for $\delta << 1$, Φ_1 is the dipole asymmetry angle. For the central collisions the direction of v_1 is Φ_1, but for the non-central collisions it is not strictly true because of additional non-linear correlations of v_1 with v_2 and v_3 [145]. Our calculation is averaged over Φ_1. This deformation is illustrated in fig. 3.1.

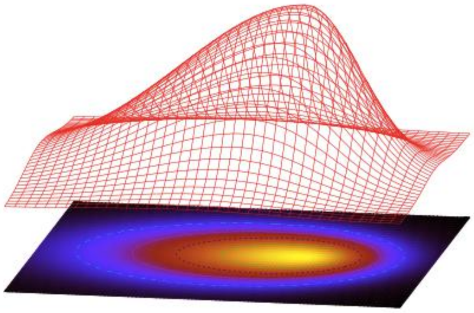

Figure 3.1: Deformed initial energy-density profile.

At the next step of modeling we run the hydrodynamic evolution equations corresponding to eq. (1.54). This hydrodynamic evolution is stopped when the system reaches the freeze-out temperature T_{fr} and the fluid is converted into particles. The resonances are taken into account in this calculation in the following way: the decays of unstable particles are calculated from the particle spectra obtained after freeze-out calculation. The modified program AZHYDRO [146] is used to perform these calculations.

The resulting hydrodynamic calculations of v_1/ε_1 with different parameters of viscosity are presented in the fig.3.2. We choose to present the ratio v_1/ε_1 and not v_1 in order to be independent on the initial state model. A slight dependence on the models was pointed out in ref. [18], but we ignore it in our calculations.

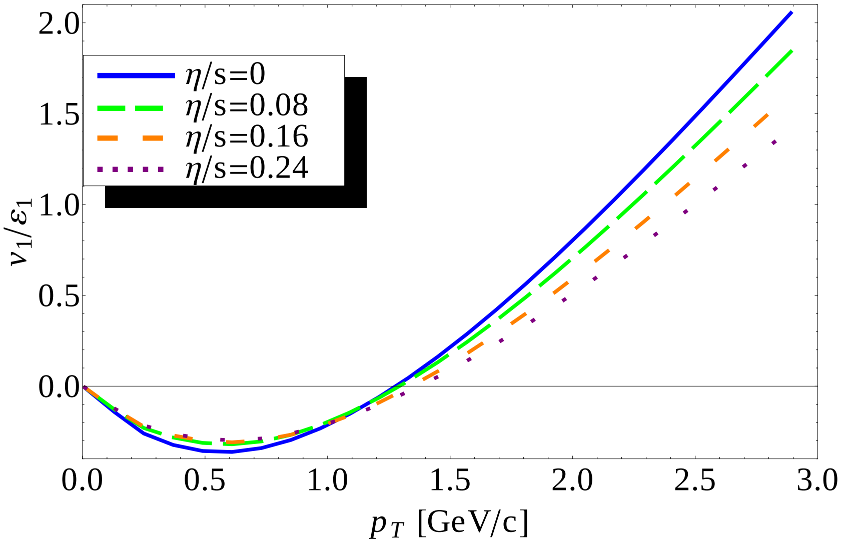

Figure 3.2: v_1/ε_1 vs p_t for central collisions.

Note, that the dependence of v_1 on p_t has the same behavior as for experimental values extracted in the Chapter 2, in hydrodynamic calculations the net transverse momentum of the system is set to zero.

In our calculations we used the ratio viscosity over entropy η/s as a free parameter and varied it as $\eta/s = 0, 0.08, 0.16, 0.24$. Dependence of v_1/ε_1 on viscosity in the fig.3.2 shows that with higher values of viscosity we have less flow. This effect can be explained due to the fact that flow is created by the interactions. If there were no interactions there would be no flow. The viscosity is approximately inversely proportional to the cross-section, so with larger viscosity one has smaller interactions which leads to less flow.

The flow harmonics v_n are expected to have an increasing sensitivity to viscosity because smaller systems are more sensitive to the viscous effects. Indeed, we find that v_1 is less sensitive to viscosity than v_2 [43] and other higher harmonics [13, 74]. This effect is illustrated in the fig. 3.3. In this figure we see the ratio of the flow coefficient calculated with the value of viscosity $\eta/s = 0.08$ to the flow coefficient calculated with $\eta/s = 0.24$. For n=1 this ratio is close to 1 which demonstrates that directed flow is slightly dependent on the viscos-

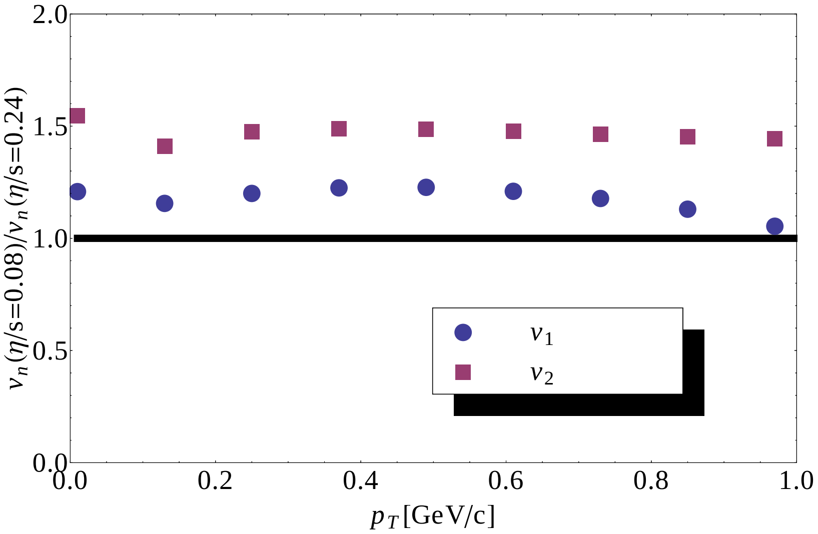

Figure 3.3: $v_n(\eta/s = 0.08)/v_n(\eta/s = 0.24)$, comparison of the ratio values of v_n with different viscosities, $n = 1, 2$.

ity. The ratio for $n = 2$ is closer to 1.5, so the elliptic flow v_2 shows stronger dependence on viscosity than directed flow.

This insensitivity to viscosity combined with the approximate proportionality $v_1 \propto \varepsilon_1$, provides a unique opportunity to place a direct constraint on the dipole asymmetry of the early-time stage and to exclude some models of initial state. Such constraints will be done in the next Chapter.

3.2 Viscous hydrodynamic predictions for directed flow at RHIC

In this section we show predictions for the directed flow v_1 for RHIC energies.

In order to compare hydrodynamic data at the LHC with the experimental values we write

$$v_1^{LHC} = \left(\frac{v_1}{\varepsilon_1}\right)_{hydro}^{LHC} \varepsilon_1^{best} . \tag{3.5}$$

In the left-hand side, v_1^{LHC} denotes the directed flow extracted from data as shown in Chapter 2. In the right-hand side, the values $(v_1/\varepsilon_1)_{hydro}^{LHC}$ are viscous hydrodynamic calculations. The ε_1^{best} is the parameter which we tune in order to get the best fit to the data. We assume little change in the average dipole asymmetry in a centrality bin. The value of ε_1^{best} at LHC is obtained by taking the best fit to the experimental v_1 for $p_t < 1.5$ GeV/c, which is the range where hydrodynamics agrees best with data [144]. The best value ε_1^{best} calculated for

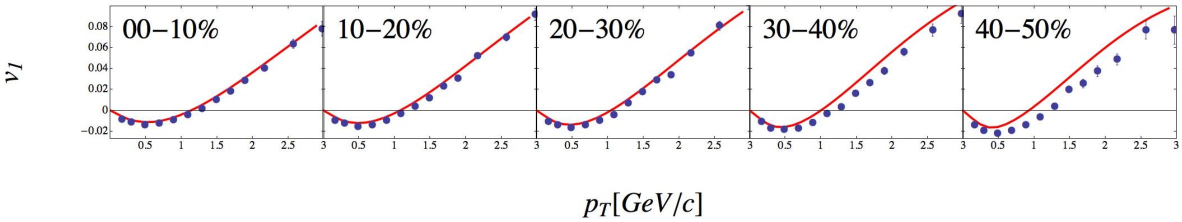

Figure 3.4: $v_1(p_t)$, hydrodynamic predictions (curve) for RHIC, compared with measured experimental data (points). Data are taken from Y.Pandit proceedings, QM2012 [17].

LHC can be applied at RHIC energies, as ε_1 change little with the energy of collisions.

Then $\left(\frac{v_1}{\varepsilon_1}\right)_{hydro}$ is calculated for Au-Au collisions with RHIC energies. Our calculations use $\eta/s = 0.16$ both at LHC and at RHIC, but the extrapolation from LHC to RHIC are almost independent of η/s [124]. Thus, the predicted values of v_1 at RHIC are:

$$v_1^{RHIC} = \left(\frac{v_1}{\varepsilon_1}\right)_{hydro}^{RHIC} \varepsilon_1^{LHC} \, . \tag{3.6}$$

Later our data were compared with experimental data from RHIC, as it is shown on Fig. 3.4 [17]. Our result was found to be well consistent with the data at low transverse momentum and in central collisions.

Chapter 4

Constraining models of initial conditions using anisotropic flow data

One of the most important topics in heavy-ion physics is the understanding of the initial state. In hydrodynamics, initial conditions means the initial energy-density profile at thermalization time t_0 [147]. This profile is not smooth and fluctuates due to the wave-functions of the incoming nuclei. The magnitude of these fluctuations is still unconstrained by the data.

Many models exist in order to describe the initial state. These models predict different values for the transport coefficients in order to match the data. In particular, by tuning the value of η/s [148], the experimental data can be fitted with one model or another [43]. Thus, it is important to understand which of these models are physically reliable. We propose a systematic approach for constraining models of initial conditions using the anisotropic flow data.

In this Chapter, we present two different methods to constrain models of initial state. The first of them is using the data on directed flow v_1, these data are rms values. We compare them to v_1/ε_1 values from hydrodynamics with different values of viscosity and extract the allowed range on rms values of ε_1 depending on centrality. Computing ε_1 in different Monte Carlo models, one could compare them with the allowed range. In the second method we use the combination of the experimental data on v_2 and v_3, these data are also rms values. We compare experimental values with hydrodynamic calculations of v_n/ε_n, $n = 2, 3$. By varying the free parameters in hydrodynamic calculations, we extract the allowed region on the plane (rms ε_2, rms ε_3). Computation of (rms ε_2, rms ε_3) values in Monte Carlo models allows to make a comparison with the extracted range and constrain some of the models.

The results of this Chapter were published in refs. [136, 149, 150].

4.1 Linear response

One of the most remarkable features of the first three flow harmonics v_n is that hydrodynamic response to the initial state is dominated by the linear response. Thus, it was shown that v_n is with a good approximation proportional [151] to the initial eccentricity ε_n

$$v_n \propto \varepsilon_n \,, \tag{4.1}$$

for $n < 4$. Higher flow harmonics have additional non-linear terms and will be discussed in the Chapter 5.

For the directed flow the dipole asymmetry ε_1 of the initial system is defined as

$$\varepsilon_1 \equiv \frac{|\int r^3 e^{i\phi}\epsilon(r,\phi) r\mathrm{d}r\mathrm{d}\phi|}{\int r^3 \epsilon(r,\phi) r\mathrm{d}r\mathrm{d}\phi} \,, \tag{4.2}$$

where the integration is over the transverse plane in polar coordinates, the $\epsilon(r,\phi)$ is the energy density at $z \sim 0$. The average is calculated after the *recentering coordinate system* as

$$\int r e^{i\phi}\epsilon(r,\phi) r dr d\phi = 0 \,. \tag{4.3}$$

For the elliptic flow the ellipticity ε_2 is defined as [90]

$$\varepsilon_2 \equiv \frac{|\int r^2 e^{i2\phi}\epsilon(r,\phi) r\mathrm{d}r\mathrm{d}\phi|}{\int r^2 \epsilon(r,\phi) r\mathrm{d}r\mathrm{d}\phi} \,, \tag{4.4}$$

where recentering is taken into account as in (4.3) .

The triangular flow v_3 is generated by fluctuations in the initial state with triangular form. The triangular flow is proportional to the initial participant triangularity ε_3 [152] which can be defined in two different ways. A first definition that was used earlier is given by

$$\varepsilon_3 \equiv \frac{|\int r^2 e^{i3\phi}\epsilon(r,\phi) r\mathrm{d}r\mathrm{d}\phi|}{\int r^2 \epsilon(r,\phi) r\mathrm{d}r\mathrm{d}\phi} \,. \tag{4.5}$$

According to [60, 153], the definition should be

$$\varepsilon_3 \equiv \frac{|\int r^3 e^{i3\phi}\epsilon(r,\phi) r\mathrm{d}r\mathrm{d}\phi|}{\int r^3 \epsilon(r,\phi) r\mathrm{d}r\mathrm{d}\phi} \,, \tag{4.6}$$

with (4.3) taken into account.

We will use the definition given by eq. (4.6).

4.2 Constraining models of initial state with v_1 data

The first Fourier coefficient v_1 originates from dipole deformation characterized by the dipole asymmetry ε_1. As it was shown in Chapter 3, the directed v_1 is less affected by viscous effects than the higher harmonics. This fact provides a good opportunity to put direct constraints on the dipole asymmetry ε_1 of the initial system, defined as (4.2).

The procedure is the following: we extract the experimental values of v_1 from two-particle correlation data of ALICE as it is shown in Chapter 2, then we run viscous hydrodynamics calculations and we get v_1/ε_1 as it is described in Chapter 3.

We want to compare hydrodynamic data with the experimental values. For this goal we compute

$$v_1 = \left(\frac{v_1}{\varepsilon_1}\right)_h \varepsilon_1^{tune} . \tag{4.7}$$

The value of ε_1^{tune} which fits the experimental data in all the p_t range does not exist. By tuning this parameter, we can obtain a good fit either in the low p_t range, or in the high p_t range as shown in fig. 4.1. In the first case we overpredict data in the upper range whereas in the second case we overpredict data in lower range. The idea is then to match the data with one set of data from below and with another set from above for a given viscosity. The values of ε_1^{tune} obtained after fitting the data establish upper and lower bounds on the actual value.

Fig. 4.1 displays v_1 versus p_t. The experimental points are extracted from ALICE correlation data, as discussed in Chapter 2. The two lines shown in fig. 4.1 correspond to the two sets of values of v_1 calculated with the eq. (4.7) with two different values of viscosity. One of them fits the data from below and another one from above. Thus, we take the line with the viscosity $\eta/s = 0$ and fit the data at low p_t and the second line with $\eta/s = 0.24$ and fit the data at high p_t. These lines are chosen in such a way that we get the largest possible range in the values of ε_1^{tune}. The extracted range for $0 < \eta/s < 0.24$ is demonstrated in fig. 4.2 as the light gray bounds.

The extraction of the extreme values of ε_1 is done for all centralities. We show in fig. 4.2 the allowed values of ε_1 as a function of centrality with the rms values from various Monte-Carlo models of initial conditions. The allowed range taking into account viscosity range $0.08 < \eta/s < 0.16$ is also shown in a darker band in order to illustrate the small effect of viscosity. The fact that v_1 has a smaller dependence on viscosity gives a more narrow band of allowed values.

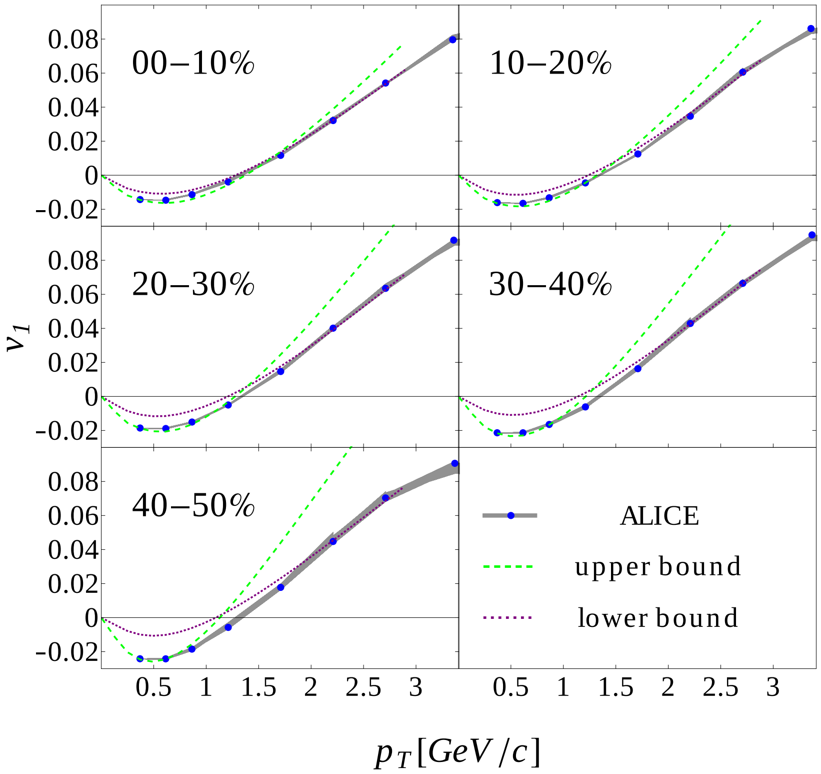

Figure 4.1: v_1 vs p_t for different centrality ranges.

This allows to constrain some models and could not be done with higher-order flow harmonics as good as with v_1.

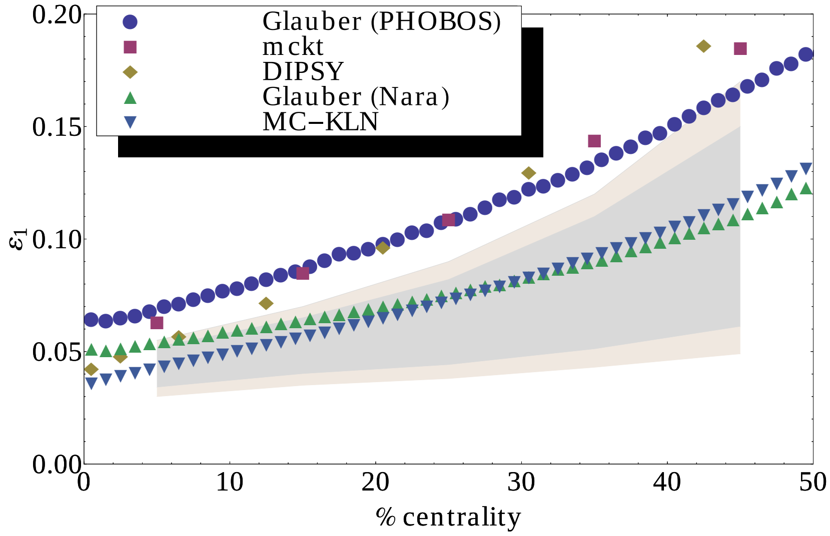

Figure 4.2: Variation of ε_1 with *centrality*. The shaded band represents allowed region: darked band corresponds to the range of viscosities $0.08 < \eta/s < 0.16$ and lighter band correspond to $0 < \eta/s < 0.24$. Symbols are predictions from Monte Carlo models.

4.2.1 Results

In fig. 4.2, we see that two models, MC-KLN [154, 155] Nara [155] are inside the allowed region for all centralities. We see that ALICE data exclude DIPSY [156] above 10% centrality. Two models, PHOBOS Glauber [94] model and an improved mckt model [157, 155] with KNO fluctuations, can be excluded over the full centrality range. Concerning MC Glauber models, the binary collision fraction for both of the models was taken as αN_{coll}, $\alpha = 0.18$ [158]. Since hydrodynamics is more reliable at low p_t, we believe that the real value of ε_1 lies close to the upper bound. The two models which have the largest values of dipole asymmetry only need a small tuning to be inside the allowed region of ε_1. Other models may lead to too low values of ε_1.

This study does not provide strong constraints on the models and in the next section we propose another study for more accurate conclusions.

4.3 Constraining models of the initial state with v_2 and v_3 data

The anisotropic flow is the hydrodynamic response [60] to initial spatial anisotropy of the strongly-interacting system appearing in the initial state of the heavy-ion collision. In this section, we focus on two of corresponding experimental observables: the elliptic v_2 [159, 72] and the triangular v_3 flow coefficients, see fig. 1.12. The main properties of elliptic and triangular flow were discussed in the Chapter 1.

In spite of the fact that v_2 and v_3 are the most studied harmonics of anisotropic flow, many questions remain to be answered. It was found out that both v_2 and v_3 hydrodynamic values can fit the data using different models of initial state by tuning η/s. As it was shown in ref. [43] CGC models predict higher values of initial eccentricity than Glauber model, which gives higher values of the flow for CGC model. The viscous effect decreases the flow, so in order to fit the data with CGC initial conditions thet higher value of viscosity has to be put. However some of the models of initial state are unable to fit both v_2 and v_3 the same time [74, 160]. By combining v_2 and v_3 data we could constrain models of initial state even if the viscosity is unknown.

In order to create the range of allowed values we combine together viscous hydrodynamic calculations with experimental data from RHIC [160] and LHC [10]. These constraints are used later in order to exclude some of the existing models of initial state. This provides a simple method that could be used by any

Monte Carlo group in order to quickly and easily compare their model with the constraints and determine weather or not this model is compatible with the data.

4.3.1 Principle of our approach

In our approach, we focus on the integrated anisotropic flow [161], i.e. the anisotropic flow averaged over p_t. Collaborations have published data of the integrated anisotropic flow coefficients v_n up to the sixth harmonics $n = 6$ [16]. In this study, we deal only with the elliptic and the triangular flow coefficients. The reason why we do not consider here higher order Fourier harmonics of anisotropic flow as v_4, v_5, v_6 is that these components have non-linear additional terms in the hydrodynamic response to the initial state geometry [162, 163, 145, 164], while the elliptic and the triangular flow coefficients are to a good approximation linear in the response to the initial state [165, 151] as it was shown in the first section of this Chapter.

Assuming linear response to the initial anisotropy, the anisotropic flow in an event is $v_n = \kappa_n \varepsilon_n$. The response coefficient κ_n is the same for all events in a centrality bin, but ε_n fluctuates, so that initial-state fluctuations result in event-by-event flow fluctuations. The experimental data of integrated flow are taken from the ALICE and PHENIX collaborations [160, 10]. The ALICE collaboration uses two-particle correlations method in order to extract the data whereas PHENIX collaboration uses an event-plane method. Both methods provide the root-mean-square values (rms) of the event-by-event distribution over a centrality bin of the anisotropic flow v_n [89]. It can therefore be written:

$$\sqrt{\langle \varepsilon_n^2 \rangle} = \frac{\sqrt{\langle (v_n)^2 \rangle}}{\kappa_n}, \tag{4.8}$$

where $\langle ... \rangle$ is an average over collision events, $n = 2, 3$ and $\sqrt{\langle (v_n)^2 \rangle}$ is the measured rms value of the integrated flow. In hydrodynamics, the coefficient κ_n is calculated as $\kappa_n = (v_n/\varepsilon_n)_{hydro}$ and the rms values of ε_2 and ε_3 can be extracted with the eq. (4.8).

There are several free parameters in hydrodynamic calculations which give uncertainties in the hydrodynamic response. These uncertainties are taken into account and are represented by the shadow bands in the (rms ε_3, rms ε_2) plane. As we will discussed in sec 4.3.3 , these uncertainty bands are narrow enough to constrain models of initial state.

4.3.2 Uncertainties in hydro response

Each step of standard hydro modeling [166] induces its own uncertainties [167]. An ideal evaluation that would take into account all these uncertainties would be too expensive [168]. In our calculations we simplify the problem by keeping at each step the main source of uncertainties. In the next section, we will discussed the leading sources of uncertainties.

Viscous effect

The main uncertainty in the hydrodynamics is the value of the shear viscosity. This value is not well constrained neither in theory nor the experiment [169, 167, 170]. We treat η/s as a free parameter that we vary from 0 to 0.24 by steps of 0.04. The hydrodynamic approach can be applied only if η/s is not too large [171]. Though effect of bulk viscosity can be not negligible for some values of temperature [122], its effect on the integrated flow is smaller than those from shear viscosity [172]. Then in the spirit of keeping only the main uncertainty source, we do not take into account the effect of bulk viscosity [173, 174]. The second-order corrections [123] are also not taken into account because they have a small effect [43].

Initial conditions

The optical Glauber model profile is smooth and has already an ellipticity, so automatically gives us elliptic flow values and we can directly compute the values of κ_2. If we want to obtain the values of ε_3 or v_3 with this profile, we get zero values for both of them due to the symmetry. In order to calculate κ_3 we deform the third harmonic in the profile in the similar way as for v_1 [74]:

$$\epsilon(r, \phi) \to (r\sqrt{1 + \varepsilon'_n \cos(n(\phi - \Phi_n))}, \phi) \tag{4.9}$$

where ε'_n is the magnitude of the deformation and Φ_n is the orientation of the deformation. As far as the elliptic deformation does not interfere with the triangular deformation [145, 74], we choose $\Phi_3 = 0$ for our calculations. We also check that the dependence of the ratio $(v_3/\varepsilon_3)_h$ on the values chosen for ε'_3 [74] is negligible. This calculation uses the same values of ε'_3 as [74]. The values of ε'_3 differs from ε_3 by a few percent. Our studies show that recentering (4.3)[1] the distribution in coordinate space after performing the deformation of the profile

---

[1] We found out that in ref. [74] this recentering correction was neglected and the resulting values of hydrodynamic response were lower by up to 10% for peripheral collisions.

by ε_3', shifts the center by a distance which is proportional to $\varepsilon_2\varepsilon_3$. This shift leads to a correction to ε_3 which decreases its value by a term of the relative order of $(\varepsilon_2)^2$.

As the Fourier coefficients have, with a good approximation, a linear response to the initial state, we consider the values of the hydrodynamic response $\kappa_n = v_n/\varepsilon_n$ to be independent on the initial state model. In reality this response is not exactly linear and should depend on the initial state model. These effects were studied in ref. [18] and it was shown that the response have a weak dependence on the initial state model. By comparing in figs. 4.3 and 4.4 the curves for "single-shot" and "event-by-event" calculations for the different models, on can see that the effects are small.

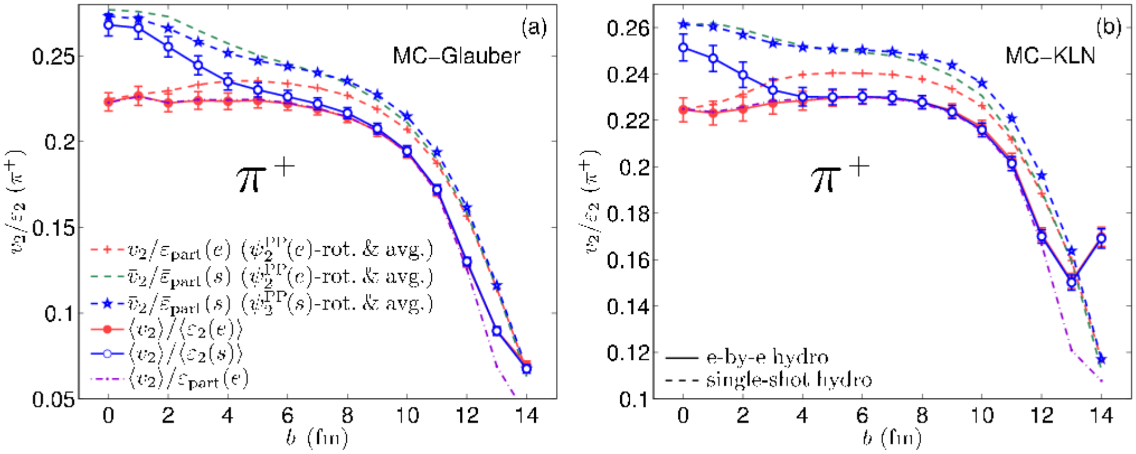

Figure 4.3: v_2/ε_2 dependence on impact parameter for pions. Solid lines correspond to event-by-event hydrodynamics, dashed lines correspond to single-shot hydrodynamics. Left: for MC Glauber initial state model, right: MC-KLN initial state model [18].

In order to estimate the uncertainty on the value of κ_n from the initial profile, we use two definitions of ε_n: with energy density weighting as in eqs. (4.4), (4.6) and entropy density weighting. Both definitions provide reasonable predictions of v_n [163], the difference between the two calculations indicates the size of the uncertainty due to the linear approximation. The deformation of optical Glauber profile as in Eq. 4.9, gives exactly the same values of ε_3 for the central collisions for both types of weighting [74], though in other type of calculations this difference can take place [18]. The values of ε_2 calculated with entropy density weighting and with energy density weighting, are different for the optical Glauber model, so this difference can be used as the part of the error bar in our calculations.

Another free parameter in our calculations is the thermalization time t_0 [147, 144] at which hydrodynamics becomes a good approximation. This parameter is

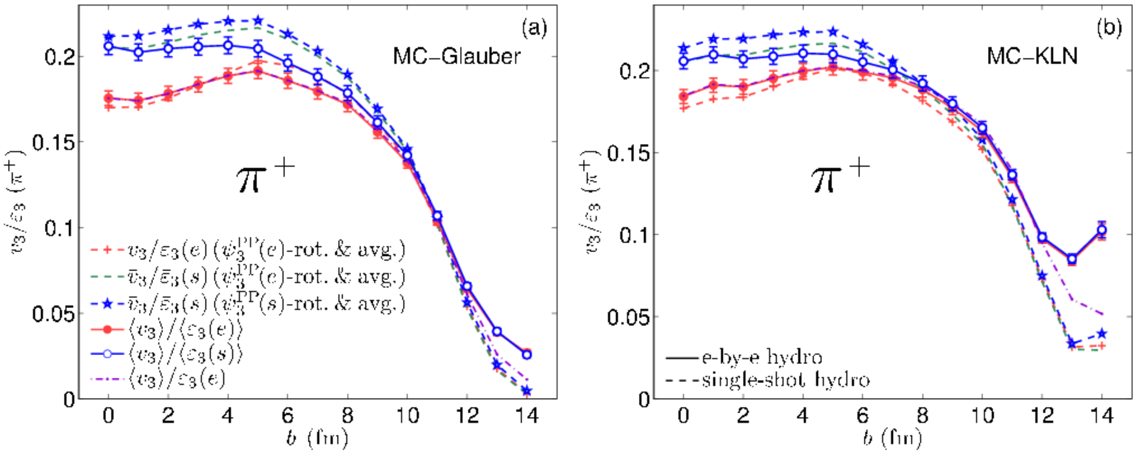

Figure 4.4: v_3/ε_3 dependence on impact parameter for pions. Solid lines correspond to event-by-event hydrodynamics, dashed lines correspond to single-shot hydrodynamics. Left: for MC Glauber initial state model, right: MC-KLN initial state model [18].

not well known. In previous studies [144] the transverse flow expansion before t_0 was neglected. t_0 is typically close to 1 fm/c. In reality the transverse flow exists directly after the collision happened, independently on the fact if the system thermalizes or not. This so-called *initial flow* has given a good explanation of interferometry data [175, 176, 177]. Initial flow is universal [178] and can be obtained in calculation with vanishing flow at t_0, by choosing a very small values [176] of t_0. We would like to take into account the effect of initial flow and thus we choose two values of the thermalization time which are 0.5 fm/c and 1 fm/c. As we vary the thermalization time, we tune the starting temperature T_{start} and the freeze-out temperature T_{fr} in order to match the p_t spectrum.

Freeze-out stage

At some point during its expansion the fluid can be described as a gas of hadrons with collective and thermal motion. The question here is at what point the hydrodynamic approach is still valid. We assume that hydrodynamics is still reasonable in the hadronic stage, using only a single freeze-out temperature [144].

Some other groups use the so-called *afterburners* which simulates hadronic decays and two-body collisions [56, 179, 180]. These afterburners are useful for reproducing the elliptic flow and identified particle spectra, though afterburner have quite a little effect on integrated properties of unidentified hadrons. These afterburners are now used in calculations for both RHIC and at LHC energies [112, 114]. Some groups also use the hydrodynamics with bulk viscosity in the hadronic stage [181] which also successfully generate the properties of identified particles.

In our approach we run hydrodynamic calculations starting from initial time t_0 and we choose the freeze-out temperature T_{fr} in such a way that we would have the average transverse momentum unchanged $\langle p_t \rangle$. Thus choosing smaller values of t_0, we stop the hydro simulation earlier, that means we put larger T_{fr}. We take into account resonance decays, but we neglect hadronic collisions.

In the hadronic part, a significant uncertainty comes from the freeze-out viscous correction [126, 182] which momentum dependence is unknown and involves microscopic information about hadronic cross-sections [125]. Due to this, we make two types of calculations with two possible ansatzs which were introduced in the Chapter 1: the quadratic ansatz $\propto p^2$ [125] which is commonly used, and the linear ansatz $\propto p$ [127] which also gives a reasonable description of the data.

4.3.3 Calculations

In this section we use Glauber optical model for the initial conditions, with the energy density weighted with the linear combination of the number of collisions N_{coll} and the number of participants N_{part} as it was described in the Chapter 1.

The cuts on the transverse momentum p_t and pseudorapidity η used by experiments, are: ALICE collaboration [10] uses $0.2 < p_t < 5$ GeV/c cut for the transverse momentum and $|\eta| < 0.8$ cut for the pseudorapidity, the PHENIX collaboration [160] uses the cuts $0.25 < p_t < 4$ GeV/c and $|\eta| < 0.35$. Our model is independent of rapidity because it is invariant under longitudinal boosts.

Our calculations take into account the difference in rapidity and pseudorapidity [39], as described in Chapter 1. Changing variables from rapidity to pseudorapidity increases v_2 by 3% and v_3 by 4%. In order to suppress non-flow correlations, the ALICE collaboration [87] uses pair correlations with a pseudorapidity gap $|\Delta\eta| > 1$ between particles in the pair. This condition excludes particles at $|\eta| < 0.2$. Since all pairs are weighted the same way, it gives more weight to particles near $|\eta| = 0.8$. We take into account this additional cut in $\Delta\eta$ which decreases v_2 by 0.3 % and v_3 by 0.4%.

After taking into account the uncertainties, we can calculate ε_2 and ε_3 using Eq. (4.8). The resulting values are shown in the fig. 4.5 for the 20–30% centrality range at the LHC. In this figure one hydro calculation with one set of parameters corresponds to one point on the (rms ε_3, rms ε_2) plane. Six types of symbols correspond to different sets of parameters:

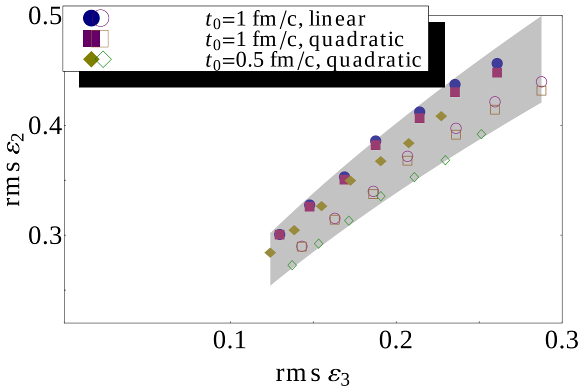

Figure 4.5: (Color online) R.m.s. values of $\varepsilon_2(\varepsilon_3)$ from hydro simulations + ALICE data for 20-30% centrality range. Purple squares correspond to t_{init} = 1 fm/c with quadratic freezeout. Blue circles correspond to t_{init} = 1 fm/c with linear freezeout. Yellow diamonds correspond to t_{init} = 0.5 fm/c with quadratic freezeout. Open symbols mean entropy-density profile used. The shaded band is an allowed band encompassing uncertainty in the extracted values.

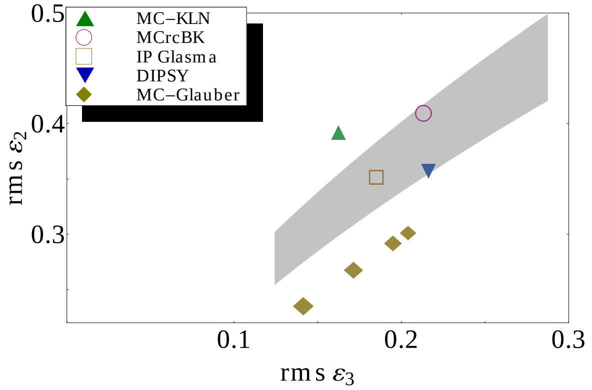

Figure 4.6: (Color online) The shaded band is the same as in fig. 4.5 and represents allowed values. Symbols are predictions from various models of initial state. The MC-Glauber model is shown for different values of the width of gaussian σ=0 fm, 0.4 fm, 0.8 fm and 1.2 fm, which are distinguished by different symbol sizes, showing that changing the smearing parameter has the same effect as changing viscosity.

- blue circles, use as parameters the thermalization time 1 fm/c and the linear ansatz
- purple squares use thermalization time 1fm/c and quadratic ansatz
- yellow diamonds correspond to thermalization time 0.5 fm/c and quadratic ansatz
- open symbols mean that the entropy-density weighting is used.

These symbols are composing six lines with viscosity η/s changing. Each line has seven points, corresponding to seven values η/s = 0, 0.04, 0.08, 0.12, 0.16, 0.2, 0.24 (from left to right).

The difference between the linear and the quadratic ansatz is small, except for high viscosity values which makes the values of ε_2 with quadratic ansatz slightly smaller than for linear ansatz. The difference in the thermalization time gives the resulting decrease of ε_2 and ε_3 values with t_0 = 0.5 fm/c in comparison with the values for t_0 = 1 fm/c. Since the hydro evolution starts earlier, more flow is produced. From the ratio (4.8) it can be seen that if more flow is produced, both values of ε_2 and ε_3 are decreasing.

With the lines drawn on the plane (rms ε_3, rms ε_2), a shaded band is created such that all the points are inside this band as it is shown in the fig. 4.5. This band defines the allowed range. The important fact here is that even with all uncertainties taken into account, we obtain a narrow band, which allows us to constrain models as we show in the fig. 4.6.

Note that the curves can be fitted by a power law function:

$$\sqrt{\langle\varepsilon_2^2\rangle}/\left(\sqrt{\langle\varepsilon_3^2\rangle}\right)^k = \mathcal{C}, \tag{4.10}$$

where the best fits leads to k=0.6 for LHC and k=0.5 for RHIC and where $\mathcal{C}$ is fixed. k can be understood as the ratio of the relative change in v_2 to the relative change in v_3 when viscosity is increasing. Note that for $k < 1$, viscosity has a smaller effect on v_2 than on v_3 as it is expected.

We can determine the range of values for $\mathcal{C}$ by computing the maximum and the minimum values of $\mathcal{C}$ allowed by hydrodynamics. The resulting minimum and maximum values are shown in Table 4.1 and corresponding figure fig. 4.7, showing the allowed $\mathcal{C}$ region for RHIC and Table 4.2 with the fig. 4.8 corresponding to the LHC respectively.

4.3.4 Results

The region of allowed values for $(\varepsilon_3, \varepsilon_2)$ obtained in the previous section can be used to constrain models of initial state. Since ε_3 is solely created by fluctuations we test Monte Carlo models which have fluctuations. We test two types of the models: Glauber type [93] and QCD-inspired models.

The type of the Monte Carlo Glauber model we use, is the PHOBOS Monte Carlo [94] model which we shortly describe in the Chapter 1. Other implementations of MC Glauber [183, 184] are not taken into account here. In this section we differ Glauber models by the participant weighting and denote them as following:

- "Glauber N_{part}" is the Glauber model, where each participant can be given or the equal weight.
- "Glauber N_{coll}" is the Glauber model, where the weight is proportional to the number of collisions
- "Glauber" is the Glauber model, where the weight is taken as the linear combination of N_{part} and N_{coll}.

Among the QCD-inspired models, we test four of them: the oldest QCD model we refer to as MC-KLN [185, 154] which is using k_T factorization and taking into account fluctuations of the positions of the nucleons. The second model MCrcBK [157] is an improved MC-KLN model with additional KNO fluctuations in order to match multiplicity distribution in pp collisions. The third one is the DIPSY [156] model, a QCD model which takes into account the multiple gluon cascade. The last one is the IP Glasma model [186] which does not assume k_T factorization and includes non-linearities and fluctuations of color charges within a nucleon.

Table 4.1: Values of the ratio $\sqrt{\langle\varepsilon_2^2\rangle}/\sqrt{\langle\varepsilon_3^2\rangle}^{0.5}$ at RHIC. First two lines: minimum and maximum values allowed by hydrodynamics and experimental data. Next lines: values predicted by various models.

% centrality	0-10	10-20	20-30	30-40	40-50
minimum	0.36	0.56	0.69	0.75	0.74
maximum	0.41	0.63	0.79	0.90	0.91
MC-Glauber	0.38	0.57	0.69	0.76	0.80
MC-Glauber (N_{coll})	0.44	0.64	0.76	0.81	0.83
MC-Glauber (N_{part})	0.34	0.52	0.64	0.73	0.78
MC-KLN	0.49	0.78	0.95	1.03	1.06
MC-rcBK	0.49	0.73	0.87	0.95	0.98
IP-Glasma	0.43	-	0.76	0.85	-
DIPSY	0.39	0.59	0.72	0.80	0.84

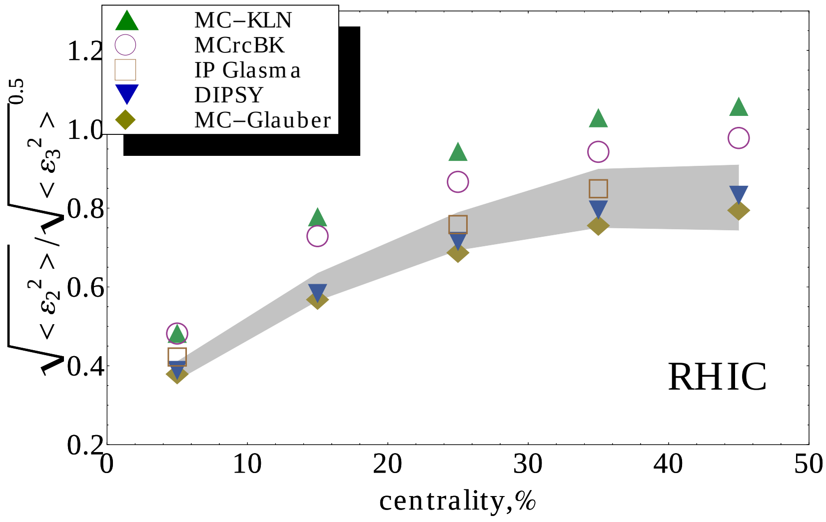

Figure 4.7: (Color online) Ratio of eccentricity moments $\sqrt{\langle\varepsilon_2^2\rangle}/\left(\sqrt{\langle\varepsilon_3^2\rangle}\right)^k$ versus centrality. Shaded bands are allowed by experiment values, combined with hydrodynamic calculations, for RHIC. Symbols are predictions from various models of initial state.

For all the models the centrality bins are set using the total entropy of each Monte Carlo event which is close to the total multiplicity, obtained in hydro evolution. As it was mentioned before, experimental definitions of centrality are also using multiplicity, so the uncertainties in centrality definition are negligible and are not taken into account.

The results for the values of $\mathcal{C}$ calculated in different Monte Carlo models are shown in the Tables 4.1 and 4.2 and the corresponding figures 4.7, 4.8. We put constraints on the initial state models by comparing the values of Monte Carlo models with the $\mathcal{C}$ minimal and maximum values. Thus, one can see that MC-KLN is excluded for all centralities both at RHIC and LHC. It is in agreement with recent studies which have shown that this model underpredicts the values of triangular flow v_3 at RHIC, while the elliptical flow v_2 is well reproduced [74, 160]. The MC Glauber model (which we basically use with a superposition weight of number of participants and number of binary collisions), does not show agreement with data at LHC, except for the most central region, while it shows a good agreement for RHIC. The MC-rcBK model is excluded at RHIC and is inside allowed band for several centralities at the LHC. DIPSY and IP-Glasma models shows good results for both RHIC and LHC, and so does the MC Glauber models when binary collision scaling is chosen.

Since MC-Glauber model has as a free parameter, the value of the source size σ, we demonstrate how the source smearing effect can change the predicted values with the variation of σ. In fig. 4.6 we display as an example the 20-30% centrality range. The MC-Glauber model (superposition weight) is shown for different values of the width of gaussian σ=0 fm, 0.4 fm, 0.8 fm and 1.2 fm [151] which are denoted by different symbol sizes. By changing this parameter, the result is shifted along the band which has the same effect as changing the viscosity, so that the agreement with data cannot be improved by adjusting the unknown source size. Thus, the ratios in Table 4.1 and Table 4.2, only change respectively by 2% and 1%. This can be understood as following: only the denominator in the (4.4), (4.6) is affected by the smearing of the sources [187] while the numerator remains unchanged. Thus, the effect of source smearing is a small increase in the system size which results in smaller ε_n. Since $\{r^3\} \propto \{r^2\}^{2/3}$, the value of ε_n is decreasing so that

$$\varepsilon_2/\varepsilon_3^{2/3} \sim const\,. \tag{4.11}$$

Since the value of k in equation (4.10) is close to 2/3, the smearing process moves the results parallel to the allowed band due to (4.11).

In fig. 4.9 one can see the predictions of the MC models of initial state with the shaded bands of the allowed region for all the centrality range. All models

Table 4.2: Values of the ratio $\sqrt{\langle\varepsilon_2^2\rangle}/\sqrt{\langle\varepsilon_3^2\rangle}^{0.6}$ at LHC.

% centrality	0-5	5-10	10-20	20-30	30-40
minimum	0.40	0.58	0.76	0.88	0.94
maximum	0.43	0.65	0.87	1.06	1.13
MC-Glauber	0.39	0.50	0.66	0.78	0.85
MC-Glauber (N_{coll})	0.46	0.61	0.79	0.92	0.96
MC-Glauber (N_{part})	0.33	0.42	0.57	0.71	0.80
MC-KLN	0.46	0.73	0.98	1.17	1.25
MC-rcBK	0.48	0.67	0.88	1.04	1.12
IP-Glasma	0.43	-	0.83	0.97	1.03
DIPSY	0.40	0.58	0.76	0.90	0.95

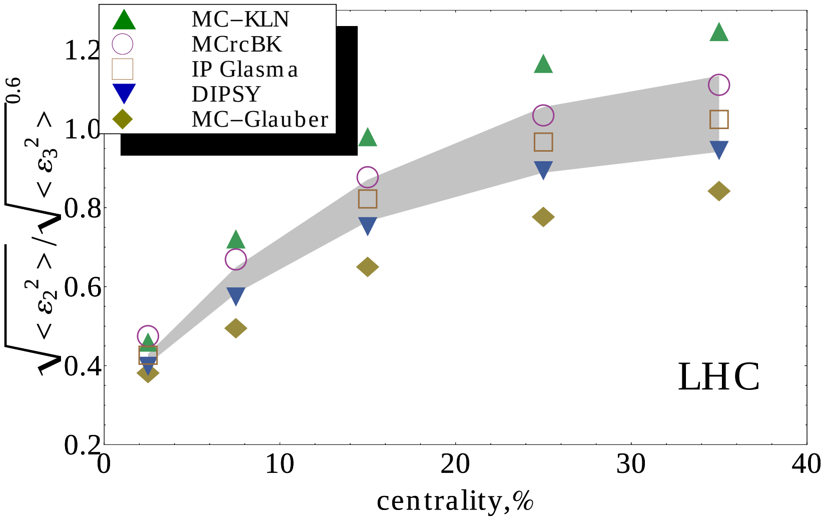

Figure 4.8: (Color online) Ratio of eccentricity moments $\sqrt{\langle\varepsilon_2^2\rangle}/\left(\sqrt{\langle\varepsilon_3^2\rangle}\right)^k$ versus centrality. Shaded bands are allowed by experiment values, combined with hydrodynamic calculations, for LHC. Symbols are predictions from various models of initial state.

show that the rms ε_2 and rms ε_3 increase with centrality, as it was expected from the explanation given in the first section. The difference between LHC energies and RHIC energies depends on the model. Thus, the MC Glauber model shows a decrease of ε_2 and ε_3 by several % which could be explained by the fact that lead nuclei used at LHC are bigger system than gold nuclei used at RHIC, though this explanation is not complete. For the MC-rcBK model the values are quite similar for both experiments. For the DIPSY model the ε_2 is increased, while ε_3 stays the same.

The claim that some model is compatible with data or can be excluded seems

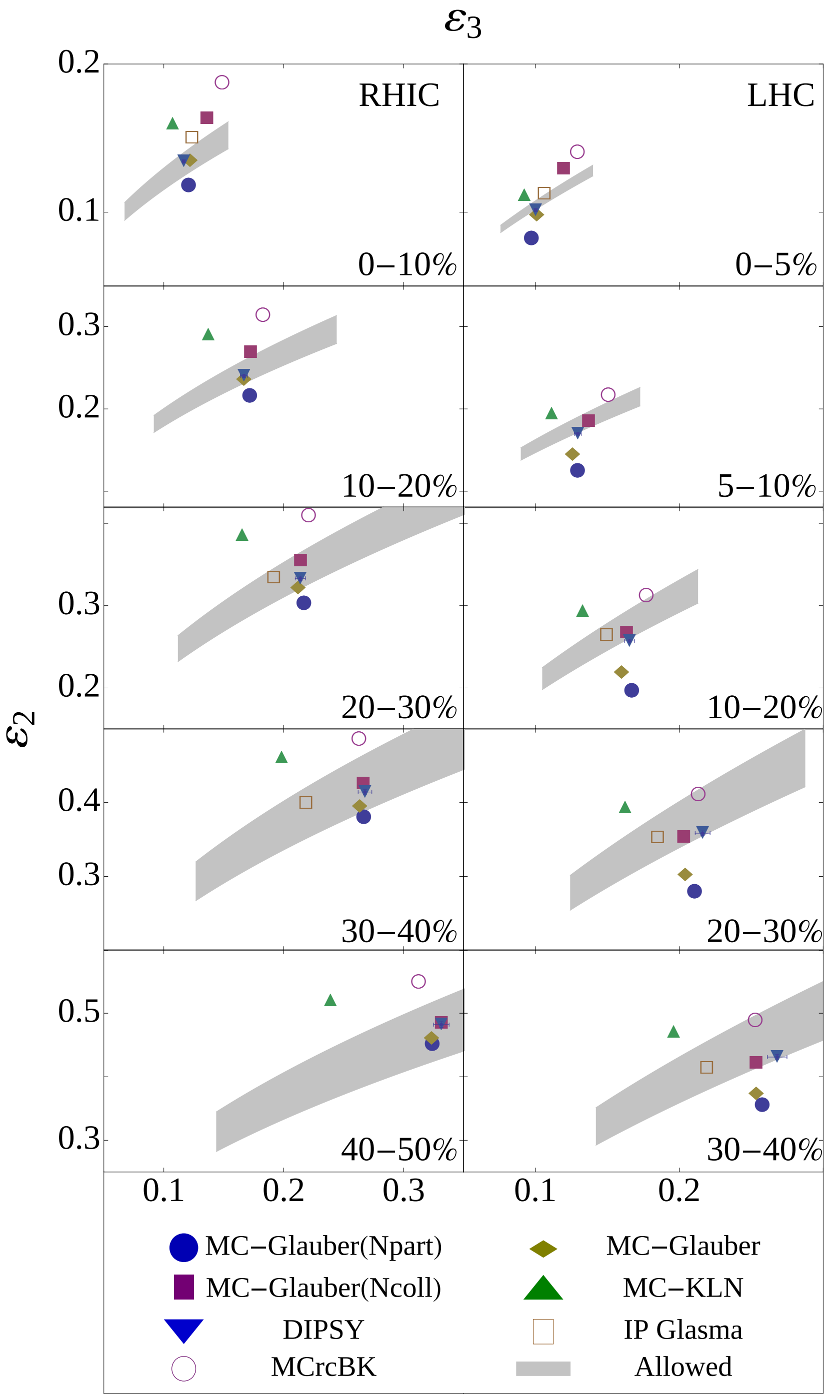

Figure 4.9: (Color online) Shaded bands are root-mean-square values of $(\varepsilon_2, \varepsilon_3)$ allowed by experimental data in combination with hydrodynamic calculations, for Au-Au collisions at $\sqrt{s_{NN}} = 0.2$ TeV (left)and Pb-Pb collisions at $\sqrt{s_{NN}} = 2.76$ TeV (right)in various centrality windows (from top to bottom). Symbols are predictions from various models of initial conditions (see text for details).

to be strong with respect to several uncertainties in the definitions of ε_2 and ε_3.

Chapter 5

Event-plane correlations

The anisotropy of the particle distribution is characterized by the Fourier expansion

$$\frac{dN}{d\phi} \propto 1 + 2\sum_{n=1}^{\infty} v_n \cos n(\phi - \Phi_n)\,, \tag{5.1}$$

where ϕ is an azimuthal angle, v_n is a magnitude of the n'th flow harmonics and Φ_n is an event plane characterizing the phase of the n'th flow harmonic.

Anisotropic flow is usually measured in two-particle angular correlations [188, 14, 137, 16] as it was described in Chapter 1. A new study of the so called *event-plane correlations* among the event planes of different flow harmonics started recently [153, 10, 19, 189]. The event-plane correlations are defined by the functions

$$\langle \cos\left(c_1\Phi_1 + ... + lc_l\Phi_l\right)\rangle\,. \tag{5.2}$$

Since the azimuthal orientation cannot be controlled in the experiments and only rotationally symmetric quantities can be measured, the coefficients must add up as $c_1 + 2c_2 + ... + lc_l = 0$ [153].

In 2012, ATLAS presented measurements of event plane correlations in Pb-Pb collisions [19, 189] and significant correlations were observed for two-plane (e.g., the correlation between second Φ_2 and fourth harmonics Φ_4) and three-plane correlations (e.g., the correlation between second Φ_2, third Φ_3 and fifth Φ_5 harmonics). These correlations can be qualitatively explained within the hydrodynamic approach by the combination of flow response in the medium with initial state fluctuations. Thus, as we discussed earlier in Chapter 4, in hydrodynamics v_1, v_2 and v_3 with a good approximation have a linear response to the medium. However, higher flow harmonics have an additional non-linear response. Thus, v_4 has an additional non-linear contribution where magnitude scales as v_2^2, i.e. $v_4 \propto v_2^2$, and is oriented along Φ_2. This non-linear mixing results in the correlations between Φ_4 and Φ_2 event plane angles, denoted as $\langle \cos 4(\Phi_2 - \Phi_4) \rangle$. The coefficient v_5 also has an additional non-linear response which represents a mixing between v_2 and v_3 harmonics, i.e. $v_5 \propto v_2 v_3$. This non-linear response results in correlations between Φ_2, Φ_3 and Φ_5 planes, denoted $\langle \cos(2\Phi_2 + 3\Phi_3 - 5\Phi_5) \rangle$. These correlations are strong where v_2 is large, i.e. in more peripheral collisions as we can see in fig. 5.1. Note, that if the event planes Φ_n were correlated completely, the values of $\langle \cos 4(\Phi_2 - \Phi_4) \rangle$ and $\langle \cos(2\Phi_2 + 3\Phi_3 - 5\Phi_5) \rangle$ would be equal to 1.

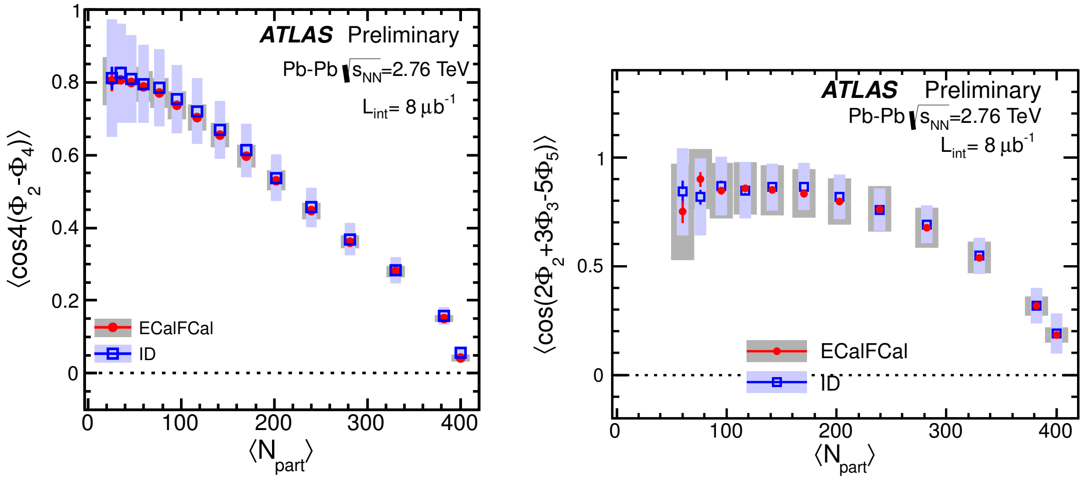

Figure 5.1: $\langle \cos 4(\Phi_2 - \Phi_4) \rangle$(left) and $\langle \cos(2\Phi_2 + 3\Phi_3 - 5\Phi_5) \rangle$(right) vs N_{part} from [19].

The measurements of event-plane correlations suggest that both the fluctuations in the initial state and the evolution of the medium in the final state are important for the formation of these correlations. There were several successful attempts to reproduce these correlations with different theoretical models [108, 20, 164]. In order to study the event-plane correlations we propose a theoretical approach based on a simple model of initial state fluctuations, called *independent source model*. For the modelisation of the hydrodynamic response we use the cumulant expansion formalism [145]. Our goal is to see what can be learnt from the hydrodynamic response from ATLAS data with minimal assumptions concerning the initial state.

In this Chapter we present such analysis for the correlations $\langle \cos 4(\Phi_2 - \Phi_4) \rangle$ and $\langle \cos(2\Phi_2 + 3\Phi_3 - 5\Phi_5) \rangle$. The experimental data for the calculations and the notations in this section are taken from ref. [19].

All data and conclusions presented in this Chapter are preliminary.

5.1 Event-plane correlations measurements

In order to perform the analysis of chosen correlations, it is important to understand how the event-plane correlations are measured in the experiment.

The ATLAS collaboration was measuring [19] the angular correlations between the harmonics Φ_n. The method they used is the *event plane* (EP) method. It was shown [190] that the traditional event-plane method [191] does not measure the mean value. In fact, in EP method, the measured value is lying between the event-average mean value $\langle v_n \rangle$ and the root-mean-square value $\left\langle v_n^2 \right\rangle^{1/2}$ [190, 192] and depends on the reaction plane resolution. The measurements of mixed-harmonic correlations have even stronger influence from this effect [193]. Thus this affects the measured correlation between the event planes Φ_4 and Φ_2

$$c\{2,2,-4\} = \langle \cos 4\left(\Phi_4 - \Phi_2\right)\rangle \ . \tag{5.3}$$

This correlation cannot be measured directly if v_2 and v_4 fluctuate. However it is possible to measure

$$c\{2,2,-4\} = \frac{\left\langle v_4 v_2^2 \cos 4(\Phi_4 - \Phi_2)\right\rangle}{\sqrt{\left\langle v_2^2\right\rangle^2 \left\langle v_4^2\right\rangle}} \ . \tag{5.4}$$

Note, that if there are no fluctuations of v_2 and v_4, (5.4) is equivalent to (5.3).

The values, measured[1] by the ATLAS collaboration with the EP method [19] are between the values obtained with (5.3) and (5.4). Recently the ATLAS collaboration published [189] new measurements with the *scalar-product* (SP) method [191, 194, 193, 20] which corresponds to the value given by (5.4) but we do not consider them here[2].

The measured value of 3-particle correlation denoted by ATLAS as $\langle \cos\left(2\Phi_2 + 3\Phi_3 - 5\Phi_5\right)\rangle$:

$$c\{2,3,-5\} = \frac{\left\langle v_2 v_3 v_5 \cos\left(2\Phi_2 + 3\Phi_3 - 5\Phi_5\right)\right\rangle}{\sqrt{\left\langle v_2^2\right\rangle \left\langle v_3^2\right\rangle \left\langle v_5^2\right\rangle}} \ . \tag{5.5}$$

This representation was suggested in the refs. [153, 193] and is more suitable for our analysis.

---

[1] Note, that ATLAS collaboration papers [19, 189] and the theoretical works [164, 20] have different notations. Thus, ATLAS define Φ_n as the event-plane angle, and theoreticians define it as Ψ_n. In order to avoid misunderstanding we denote the measured correlations between n_k harmonics as $c\{n_1, n_2 ...\}$.

[2] Our analysis was done before the new data were published, so this analysis needs to be updated in the future with the new data sets, though we can notice that for the chosen correlations the data does not change significantly.

5.2 Our model

In order to describe anisotropic flow v_n response to the medium in hydrodynamics we denote the complex flow coefficient as[3]

$$V_n = v_n e^{in\Psi_n} , \tag{5.6}$$

where Ψ_n is an event-plane angle.

As it was described in Chapter 4, the hydrodynamic response for first three flow harmonics is linear with a good approximation. We recall that this reads

$$V_1 = a_1 E_1 , \tag{5.7}$$
$$V_2 = a_2 E_2 , \tag{5.8}$$
$$V_3 = a_3 E_3 , \tag{5.9}$$

where a_n are linear hydrodynamic response to the initial state, and E_n is the complex coefficient depending on the initial density profile, which will be defined below. In this section we consider higher flow harmonics v_4 and v_5. These harmonics have additional non-linear response to the medium [163]. Thus, in analogy with the hydrodynamic response of the lower flow harmonics, it can be written

$$V_4 = a_4 E_4 + b_4 E_2^2 , \tag{5.10}$$
$$V_5 = a_5 E_5 + b_5 E_2 E_3 . \tag{5.11}$$

There are two terms which relate V_4 and V_5 to the initial profile: linear one and non-linear one. The coefficients a_n is indicating the linear hydrodynamic response to the medium and b_n is a non-linear hydrodynamic response. The values E_n are characterizing the medium properties defined by the initial conditions. Thus, we need two models: hydrodynamic response model and a model of initial state. In this section we discuss the hydrodynamic response model and the initial state model is presented in the section 5.4.

Following refs. [60, 164], we assume that the hydrodynamic response is represented in terms of *cumulants*[4] $\mathcal{E}_n$, where its complex notation with the corresponding orientation Φ_n reads as

$$E_n = \mathcal{E}_n e^{in\Phi_n} . \tag{5.12}$$

---

[3] From here we follow the notations and definitions used in theoretical works, in particular in ref. [164].

[4] In order to distinguish moments from cumulants the moments are denoted as ε_n and cumulants are denoted as $\mathcal{E}_n$.

The general definition of the cumulants is

$$\mathcal{E}_n e^{in\Phi_n} \equiv -\frac{\{r^n e^{in\phi}\} - \delta_n}{\{r^n\}}\,, \tag{5.13}$$

where δ_n denotes the subtractions. The values $\delta_n = 0$ turns cumulant representation to the moment representation which was used in Chapters 2, 3, 4.

For first three harmonics azimuthal cumulants and moments are identical as defined in Chapter 4. eqs. (4.2), (4.4), (4.6) [164], but 4th and 5th harmonics have additional non-linear response to the medium:

$$\mathcal{E}_4 e^{i4\Phi_4} \equiv -\frac{\left[\{r^4 e^{i4\phi}\} - 3\{r^2 e^{i2\phi}\}^2\right]}{\{r^4\}}\,, \tag{5.14}$$

$$\mathcal{E}_5 e^{i5\Phi_5} \equiv -\frac{\left[\{r^5 e^{i5\phi}\} - 10\{r^2 e^{i2\phi}\}\{r^3 e^{i3\phi}\}\right]}{\{r^5\}}\,. \tag{5.15}$$

The cumulants $\mathcal{E}_1$, $\mathcal{E}_2$, $\mathcal{E}_3$, $\mathcal{E}_4$ and $\mathcal{E}_5$ characterize the deformation of energy density profile in the transverse plane, respectively: dipole, elliptic, triangular, quadrangular and pentagonal.

The definitions presented earlier were given for one single event. In the following calculations we will need to calculate the mixed terms of the cumulants averaged over all the events. We will use following notations [153, 187]

$$\mathcal{E}\{n_1, ..., n_k\} \equiv \langle E_{n_1} E_{n_2} ... E_{n_k} \rangle, \tag{5.16}$$

where $\langle ... \rangle$ denotes an average over events in a centrality class. The rms average of $\mathcal{E}_n$ [89]:

$$\mathcal{E}_n\{2\} \equiv \langle \mathcal{E}_n^2 \rangle^{1/2} = \mathcal{E}\{n, -n\}^{1/2}. \tag{5.17}$$

The symmetry with respect to the reaction plane ($y \to -y$) means that all the cumulants are real, i.e. $\mathcal{E}\{-n_1, ..., -n_k\} = \mathcal{E}\{n_1, ..., n_k\}$. The symmetry $(x, y) \to (-x, -y)$ means that the odd values of $n_1 + ... + n_k$ are vanishing. The azimuthal orientation of each collision in not measured experimentally, so the only possible measurements are symmetric to the rotation values. Thus, the only cumulants taken into account must satisfy the following rule:

$$n_1 + ... + n_k = 0\,. \tag{5.18}$$

5.3 Event-averaged observables

The event-plane correlations averaged over events which we study in this Chapter are $\langle\cos 4(\Phi_4-\Phi_2)\rangle$ and $\langle\cos(2\Phi_2+3\Phi_3-5\Phi_5)\rangle$.

Using the notations of the previous section, the measured value for $\langle\cos 4(\Phi_4-\Phi_2)\rangle$ (5.4) reads

$$c\{2,2,-4\} = \frac{\langle V_4^* V_2 V_2\rangle}{\sqrt{\langle|V_2^2|\rangle^2\langle V_4^2\rangle}}\,. \tag{5.19}$$

Applying the eqs. (5.8)-(5.11), the previous equation can be written as

$$c\{2,2,-4\} = \frac{\left\langle(a_4E_4^*+b_4E_2^2)a_2E_2a_2E_2\right\rangle}{\sqrt{\langle(a_2E_2)^2\rangle^2\langle(a_4E_4^*+b_4E_2^2)^2\rangle}}\,. \tag{5.20}$$

We introduce the following variables:

$$\lambda_{224} = \left(\frac{b_4}{a_4}\right)\frac{\sqrt{\langle E_2^2E_2^{*2}\rangle}}{\sqrt{\langle E_4E_4^*\rangle}}\,, \tag{5.21}$$

$$\mathcal{C}_{224} = \frac{\left\langle E_4^*E_2^2\right\rangle}{\sqrt{\langle E_4E_4^*\rangle\langle E_2^2E_2^{*2}\rangle}}\,, \tag{5.22}$$

where a_4 and b_4 are linear and non-linear response coefficients from the eq. (5.33). The variable λ_{224} represents the ratio of the non-linear response over the linear response to the medium. The coefficient $\mathcal{C}_{224}$ is the Pearson correlation between E_4 and E_2^2 which is small. In these terms the desired correlation has a form:

$$c\{2,2,-4\} = \frac{\lambda_{224}+\mathcal{C}_{224}}{\sqrt{1+2\lambda_{224}\mathcal{C}_{224}+\lambda_{224}^2}} \simeq \frac{\lambda_{224}}{\sqrt{1+\lambda_{224}^2}}, \tag{5.23}$$

where we have neglected the correlation $\mathcal{C}_{224}$.

In the similar way a 3-event plane correlation $c\{2,3,-5\}$ can be presented as

$$c\{2,3,-5\} = \frac{\langle V_2V_3V_5^*\rangle}{\sqrt{\langle V_2^2\rangle\langle V_3^2\rangle\langle V_5^2\rangle}}\,, \tag{5.24}$$

where using eqs. (5.8)-(5.11), we have

$$c\{2,3,-5\} = \frac{\langle a_2E_2a_3E_3(a_5E_5^*+b_5E_2E_3)\rangle}{\sqrt{\langle(a_2E_2)^2\rangle\langle(a_3E_3)^2\rangle\langle(a_5E_5^*+b_5E_2E_3)^2\rangle}}\,, \tag{5.25}$$

In analogy with (5.21) we denote the following parameters:

$$\lambda_{235} = \left(\frac{b_5}{a_5}\right) \frac{\sqrt{\langle E_2 E_3 E_2^* E_3^* \rangle}}{\sqrt{\langle E_5 E_5^* \rangle}} \,, \tag{5.26}$$

$$\mathcal{C}_{235} = \frac{\langle E_5^* E_2 E_3 \rangle}{\sqrt{\langle E_5 E_5^* \rangle \langle E_2 E_2^* \rangle \langle E_3 E_3^* \rangle}} \,. \tag{5.27}$$

Thus, (5.24) reads

$$c\{2, 3, -5\} = \frac{\lambda_{235} + C_{235}}{\sqrt{1 + 2C_{235}\lambda_{235} + \lambda_{235}^2}} \simeq \frac{\lambda_{235}}{\sqrt{1 + \lambda_{235}^2}} \,. \tag{5.28}$$

In order to perform the calculations of desired correlations first we need to calculate the following terms: $\langle E_2 E_2^* \rangle \equiv \mathcal{E}\{2, -2\}$, $\langle E_4 E_4^* \rangle \equiv \mathcal{E}\{4, -4\}$, $\left\langle E_4^* E_2^2 \right\rangle \equiv \mathcal{E}\{2, 2, -4\}$, $\left\langle E_2^2 E_2^{*2} \right\rangle \equiv \mathcal{E}\{2, 2, -2 -2\}$, $\langle E_2 E_3 E_2^* E_3^* \rangle \equiv \mathcal{E}\{2, 3, -2, -3\}$, $\langle E_5 E_5^* \rangle \equiv \mathcal{E}\{5, -5\}$, $\langle E_5^* E_2 E_3 \rangle \equiv \mathcal{E}\{2, 3, -5\}$ and $\langle E_3 E_3^* \rangle \equiv \mathcal{E}\{3, -3\}$. In order to calculate these correlations we need a model of the initial state that we present in the next section.

Secondly, we need to know the constants of the hydrodynamic response b_4/a_4 and b_5/a_5. The calculations of the hydrodynamic response coefficients will be presented in sections 5.5 and 5.6.

5.4 Independent source model

As the model of the initial state in our work we choose the *independent source model*. Here we introduce the formalism of this model [187].

In this model authors assume that initial energy density profile in the transverse plane is the superposition of N random independent sources

$$\epsilon(\mathbf{x}) = \sum_{j=1}^{N} \rho(|\mathbf{x} - \mathbf{x}_j|), \tag{5.29}$$

where $\mathbf{x}_j$ are N independent random variables with a probability distribution $p(\mathbf{x}_j)$ and $\rho(r)$ - profile of a single source, where the standard choice for $\rho(r)$ is a Gaussian profile

$$\rho(r) = \rho_0 e^{-\frac{r^2}{\sigma^2}}, \tag{5.30}$$

where σ is controlling the width.

All cumulants can be calculated analytically as a systematic expansion in powers of $1/N$ within the independent-source model formalism.

5.4.1 Application of the model

In this section we introduce the analytic tools that are needed in order to calculate cumulants $\mathcal{E}\{n_1, ..., n_k\}$ within the independent source model [187].

We denote $\langle f(x,y)\rangle$ the average value of $f(x,y)$ with the source probability density $p(\mathbf{x}_j)$ and introduce

$$\delta_f \equiv \{f\} - \langle f\rangle \tag{5.31}$$

for the event-by-event fluctuations, and $\{...\}$ denotes an average over the transverse plane in a single event

$$\{f(x,y)\} \equiv \frac{\int f(x,y)\epsilon(x,y)dxdy}{\int \epsilon(x,y)dxdy}\,, \tag{5.32}$$

where the average is weighted with the energy density $\epsilon(x,y)$.

We use complex coordinates $z = x + iy$ and $\bar{z} = x - iy$. The $re^{i\phi}$ is replaced by $z - \delta_z$ in order to take into account the recentering correction. Thus the expressions for cumulants are obtained in the leading order on fluctuations as

$$E_1 = -\frac{\{(z-\delta_z)^2(\bar{z}-\delta_{\bar{z}})\}}{\{r^3\}} \simeq -\frac{\delta_{z^2\bar{z}} - 2\left\langle z\bar{z}\right\rangle \delta_z - \left\langle z^2\right\rangle \delta_{\bar{z}}}{\left\langle r^3\right\rangle}\,, \tag{5.33}$$

$$E_2 = -\frac{\left\langle z^2\right\rangle + \delta_{z^2} - \delta_z^2}{\left\langle z\bar{z}\right\rangle + \delta_{z\bar{z}} - \delta_z\delta_{\bar{z}}}\,, \tag{5.34}$$

$$E_3 = -\frac{\delta_{z^3} - 3\left\langle z^2\right\rangle \delta_z - 3\delta_{z^2}\delta_z}{\left\langle r^3\right\rangle}\,, \tag{5.35}$$

$$E_4 = -\frac{\left\langle z^4\right\rangle + \delta_{z^4} - 3\left\langle z^2\right\rangle^2 - 6\left\langle z^2\right\rangle \delta_{z^2} - 3\delta_{z^2}^2 + 12\left\langle z^2\right\rangle \delta_z^2 - 4\delta_{z^3}\delta_z}{\left\langle z^2\bar{z}^2\right\rangle + \delta_{z^2\bar{z}^2} - 2\delta_{z^2\bar{z}}\delta_{\bar{z}} + \left\langle z^2\right\rangle \delta_{\bar{z}}^2 - 2\delta_{z\bar{z}^2\delta_z} + 4\left\langle z\bar{z}\right\rangle \delta_z\delta_{\bar{z}} + \left\langle \bar{z}^2\right\rangle \delta_{\bar{z}}^2}\,, \tag{5.36}$$

$$E_5 = -\frac{\delta_{z^5} - 5\left\langle z^4\right\rangle \delta_z - 10\left\langle z^2\right\rangle \delta_{z^3} + 30\left\langle z^2\right\rangle^2 \delta_z - 5\delta_{z^4}\delta_z - 6\left\langle z^2\right\rangle \delta_{z^2}\delta_z + \delta_{z^2}\delta_{z^3}}{\left\langle r^5\right\rangle}\,. \tag{5.37}$$

The calculations of $\mathcal{E}\{n_1, ..., n_k\}$ involve an average over events of products of δ's. Two-point averages are computed within the formalism of the independent source model as following:

$$\langle \delta_f \delta_g \rangle = \frac{\langle fg \rangle - \langle f \rangle \langle g \rangle}{N} \,. \tag{5.38}$$

We use the following equations

$$\langle z^n \bar{z}^m \rangle = 0, \text{ n-m} - \text{odd} \,, \tag{5.39}$$

$$\langle z^n \bar{z}^m \rangle = \left\langle r^{n+m} \cos\left((n-m)\phi\right) \right\rangle, \text{ n-m} - \text{even} \,. \tag{5.40}$$

With the equations (5.33)-(5.40) we are able now to get any cumulants $\mathcal{E}\{n_1, ..., n_k\}$. In the following sections we use the notation

$$\varepsilon_s \equiv -\frac{\langle r^2 \cos 2\phi \rangle}{\langle r^2 \rangle}, \tag{5.41}$$

which denotes the *standard eccentricity*.

5.5 Correlation $c\{2, 2, -4\}$

In this section we present the calculations of the value event-plane correlation $c\{2, 2, -4\}$ in the terms of the independent source model.

In order to calculate $\mathcal{E}\{2, -2\}$ we repeat the calculation as in [187]. We apply the formulas (5.33), (5.38) and (5.40) and get the following equation:

$$\mathcal{E}\{2, -2\} = \varepsilon_s^2 + \frac{\left\langle r^4 \right\rangle + 3\varepsilon_s^2 \left\langle r^4 \right\rangle + 4\varepsilon_s \left\langle r^4 \cos 2\phi \right\rangle}{\left\langle r^2 \right\rangle^2 N} \,. \tag{5.42}$$

In the similar way it can be obtained

$$\mathcal{E}\{2, 2, -2, -2\} = \frac{\varepsilon_s^2 (2(2 + 5\varepsilon_s^2) \left\langle r^4 \right\rangle + 16\varepsilon_s \left\langle r^4 \cos 2\phi \right\rangle + 2 \left\langle r^4 \cos 4\phi \right\rangle + \varepsilon_s^2 \left\langle r^2 \right\rangle^2 N)}{\left\langle r^2 \right\rangle^2 N} \,. \tag{5.43}$$

The expressions for the correlations $\mathcal{E}\{4, -4\}$, $\mathcal{E}\{4, -2, -2\}$ are too large, so we present their general form in the Appendix. Knowing the four correlations $\mathcal{E}\{2, -2\}$, $\mathcal{E}\{2, 2, -2, -2\}$, $\mathcal{E}\{4, -4\}$ and $\mathcal{E}\{4, -2, -2\}$ one can obtain the expressions for λ_{224} and $\mathcal{C}_{224}$ which are also presented in the Appendix.

The average values $\langle r^{n+m} \cos (n-m)\phi \rangle$ presented in the terms of the expressions for λ_{224} and $\mathcal{C}_{224}$ are calculated in the Gaussian model, PHOBOS Monte Carlo Glauber model and MC-KLN model.

5.5.1 Correlations for c{2,2,-4} in the Gaussian model

In this section we present the calculations of correlations $\mathcal{E}\{n_1, n_2, ...n_k\}$ with the Gaussian model.

For the Gaussian model the density distribution is

$$\rho(x,y) = \frac{1}{2\pi\sigma_x\sigma_y} e^{-\frac{x^2}{2\sigma_x^2}-\frac{y^2}{2\sigma_y^2}} \tag{5.44}$$

from where

$$\langle r^2 \rangle = \sigma_x^2 + \sigma_y^2 \,, \tag{5.45}$$

and the eccentricity reads as

$$\varepsilon_s = \frac{\sigma_x^2 - \sigma_y^2}{\sigma_x^2 + \sigma_y^2} \,. \tag{5.46}$$

Integration over $\rho(x,y)$ gives following expressions for the correlations:

$$\mathcal{E}\{2,-2\} = \frac{2 + 3\varepsilon_s^4 + \varepsilon_s^2(-5+N)}{N} \,, \tag{5.47}$$

$$\mathcal{E}\{4,-4\} = \frac{24}{(2+\varepsilon_s^2)^2 N} \,, \tag{5.48}$$

$$\mathcal{E}\{4,-2,-2\} = \frac{6\varepsilon_s^4(6+\varepsilon_s^2)}{(2+\varepsilon_s^2)^2 N} \,, \tag{5.49}$$

$$\mathcal{E}\{2,2,-2,-2\} = \frac{\varepsilon_s^2(8 + 10\varepsilon_s^4 + \varepsilon_s^2(-18+N))}{N} \,. \tag{5.50}$$

Thus, the expression for λ_{224} reads

$$\lambda_{224} = \frac{\sqrt{\frac{{\varepsilon_s}^2(8+10{\varepsilon_s}^4+{\varepsilon_s}^2(-18+N))}{N}}}{2\sqrt{6}\sqrt{\frac{1}{(2+{\varepsilon_s}^2)^2 N}}} \,. \tag{5.51}$$

And the expression for $\mathcal{C}_{224}$ is following:

$$\mathcal{C}_{224} = \frac{\sqrt{\frac{3}{2}}\varepsilon_s^4\left(6+\varepsilon_s^2\right)}{\left(2+\varepsilon_s^2\right)^2\sqrt{\frac{\varepsilon_s^2(8+10\varepsilon_s^4+\varepsilon_s^2(-18+N))}{\left(2+\varepsilon_s^2\right)^2 N^2}}N} \,. \tag{5.52}$$

Note, that Gaussian model is given only for the demonstration and we do not use this model in our following calculations. In order to calculate

$\langle r^{n+m}\cos{(n-m)\phi}\rangle$ we use PHOBOS MC-Glauber and MC-KLN models of initial state in the following sections.

5.5.2 Calculations of a_4/b_4 parameter with MC-Glauber and MC-KLN models

After we have got the values of the correlations defined in the section 5.3, we need to calculate the parameter a_4/b_4. For this goal we combine experimental data on measured correlations with the calculations of these correlations from independent source model which were in previous sections.

In this method the experimental data on $c\{2,2,-4\}(N_{part})$ can be fit with the function (5.23) and use the a_4/b_4 as a parameter.

We represent the fit function in the following way

$$\frac{(b_4/a_4)L_{224}}{\sqrt{1+(b_4/a_4)^2L_{224}^2}}(N_{part}) \tag{5.53}$$

or in general case

$$\frac{(b_4/a_4)L_{224}+\mathcal{C}_{224}}{\sqrt{1+(b_4/a_4)^2L_{224}^2+2(b_4/a_4)L_{224}\mathcal{C}_{224}}}(N_{part})\,, \tag{5.54}$$

where

$$L_{224}=\frac{\lambda_{224}}{(b_4/a_4)}=\frac{\sqrt{\langle E_2^2E_2^{*2}\rangle}}{\sqrt{\langle E_4E_4^*\rangle}}\,. \tag{5.55}$$

The behavior of the hydrodynamic response coefficients a_4 and b_4 can be expressed as a function of the size of the system $R\equiv\sqrt{\langle r^2\rangle}$. Thus, from the eq. (1.40) the hydrodynamic response coefficients decreases as $\propto 1/R$ [195] due to the viscous correction. This viscous correction is found to be more important for the linear response a_4. Thus, the ratio of nonlinear to linear response can be written in the following way:

$$(b_4/a_4)=\frac{\beta_4}{\left(1-\frac{\alpha_4}{\sqrt{\langle r^2\rangle}}\right)}\,. \tag{5.56}$$

In the eqs. (5.53) and (5.54) the parameters (b_4/a_4), L_{224} and $\mathcal{C}_{224}$ are in fact functions of N_{part}. In order to make a fit of the experimental data with one of the functions (5.53) or (5.54), one needs to find a form for the functions $L_{224}(N_{part})$ and $\mathcal{C}_{224}(N_{part})$. We do this by the fit of the numerical points got

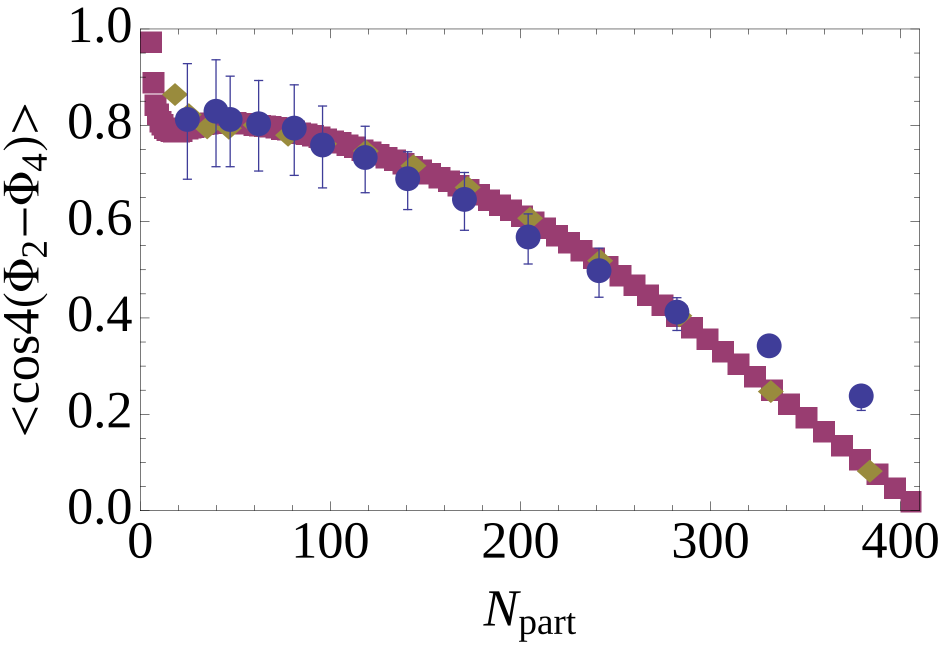

Figure 5.2: Comparison of experimental data of $c\{2,2,-4\}$ (blue circles) with the fit made with MC-Glauber (yellow diamonds) and MC-KLN models (purple squares) with the help of independent source model calculations.

from MC-Glauber or MC-KLN models with the polynomial functions. The value $\sqrt{\langle r^2\rangle}$ in (5.56) is also dependent on N_{part} and is fitted as well with a polynomial function. These functions then can be used in the fit models (5.53) or (5.54). The fit functions have only two parameters α_4 and β_4. The resulting fit is shown in fig. 5.2.

The parameters α_4 and β_4 extracted from the fit allow us to construct the function for the $a_4/b_4(N_{part})$. The resulting values are shown in fig. 5.3. In this figure we can see that the values of a_4/b_4 are different for MC-Glauber and MC-KLN models. These models give different prediction for $\langle E_2^2 E_2^{*2}\rangle$, thus the MC-KLN gives higher values, so the value of a_4/b_4 is also higher.

The extracted values of a_4/b_4 for the CGC model are of the same order of magnitude as the values obtained from the hydrodynamic calculations by Teaney and Yan [196].

5.6 Correlations for $c\{2,3,-5\}$ in the Gaussian model

In this section we present similar calculations for the measure 3-event plane correlation $c\{2,3,-5\}$.

The general formulas calculated within the independent source model formalism are presented in the Appendix.

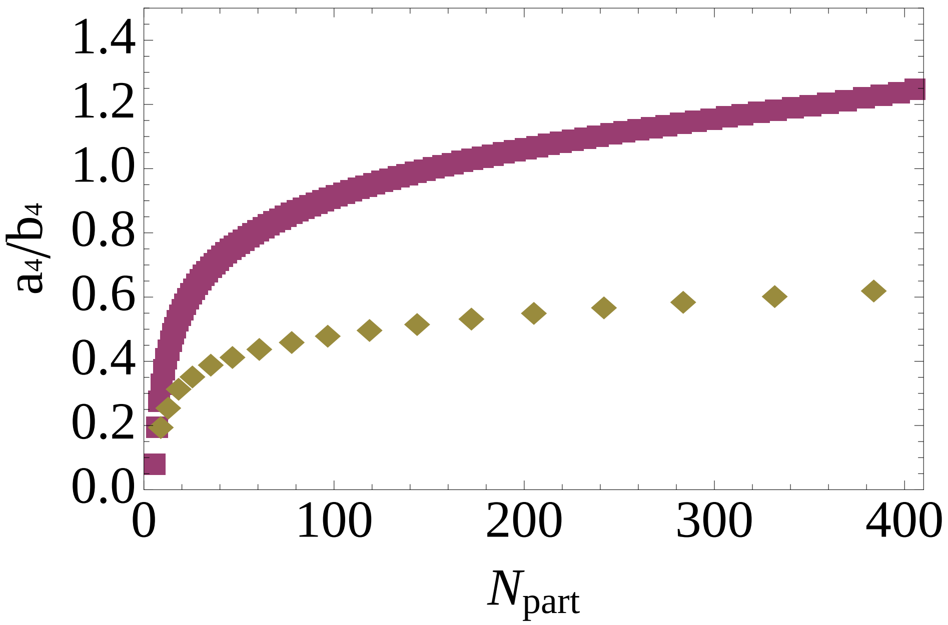

Figure 5.3: a_4/b_4 extracted from the fit, for MC Glauber (yellow diamonds) and MC-KLN models (purple squares).

Here we present the expressions for cumulants in the Gaussian model. The expressions which we get within this model demonstrate the usefulness of the cumulant formalism, thus one gets $\mathcal{E}\{2,3,-5\}=0$.

$$\mathcal{E}\{5,-5\} = \frac{(120\langle r^2\rangle^5)}{\langle r^5\rangle^2 N}\,, \tag{5.57}$$

$$\mathcal{E}\{3,-3\} = \frac{(6\langle r^2\rangle^3)}{\langle r^3\rangle^2 N}\,, \tag{5.58}$$

$$\mathcal{E}\{2,3,-2,-3\} = \frac{(6\varepsilon_s^2\langle r^2\rangle^3)}{\langle r^3\rangle^2 N}\,, \tag{5.59}$$

$$\mathcal{E}\{2,3,-5\} = 0\,, \tag{5.60}$$

$$\lambda_{235} = \frac{\sqrt{\frac{\varepsilon_s^2\langle r^2\rangle^3}{\langle r^3\rangle^2 N}}}{2\sqrt{5}\sqrt{\frac{\langle r^2\rangle^5}{\langle r^5\rangle^2 N}}}\,, \tag{5.61}$$

$$\mathcal{C}_{235} = 0\,. \tag{5.62}$$

where ε_s and $\langle r^2\rangle$ are defined by eqs. (5.45) and (5.46).

In the following sections these values are calculated within PHOBOS MC-

Glauber model.

5.6.1 Calculation of a_5/b_5 parameter with MC-Glauber model

In this section we do the same fit procedure as for a_4/b_4 parameter. Thus, we

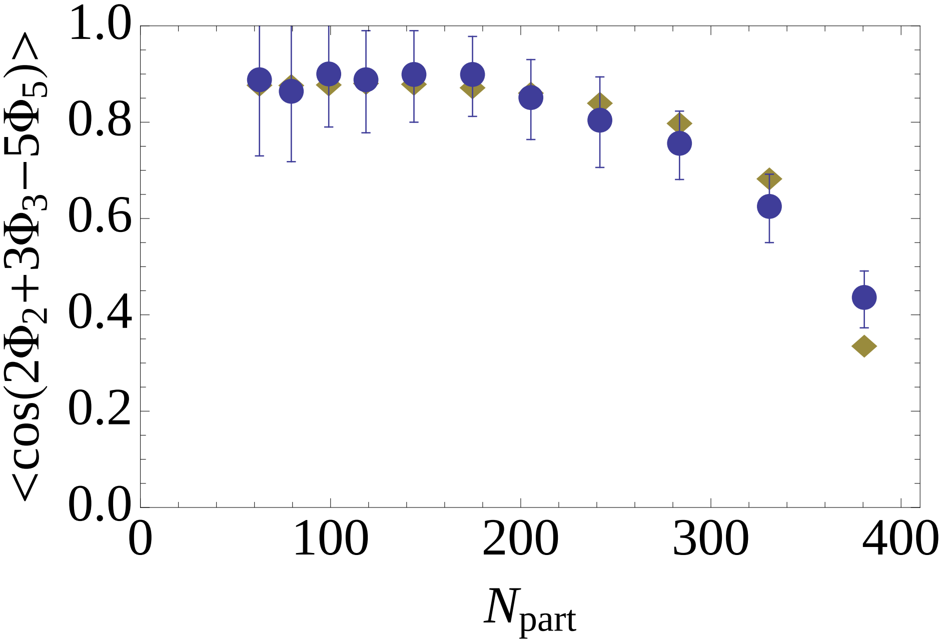

Figure 5.4: Comparison of experimental data of $c\{2, 3, -5\}$ (blue circles) with the fit made with MC-Glauber (yellow diamonds) with the help of independent source model calculations.

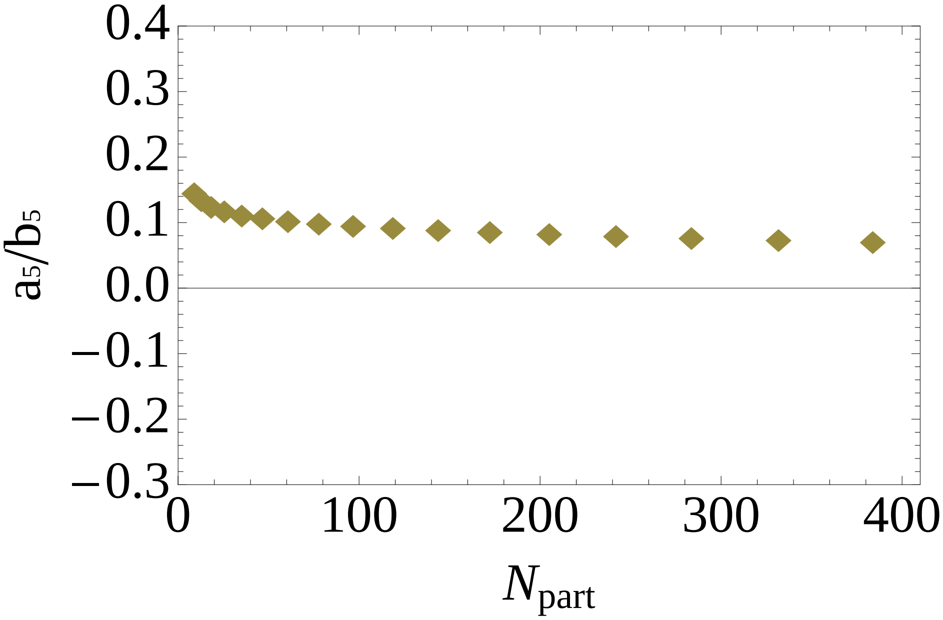

Figure 5.5: a_5/b_5 extracted from the fit with MC-Glauber model.

choose the fit function in the following way:

$$\frac{(b_5/a_5)L_{235}}{\sqrt{1+(b_5/a_5)^2L_{235}^2}}(N_{part})\,, \tag{5.63}$$

or in general case

$$\frac{(b_5/a_5)L_{235}+\mathcal{C}_{235}}{\sqrt{1+(b_5/a_5)^2L_{235}^2+2(b_5/a_5)L_{235}\mathcal{C}_{235}}}(N_{part})\,, \tag{5.64}$$

where we denote

$$L_{235}=\frac{\lambda_{235}}{(b_5/a_5)}=\frac{\sqrt{\langle E_2E_3E_2^*E_3^*\rangle}}{\sqrt{\langle E_5E_5^*\rangle}}\,. \tag{5.65}$$

The resulting fit is shown in fig. 5.4.

As in the case with a_4 and b_4, we assume the following dependence on the size of the system for the coefficients a_5 and b_5:

$$(b_5/a_5)=\frac{\beta_5}{\left(1-\frac{\alpha_5}{\sqrt{\langle r^2\rangle}}\right)}\,. \tag{5.66}$$

The extracted function of $a_5/b_5(N_{part})$ is presented in fig. 5.5. These values are in a good agreement with the hydrodynamic predictions by Teaney and Yan [196].

5.6.2 Verification of the independent source model.

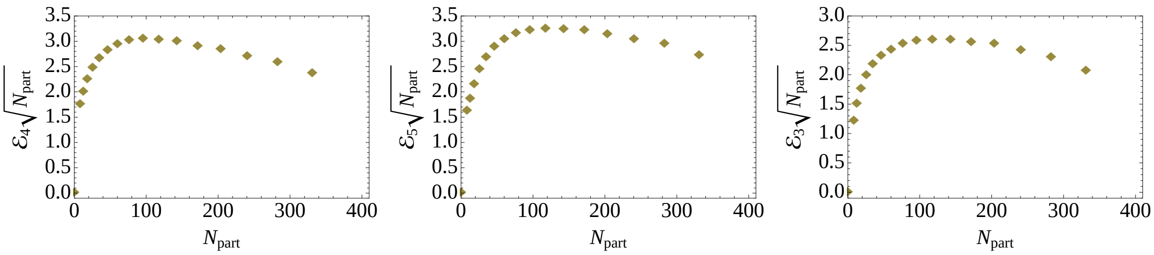

Figure 5.6: $\mathcal{E}_4\sqrt{N_{part}}(N_{part})$, $\mathcal{E}_5\sqrt{N_{part}}(N_{part})$ and $\mathcal{E}_3\sqrt{N_{part}}(N_{part})$ with MC-Glauber model

One of the main statements of the independent source model is that all the cumulants are $\propto \frac{1}{\sqrt{N_{part}}}$. In order to check this statement we compute $\mathcal{E}_4\sqrt{N_{part}}(N_{part})$, $\mathcal{E}_5\sqrt{N_{part}}(N_{part})$ and $\mathcal{E}_3\sqrt{N_{part}}(N_{part})$. In this calculations we used PHOBOS MC-Glauber model as the initial state model for the cumulants. The resulting functions are presented in figs. 5.6.

We expect these values to be close to a constant. In these figures we see that these values are approximately constant in the low centrality range, so the independent source model is considered reliable.

5.7 Predictions for the 4-particle correlation $c\{2,-3,-4,5\}$.

In this section we propose a prediction for the possible future measurement of 4-particle correlation $c\{2,-3,-4,5\} = \langle\cos(2\Phi_2 - 3\Phi_3 - 4\Phi_4 + 5\Phi_5)\rangle$.

We assume that

$$c\{2,-3,-4,5\} = \frac{c\{2,2,-4\}c\{2,3,-5\}\sqrt{\langle E_2\rangle^4}}{\langle E_2^2\rangle}\,. \tag{5.67}$$

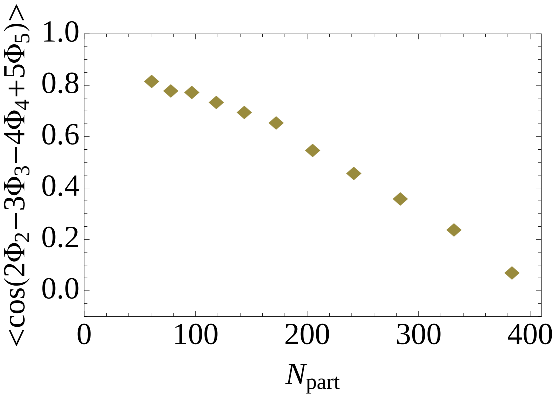

Figure 5.7: Prediction of $\langle\cos(2\Phi_2 - 3\Phi_3 - 4\Phi_4 + 5\Phi_5)\rangle$ with MC-Glauber model.

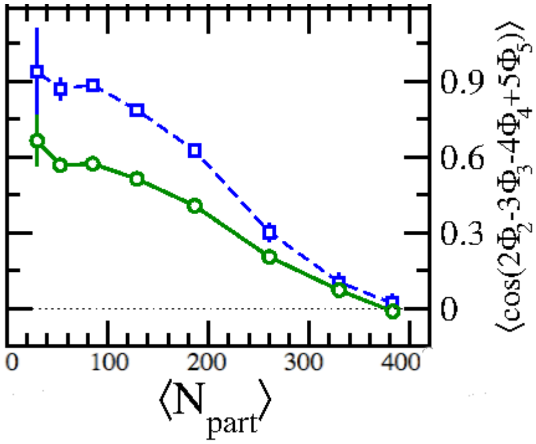

Figure 5.8: Prediction of $\langle\cos(2\Phi_2 - 3\Phi_3 - 4\Phi_4 + 5\Phi_5)\rangle$ (N_{part}) from the AMPT model, from [20] (blue squares: calculations made with SP method, green circles: calculations made with EP method)

Here $c\{2,2,-4\}$ and $c\{2,3,-5\}$ are 2-particle and 3-particle correlations measured by ATLAS and the values of $\sqrt{\langle E_2\rangle^4}$ and $\left\langle E_2^2\right\rangle$ can be calculated within some model of initial state. As the model of initial state here we choose PHOBOS MC-Glauber model. The resulting prediction is shown in fig. 5.7.

These predictions are consistent with the predictions made within AMPT model [20] with the SP method, see fig. 5.8.

Conclusions

In this thesis we were studying the physics of anisotropic flow in heavy-ion collisions. Anisotropic flow characterizes the collective expansion as the response to the fluctuating initial state. A relativistic hydrodynamics is used in order to describe the evolution of the fluid created in the heavy-ion collision. During its evolution the fluid turns into independently emitted outgoing particles. The azimuthal distribution of produced particles is characterized by a Fourier distribution with the flow coefficients v_n

$$\frac{dN}{d\phi} = \frac{N}{2\pi}\left(1 + 2\sum_{n=1}^{\infty} v_n \cos n(\phi - \Psi_n)\right) , \tag{6.68}$$

where Ψ_n are the reference angles of harmonics n.

In the **first chapter** of this thesis we gave a general introduction which includes a historical review on the heavy-ion physics and recent theoretical and experimental approaches.

In the **second chapter** we present the first measurements of the Fourier coefficient v_1, called directed flow. For this goal we used the data on two-particle correlations $V_{n\Delta}$ from ALICE collaboration. These correlations can be represented as the product of two single-particle flow coefficients

$$V_{n\Delta} = v_n^a v_n^b , \tag{6.69}$$

where a and b are two particles. It turns out that for the case $n = 1$ this factorization does not work and one needs to take into account an additional term due to the momentum conservation. Thus the two-particle correlation reads

$$V_{1\Delta} = v_1^a v_1^b - k p_t^a p_t^b , \tag{6.70}$$

where k is the momentum conservation coefficient.

In order to extract v_1 we fit the experimental data $V_{1\Delta}$ which represent a $N \times N$ matrix by the right side of the equation (6.70) with N+1 parameters: N parameters v_1 and one parameter k, where N is the number of p_t bins. The values of v_1 extracted as the parameter of the fit, thus were the first measurements of rapidity-even directed flow at the LHC. Later these results were confirmed by the ATLAS collaboration.

In the **third chapter** we present the first viscous hydrodynamic calculations of the directed flow v_1. For this goal we use 2+1D viscous hydrodynamic model with the optical Glauber model for the initial state. As far as the initial profile of the optical Glauber model is symmetric and smooth it had to be deformed in order to create the dipole asymmetry which causes the directed flow. With the viscous hydrodynamic calculations we have found that v_1 has a weaker dependence on viscosity than v_2 and v_3. In this chapter we also present the predictions of the directed flow at RHIC. These results were later confirmed by the measurements at RHIC.

In the **fourth chapter** we focus on the initial state models. The initial conditions are poorly constrained, so there is a number of models of initial state. We propose two ways to constrain the models of initial state by using anisotropic flow data. In the first part of this chapter we constrain the models of initial state by using v_1 flow data. Directed flow v_1 is found with a good approximation to be proportional to the initial dipole symmetry ε_1. The following equation can be written:

$$v_1^{LHC} = \left(\frac{v_1}{\varepsilon_1}\right)_h \varepsilon_1^{tune} . \tag{6.71}$$

In order to fit the left part of the equation which represents experimental data extracted in Chapter 2, with the right part of the equation, one can tune the value ε_1^{tune}. $\left(\frac{v_1}{\varepsilon_1}\right)_h$ are the values calculated from hydrodynamics as shown in Chapter 3. By tuning the coefficient ε_1^{tune} one can fit the experimental values at low p_t and at high p_t. The corresponding values of ε_1^{tune} are considered as upper and lower bounds on the actual values of ε_1. Calculating the values of ε_1 with different Monte Carlo models of initial state one can compare them with the allowed region and thus exclude or constrain these models. The fact that v_1 is weakly dependent on viscosity allows us to put a constrain on some models of initial state, because the created band is rather narrow. However, the constraints provided by this method are not strong enough. In the second part of the chapter we propose more strong constraints on the models of initial state by using v_2 and v_3 data. In this method we perform a combined analysis of v_2 and v_3 using viscous hydrodynamics. Elliptic and triangular flow are proportional to the elliptic and triangular asymmetry respectively, which reads as $v_n = \kappa\varepsilon_n$, $n = 2, 3$, where κ is the linear response in harmonic n. Combining experimental values with hydrodynamic calculations we extract the values ε_2 and ε_3 in the following way

$$\sqrt{\langle \varepsilon_n^2 \rangle} \equiv \frac{\sqrt{\langle (v_n)^2 \rangle}}{\kappa_n}\,, \tag{6.72}$$

where $\langle (v_n)^2 \rangle$ is the measured rms value of integrated flow, average is taken over collision events. The coefficient $\kappa_n = (v_n/\varepsilon_n)_{hydro}$ is calculated in hydrodynamics. This way we are able to extract the rms values of ε_n. By varying free parameters in the hydrodynamic calculations, we have obtained range of ε_2 and ε_3 values. These values placed in the (rms ε_2, rms ε_3) plane create a band of allowed values. After calculating the values of rms ε_2 and rms ε_3 in the models of initial state, we put them on the (rms ε_2, rms ε_3) plane and constrain models of initial state. This method could be used as a test by any group which has a Monte Carlo model.

The **fifth chapter**, prospects for initial state studies were given. In this chapter, we perform calculations of event-plane correlations recently measured by the ATLAS collaboration. In order to study these correlations one needs a model for the initial state and a model for the hydrodynamic response. In our study we used the independent source model proposed by Ollitrault, Luzum and Bhalerao and the cumulant approach proposed by Teaney and Yan. In the cumulant approach the medium response is represented as a sum of linear and non-linear order responses. We analyze two correlations, $c\{2, 2-4\} = \langle \cos 4(\Phi_2 - \Phi_4) \rangle$ and $c\{2, 3, -5\} = \langle \cos(2\Phi_2 + 3\Phi_3 - 5\Phi_5) \rangle$. The method provides the ratio of linear over non-linear response. The values are in agreement with the predictions from hydrodynamics. In this chapter we also propose a simple method for a prediction of the possible future measurement of the 4-particle correlation $c\{2, -3, -4, 5\} = \langle \cos(2\Phi_2 - 3\Phi_3 - 4\Phi_4 + 5\Phi_5) \rangle$, the predicted values are similar to the predictions made with the AMPT model.

In this thesis, we have performed a full analysis of the first five harmonics v_n, $n < 6$. This analysis allowed us to put constraints on the initial state models. The future of the studies of the initial state is connected with the analysis of event-plane correlations. We hope that these studies could shed light on initial fluctuations and the hydrodynamic expansion.

Appendices

Cumulants calculations

Cumulants for $c\{2,2,-4\}$ correlation

Here we present the general formulas for cumulants, calculated within the cumulan expantion formalism and within the independent source model. The values presented here and used in the Chapter 5. Later they are calculated within Gauss, MC-Glauber and MC-KLN models.

The following expressions are calculated with the formulas for cumulants within the independent source model formalism:

$$\mathcal{E}_1 e^{i\Phi_1} = E_1 = -\frac{\{(z-\delta_z)^2(\bar{z}-\delta_{\bar{z}})\}}{\{r^3\}} \simeq -\frac{\delta_{z^2\bar{z}} - 2\left\langle z\bar{z}\right\rangle \delta_z - \left\langle z^2\right\rangle \delta_{\bar{z}}}{\left\langle r^3\right\rangle}, \tag{A.73}$$

$$\mathcal{E}_2 e^{2i\Phi_2} = E_2 = -\frac{\left\langle z^2\right\rangle + \delta_{z^2} - \delta_z^2}{\left\langle z\bar{z}\right\rangle + \delta_{z\bar{z}} - \delta_z\delta_{\bar{z}}}, \tag{A.74}$$

$$\mathcal{E}_3 e^{3i\Phi_3} = E_3 = -\frac{\delta_{z^3} - 3\left\langle z^2\right\rangle \delta_z - 3\delta_{z^2}\delta_z}{\left\langle r^3\right\rangle}, \tag{A.75}$$

$$\mathcal{E}_4 e^{4i\Phi_4} = E_4 = -\frac{\left\langle z^4\right\rangle + \delta_{z^4} - 3\left\langle z^2\right\rangle^2 - 6\left\langle z^2\right\rangle \delta_{z^2} - 3\delta_{z^2}^2 + 12\left\langle z^2\right\rangle \delta_z^2 - 4\delta_{z^3}\delta_z}{\left\langle z^2\bar{z}^2\right\rangle + \delta_{z^2\bar{z}^2} - 2\delta_{z^2\bar{z}}\delta_{\bar{z}} + \left\langle z^2\right\rangle \delta_{\bar{z}}^2 - 2\delta_{z\bar{z}^2\delta_z} + 4\left\langle z\bar{z}\right\rangle \delta_z\delta_{\bar{z}} + \left\langle \bar{z}^2\right\rangle \delta_{\bar{z}}^2}, \tag{A.76}$$

$$\mathcal{E}_5 e^{5i\Phi_5} = E_5 = -\frac{\delta_{z^5} - 5\left\langle z^4\right\rangle \delta_z - 10\left\langle z^2\right\rangle \delta_{z^3} + 30\left\langle z^2\right\rangle^2 \delta_z - 5\delta_{z^4}\delta_z - 6\left\langle z^2\right\rangle \delta_{z^2}\delta_z + \delta_{z^2}\delta_{z^3}}{\left\langle r^5\right\rangle}, \tag{A.77}$$

where

$$\delta_f \equiv \{f\} - \langle f\rangle \tag{A.78}$$

for the event-by-event fluctuations, and $\{...\}$ denotes an average over the transverse plane in a single event:

$$\{f(x,y)\} \equiv \frac{\int f(x,y)\epsilon(x,y)dxdy}{\int \epsilon(x,y)dxdy}. \tag{A.79}$$

We use complex coordinates $z = x + iy$ and $\bar{z} = x - iy$. We replace $re^{i\phi}$ by $z - \delta z$ in order to take into account the recentering correction.

Two-point averages are computed as following:

$$\langle \delta_f \delta_g \rangle = \frac{\langle fg \rangle - \langle f \rangle \langle g \rangle}{N} \tag{A.80}$$

We use the following equations:

$$\langle z^n \bar{z}^m \rangle = 0, n - m - odd \tag{A.81}$$

$$\langle z^n \bar{z}^m \rangle = \left\langle r^{n+m} \cos\left((n-m)\phi\right) \right\rangle, n - m - even, \tag{A.82}$$

Thus, we get following equations

$$\mathcal{E}\{2,-2\} = \varepsilon_s^2 + \frac{\left\langle r^4 \right\rangle + 3\varepsilon_s^2 \left\langle r^4 \right\rangle + 4\varepsilon_s \left\langle r^4 \cos 2\phi \right\rangle}{\left\langle r^2 \right\rangle^2 N} \tag{A.83}$$

$$\mathcal{E}\{2,2,-2,-2\} = \frac{\varepsilon_s^2 (2(2+5\varepsilon_s^2) \left\langle r^4 \right\rangle + 16\varepsilon_s \left\langle r^4 \cos 2\phi \right\rangle + 2 \left\langle r^4 \cos 4\phi \right\rangle + \varepsilon_s^2 \left\langle r^2 \right\rangle^2 N)}{\left\langle r^2 \right\rangle^2 N} \tag{A.84}$$

$$\begin{aligned}
\mathcal{E}\{4,-4\} = \frac{1}{\left\langle r^4 \right\rangle^4 N} (-36\varepsilon_s^6 \left\langle r^2 \right\rangle^6 \left\langle r^4 \right\rangle - 6 \left\langle r^4 \right\rangle^2 \left\langle r^4 \cos 4\phi \right\rangle^2 - \\
8 \left\langle r^2 \right\rangle^2 \left\langle r^4 \right\rangle \left(-3\varepsilon_s^2 \left\langle r^2 \right\rangle^2 + \left\langle r^4 \cos 4\phi \right\rangle \right)^2 + 72\varepsilon_s^3 \left\langle r^2 \right\rangle^3 \left\langle r^4 \right\rangle \left\langle r^6 \cos 2\phi \right\rangle + \\
12\varepsilon_s \left\langle r^2 \right\rangle \left\langle r^4 \right\rangle (\left\langle r^4 \right\rangle - 2 \left\langle r^4 \cos 4\phi \right\rangle) \left\langle r^6 \cos 2\phi \right\rangle + \\
\left\langle r^4 \right\rangle^2 \left\langle r^8 \right\rangle + 3 \left\langle r^4 \cos 4\phi \right\rangle^2 \left\langle r^8 \right\rangle + \\
\varepsilon_s^4 \left\langle r^2 \right\rangle^4 \left(-9 \left\langle r^4 \right\rangle^2 + 24 \left\langle r^4 \right\rangle \left\langle r^4 \cos 4\phi \right\rangle + 27 \left\langle r^8 \right\rangle \right) - \\
4 \left\langle r4 \right\rangle \left\langle r^4 \cos 4\phi \right\rangle \left\langle r^8 \cos 4\phi \right\rangle + \\
2\varepsilon_s^2 \left\langle r^2 \right\rangle^2 (18 \left\langle r^4 \right\rangle^3 + 9 \left\langle r^4 \right\rangle^2 \left\langle r^4 \cos 4\phi \right\rangle - 2 \left\langle r^4 \right\rangle \left\langle r^4 \cos 4\phi \right\rangle^2 - \\
9 \left\langle r^4 \cos 4\phi \right\rangle \left\langle r^8 \right\rangle + 6 \left\langle r^4 \right\rangle \left\langle r^8 \cos 4\phi \right\rangle) + \\
\left\langle r^4 \right\rangle^2 \left(-3\varepsilon_s^2 \left\langle r^2 \right\rangle^2 + \left\langle r^4 \cos 4\phi \right\rangle \right)^2 N)
\end{aligned} \tag{A.85}$$

$$\begin{aligned}\mathcal{E}\{2,2,-4\} = \frac{1}{\left\langle r^2\right\rangle^2 \left\langle r^4\right\rangle^3 N}(&-6\varepsilon_s^6 \left\langle r^2\right\rangle^6 \left\langle r^4\right\rangle - \left\langle r^4\right\rangle^2 \left\langle r^4 \cos 4\phi^2\right\rangle + \\ &12\varepsilon_s^3 \left\langle r^2\right\rangle^2 \left\langle r^4\right\rangle \left(2 \left\langle r^4\right\rangle \left\langle r^4 \cos 2\phi\right\rangle + \left\langle r^2\right\rangle \left\langle r^6 \cos 2\phi\right\rangle\right) - \\ &2\varepsilon_s \left\langle r^4\right\rangle (2 \left\langle r^4\right\rangle \left\langle r^4 \cos 2\phi\right\rangle \left\langle r^4 \cos 4\phi\right\rangle - \left\langle r^2\right\rangle \left\langle r^4\right\rangle \left\langle r^6 \cos 2\phi\right\rangle + \\ &\left\langle r^2\right\rangle \left\langle r^4 \cos 4\phi\right\rangle \left\langle r^6 \cos 2\phi\right\rangle) + \\ &\varepsilon_s^2 (4 \left\langle r^2\right\rangle^4 \left\langle r^4\right\rangle \left\langle r^4 \cos 4\phi\right\rangle - 3 \left\langle r^4\right\rangle^3 \left\langle r^4 \cos 4\phi\right\rangle + \\ &2 \left\langle r^2\right\rangle \left\langle r^4\right\rangle (- \left\langle r^4 \cos 4\phi\right\rangle \left\langle r^6\right\rangle + \left\langle r^4\right\rangle \left\langle r^6 \cos 4\phi\right\rangle) + \\ &\left\langle r^2\right\rangle^2 (12 \left\langle r^4\right\rangle^3 - \left\langle r^4 \cos 4\phi\right\rangle \left\langle r^8\right\rangle + \left\langle r^4\right\rangle \left\langle r^8 \cos 4\phi\right\rangle - \\ &\left\langle r^4\right\rangle^2 \left\langle r^4 \cos 4\phi\right\rangle (-6 + N))) + \\ &\varepsilon_s^4 \left\langle r^2\right\rangle^2 (-12 \left\langle r^2\right\rangle^4 \left\langle r^4\right\rangle + 9 \left\langle r^4\right\rangle^3 + 6 \left\langle r^2\right\rangle \left\langle r^4\right\rangle \left\langle r^6\right\rangle + \\ &\left\langle r^2\right\rangle^2 (2 \left\langle r^4\right\rangle \left\langle r^4 \cos 4\phi\right\rangle + 3 \left\langle r^8\right\rangle + 3 \left\langle r^4\right\rangle^2 N))) \end{aligned} \tag{A.86}$$

Denoting λ_{224} and $\mathcal{C}_{224}$ in the following way

$$\lambda_{224} = \left(\frac{b_4}{a_4}\right) \frac{\sqrt{\langle E_2^2 E_2^{*2}\rangle}}{\sqrt{\langle E_4 E_4^*\rangle}}, \tag{A.87}$$

$$\mathcal{C}_{224} = \frac{\left\langle E_4^* E_2^2\right\rangle}{\sqrt{\langle E_4 E_4^*\rangle \langle E_2^2 E_2^{*2}\rangle}}, \tag{A.88}$$

one gets the value of λ_{224}:

$$\begin{aligned}
\lambda_{224} = \left(\frac{b_4}{a_4}\right)(\sqrt{(}(\varepsilon_s^2(2(2+5\varepsilon_s^2)\left\langle r^4\right\rangle + 16\varepsilon_s\left\langle r^4\cos 2\phi\right\rangle + 2\left\langle r^4\cos 4\phi\right\rangle + \\
\varepsilon_s^2\left\langle r^2\right\rangle^2 N))/(\left\langle r^2\right\rangle^2 N)))/(\sqrt{(}1/(\left\langle r^4\right\rangle^4 N)(-36\varepsilon_s^6\left\langle r^2\right\rangle^6\left\langle r^4\right\rangle - \\
8\left\langle r^2\right\rangle^2\left\langle r^4\right\rangle\left\langle r^4\cos 4\phi\right\rangle^2 - 6\left\langle r^4\right\rangle^2\left\langle r^4\cos 4\phi\right\rangle^2 + \\
72\varepsilon_s^3\left\langle r^2\right\rangle^3\left\langle r^4\right\rangle\left\langle r^6\cos 2\phi\right\rangle + \\
12\varepsilon_s\left\langle r^2\right\rangle\left\langle r^4\right\rangle(\left\langle r^4\right\rangle - 2\left\langle r^4\cos 4\phi\right\rangle)\left\langle r^6\cos 2\phi\right\rangle + \left\langle r^4\right\rangle^2\left\langle r^8\right\rangle + \\
3\left\langle r^4\cos 4\phi\right\rangle^2\left\langle r^8\right\rangle - 4\left\langle r^4\right\rangle\left\langle r^4\cos 4\phi\right\rangle\left\langle r^8\cos 4\phi\right\rangle + \\
2\varepsilon_s^2\left\langle r^2\right\rangle^2(18\left\langle r^4\right\rangle^3 - 9\left\langle r^4\cos 4\phi\right\rangle\left\langle r^8\right\rangle + \\
\left\langle r^4\right\rangle(24\left\langle r^2\right\rangle^2\left\langle r^4\cos 4\phi\right\rangle - 2\left\langle r^4\cos 4\phi\right\rangle^2 + 6\left\langle r^8\cos 4\phi\right\rangle) - \\
3\left\langle r^4\right\rangle^2\left\langle r^4\cos 4\phi\right\rangle(-3+N)) + \\
3\varepsilon_s^4\left\langle r^2\right\rangle^4(-24\left\langle r^2\right\rangle^2\left\langle r^4\right\rangle + 8\left\langle r^4\right\rangle\left\langle r^4\cos 4\phi\right\rangle + 9\left\langle r^8\right\rangle + \\
3\left\langle r^4\right\rangle^2(-1+N)) + \left\langle r^4\right\rangle^2\left\langle r^4\cos 4\phi\right\rangle^2 N)))
\end{aligned} \tag{A.89}$$

and the value of $\mathcal{C}_{224}$

$$\begin{aligned}
\mathcal{C}_{224} = (-6\varepsilon_s^6 \left\langle r^2 \right\rangle^6 \left\langle r^4 \right\rangle - \left\langle r^4 \right\rangle^2 \left\langle r^4 \cos 4\phi \right\rangle^2 + \\
12\varepsilon_s^3 \left\langle r^2 \right\rangle^2 \left\langle r^4 \right\rangle (2 \left\langle r^4 \right\rangle \left\langle r^4 \cos 2\phi \right\rangle + \left\langle r^2 \right\rangle \left\langle r^6 \cos 2\phi \right\rangle) - \\
2\varepsilon_s \left\langle r^4 \right\rangle (2 \left\langle r^4 \right\rangle \left\langle r^4 \cos 2\phi \right\rangle \left\langle r^4 \cos 4\phi \right\rangle - \left\langle r^2 \right\rangle \left\langle r^4 \right\rangle \left\langle r^6 \cos 2\phi \right\rangle + \\
\left\langle r^2 \right\rangle \left\langle r^4 \cos 4\phi \right\rangle \left\langle r^6 \cos 2\phi \right\rangle) + \\
\varepsilon_s^2 (4 \left\langle r^2 \right\rangle^4 \left\langle r^4 \right\rangle \left\langle r^4 \cos 4\phi \right\rangle - 3 \left\langle r^4 \right\rangle^3 \left\langle r^4 \cos 4\phi \right\rangle + \\
2 \left\langle r^2 \right\rangle \left\langle r^4 \right\rangle (- \left\langle r^4 \cos 4\phi \right\rangle \left\langle r^6 \right\rangle + \left\langle r^4 \right\rangle \left\langle r^6 \cos 4\phi \right\rangle) + \\
\left\langle r^2 \right\rangle^2 (12 \left\langle r^4 \right\rangle^3 - \left\langle r^4 \cos 4\phi \right\rangle \left\langle r^8 \right\rangle + \left\langle r^4 \right\rangle \left\langle r^8 \cos 4\phi \right\rangle - \\
\left\langle r^4 \right\rangle^2 \left\langle r^4 \cos 4\phi \right\rangle (-6 + N))) + \\
\varepsilon_s^4 \left\langle r^2 \right\rangle^2 (-12 \left\langle r^2 \right\rangle^4 \left\langle r^4 \right\rangle + 9 \left\langle r^4 \right\rangle^3 + 6 \left\langle r^2 \right\rangle \left\langle r^4 \right\rangle \left\langle r^6 \right\rangle + \\
\left\langle r^2 \right\rangle^2 (2 \left\langle r^4 \right\rangle \left\langle r^4 \cos 4\phi \right\rangle + 3 \left\langle r^8 \right\rangle + 3 \left\langle r^4 \right\rangle^2 N)))/ \\
((\left\langle r^2 \right\rangle^2 \left\langle r^4 \right\rangle^3 N \sqrt{(} - 1/((\left\langle r^2 \right\rangle^2 \left\langle r^4 \right\rangle^4 N^2) \varepsilon_s^2 (2(2 + 5\varepsilon_s^2) \left\langle r^4 \right\rangle + \\
16\varepsilon_s \left\langle r^4 \cos 2\phi \right\rangle + 2 \left\langle r^4 \cos 4\phi \right\rangle + \\
\varepsilon_s^2 \left\langle r^2 \right\rangle^2 N)(36\varepsilon_s^6 \left\langle r^2 \right\rangle^6 \left\langle r^4 \right\rangle + 8 \left\langle r^2 \right\rangle^2 \left\langle r^4 \right\rangle \left\langle r^4 \cos 4\phi^2 \right\rangle + \\
6 \left\langle r^4 \right\rangle^2 \left\langle r^4 \cos 4\phi \right\rangle^2 - 72\varepsilon_s^3 \left\langle r^2 \right\rangle^3 \left\langle r^4 \right\rangle \left\langle r^6 \cos 2\phi \right\rangle - \\
12\varepsilon_s \left\langle r^2 \right\rangle \left\langle r^4 \right\rangle (\left\langle r^4 \right\rangle - 2 \left\langle r^4 \cos 4\phi \right\rangle) \left\langle r^6 \cos 2\phi \right\rangle - \left\langle r^4 \right\rangle^2 \left\langle r^8 \right\rangle - \\
3 \left\langle r^4 \cos 4\phi \right\rangle^2 \left\langle r^8 \right\rangle + 4 \left\langle r^4 \right\rangle \left\langle r^4 \cos 4\phi \right\rangle \left\langle r^8 \cos 4\phi \right\rangle - \\
2\varepsilon_s^2 \left\langle r^2 \right\rangle^2 (18 \left\langle r^4 \right\rangle^3 - 9 \left\langle r^4 \cos 4\phi \right\rangle \left\langle r^8 \right\rangle + \\
\left\langle r^4 \right\rangle (24 \left\langle r^2 \right\rangle^2 \left\langle r^4 \cos 4\phi \right\rangle - 2 \left\langle r^4 \cos 4\phi \right\rangle^2 + 6 \left\langle r^8 \cos 4\phi \right\rangle) - \\
3 \left\langle r^4 \right\rangle^2 \left\langle r^4 \cos 4\phi \right\rangle (-3 + N)) + \\
3\varepsilon_s^4 \left\langle r^2 \right\rangle^4 (24 \left\langle r^2 \right\rangle^2 \left\langle r^4 \right\rangle - 8 \left\langle r^4 \right\rangle \left\langle r^4 \cos 4\phi \right\rangle - \\
9 \left\langle r^8 \right\rangle - 3 \left\langle r^4 \right\rangle^2 (-1 + N)) - \left\langle r^4 \right\rangle^2 \left\langle r^4 \cos 4\phi \right\rangle^2 N)))
\end{aligned} \tag{A.90}$$

Cumulants for $c\{2, 3, -5\}$ correlation

Here we perform the calculations of cumulants which we need in order to calculate $c\{2, 3, -5\}$ correlations.

$$\begin{aligned}\mathcal{E}\{2,3,-5\} = {} & \frac{(90\varepsilon_s^4 \left\langle r^2 \right\rangle^4)}{(\left\langle r^3 \right\rangle \left\langle r^5 \right\rangle N)} + \frac{(60\varepsilon_s^3 \left\langle r^2 \right\rangle^2 \left\langle r^2 \right\rangle^2 \left\langle r^4 \cos 2\phi \right\rangle)}{(\left\langle r^3 \right\rangle \left\langle r^5 \right\rangle N)} - \frac{(15\varepsilon_s^2 \left\langle r^2 \right\rangle^2 \left\langle r^4 \cos 4\phi \right\rangle)}{(\left\langle r^3 \right\rangle \left\langle r^5 \right\rangle N)} - \\ & \frac{(5\varepsilon_s \left\langle r^4 \cos 2\phi \right\rangle \left\langle r^4 \cos 4\phi \right\rangle)}{(\left\langle r^3 \right\rangle \left\langle r^5 \right\rangle N)} + \frac{(10\varepsilon_s^2 \left\langle r^2 \right\rangle \left\langle r^6 \right\rangle)}{(\left\langle r^3 \right\rangle \left\langle r^5 \right\rangle N)} + \frac{(3\varepsilon_s^2 \left\langle r^2 \right\rangle \left\langle r^6 \cos 4\phi \right\rangle)}{(\left\langle r^3 \right\rangle \left\langle r^5 \right\rangle N)} + \frac{(\varepsilon_s \left\langle r^8 \cos 2\phi \right\rangle)}{(\left\langle r^3 \right\rangle \left\langle r^5 \right\rangle N)}\end{aligned} \tag{A.91}$$

$$\begin{aligned}\mathcal{E}\{5,-5\} = {} & \frac{\left\langle r^{10} \right\rangle}{(\left\langle r^5 \right\rangle^2 N)} + \frac{(900\varepsilon_s^4 \left\langle r^2 \right\rangle^5)}{(\left\langle r^5 \right\rangle^2 N)} + \frac{(600\varepsilon_s^3 \left\langle r^2 \right\rangle^3 \left\langle r^4 \cos 2\phi \right\rangle)}{(\left\langle r^5 \right\rangle^2 N)} - \\ & \frac{(300\varepsilon_s^2 \left\langle r^2 \right\rangle^3 \left\langle r^4 \cos 4\phi \right\rangle}{(\left\langle r^5 \right\rangle^2 N)} - \frac{(100\varepsilon_s \left\langle r^2 \right\rangle \left\langle r^4 \cos 2\phi \right\rangle \left\langle r^4 \cos 4\phi \right\rangle)}{(\left\langle r^5 \right\rangle^2 N)} + \\ & \frac{(25 \left\langle r^2 \right\rangle \left\langle r^4 \cos 4\phi \right\rangle^2)}{(\left\langle r^5 \right\rangle^2 N)} + \frac{(100\varepsilon_s^2 \left\langle r^2 \right\rangle^2 \left\langle r^6 \right\rangle)}{(\left\langle r^5 \right\rangle^2 N)} + \frac{(60\varepsilon_s^2 \left\langle r^2 \right\rangle^2 \left\langle r^6 \cos 4\phi \right\rangle)}{(\left\langle r^5 \right\rangle^2 N)} - \\ & \frac{(10 \left\langle r^4 \cos 4\phi \right\rangle \left\langle r^6 \cos 4\phi \right\rangle)}{(\left\langle r^5 \right\rangle^2 N)} + \frac{(20\varepsilon_s \left\langle r^2 \right\rangle \left\langle r^8 \cos 2\phi \right\rangle)}{(\left\langle r^5 \right\rangle^2 N)}\end{aligned} \tag{A.92}$$

$$\varepsilon\{3,-3\} = \frac{(9\varepsilon_s^2 \left\langle r^2 \right\rangle^3 + 6\varepsilon_s \left\langle r^2 \right\rangle \left\langle r^4 \cos 2\phi \right\rangle + \left\langle r^6 \right\rangle)}{(\left\langle r^3 \right\rangle^2 N)} \tag{A.93}$$

$$\varepsilon\{2,3,-2,-3\} = \frac{\varepsilon_s^2(9\varepsilon_s^2 \left\langle r^2 \right\rangle^3 + 6\varepsilon_s \left\langle r^2 \right\rangle \left\langle r^4 \cos 4\phi \right\rangle + \left\langle r^6 \right\rangle)}{\left\langle r^3 \right\rangle^2 N} \tag{A.94}$$

We denote:

$$\lambda_{235} = \left(\frac{b_5}{a_5}\right) \frac{\sqrt{\langle E_2 E_3 E_2^* E_3^* \rangle}}{\sqrt{\langle E_5 E_5^* \rangle}}, \tag{A.95}$$

$$\mathcal{C}_{235} = \frac{\langle E_5^* E_2 E_3 \rangle}{\sqrt{\langle E_5 E_5^* \rangle \langle E_2 E_2^* \rangle \langle E_3 E_3^* \rangle}} \tag{A.96}$$

Thus, we have:

$$\begin{aligned}\lambda_{235} = \left(\frac{b_5}{a_5}\right) &\sqrt{(}(\varepsilon_s^2(9\varepsilon_s^2\left\langle r^2\right\rangle^3 + 6\varepsilon_s\left\langle r^2\right\rangle\left\langle r^4\cos 2\phi\right\rangle + \left\langle r^6\right\rangle))/ \\ &(\left\langle r^3\right\rangle^2 N)))/(\sqrt{1/((\langle r^5\rangle^2 N}((\left\langle r^{10}\right\rangle + \\ &5(180\varepsilon_s^4\left\langle r^2\right\rangle^5 + 120\varepsilon_s^3\left\langle r^2\right\rangle^3\left\langle r^4\cos 2\phi\right\rangle + \\ &\left\langle r^4\cos 4\phi\right\rangle(5\left\langle r^2\right\rangle\left\langle r^4\cos 4\phi\right\rangle - 2\left\langle r^6\cos 4\phi\right\rangle) + \\ &4\varepsilon_s^2\left\langle r^2\right\rangle^2(-15\left\langle r^2\right\rangle\left\langle r^4\cos 4\phi\right\rangle + 5\left\langle r^6\right\rangle + 3\left\langle r^6\cos 4\phi\right\rangle) + \\ &4\varepsilon_s\left\langle r^2\right\rangle(-5\left\langle r^4\cos 2\phi\right\rangle\left\langle r^4\cos 4\phi\right\rangle + \left\langle r^8\cos 2\phi\right\rangle))))) \end{aligned} \tag{A.97}$$

$$\begin{aligned}&\mathcal{C}_{235} = (\varepsilon_s(90\varepsilon_s^3\left\langle r^2\right\rangle^4 + 60\varepsilon_s^2\left\langle r^2\right\rangle^2\left\langle r^4\cos 2\phi\right\rangle - 5\left\langle r^4\cos 2\phi\right\rangle\left\langle r^4\cos 4\phi\right\rangle + \\ &\varepsilon_s\left\langle r^2\right\rangle(-15\left\langle r^2\right\rangle\left\langle r^4\cos 4\phi\right\rangle + 10\left\langle r^6\right\rangle + 3\left\langle r^6\cos 4\phi\right\rangle) + \\ &\left\langle r^8\cos 2\phi\right\rangle))/(\left\langle r^3\right\rangle\left\langle r^5\right\rangle\sqrt{(}1/(\left\langle r^3\right\rangle^2\left\langle r^5\right\rangle^2 N^2)\varepsilon_s^2(9\varepsilon_s^2\left\langle r^2\right\rangle^3 + 6\varepsilon_s\left\langle r^2\right\rangle\left\langle r^4\cos 2\phi\right\rangle + \\ &\left\langle r^6\right\rangle)(\left\langle r^{10}\right\rangle + 5(180\varepsilon_s^4\left\langle r^2\right\rangle^5 + 120\varepsilon_s^3\left\langle r^2\right\rangle^3\left\langle r^4\cos 2\phi\right\rangle + \left\langle r^4\cos 4\phi\right\rangle(5\left\langle r^2\right\rangle\left\langle r^4\cos 4\phi\right\rangle - \\ &2\left\langle r^6\cos 4\phi\right\rangle) + 4\varepsilon_s^2\left\langle r^2\right\rangle^2(-15\left\langle r^2\right\rangle\left\langle r^4\cos 4\phi\right\rangle + 5\left\langle r^6\right\rangle + 3\left\langle r^6\cos 4\phi\right\rangle) + \\ &4\varepsilon_s\left\langle r^2\right\rangle(-5\left\langle r^4\cos 2\phi\right\rangle\left\langle r^4\cos 4\phi\right\rangle + \left\langle r^8\cos 2\phi\right\rangle))))N) \end{aligned} \tag{A.98}$$

Published articles

Directed Flow at Midrapidity in $\sqrt{s_{NN}} = 2.76$ TeV Pb + Pb Collisions

Ekaterina Retinskaya,[1] Matthew Luzum,[2] and Jean-Yves Ollitrault[2]
[1]*CEA, IPhT, Institut de physique théorique de Saclay, F-91191 Gif-sur-Yvette, France*
[2]*CNRS, URA2306, IPhT, Institut de physique théorique de Saclay, F-91191 Gif-sur-Yvette, France*
(Received 6 March 2012; published 19 June 2012)

We analyze published data from the ALICE Collaboration in order to obtain the first extraction of the recently proposed rapidity-even directed flow observable v_1. An accounting of the correlation due to the conservation of transverse momentum restores the factorization seen by ALICE in all other Fourier harmonics and thus indicates that the remaining correlation gives a reliable measurement of directed flow. We then carry out the first viscous hydrodynamic calculation of directed flow, and show that it is less sensitive to viscosity than higher harmonics. This allows for a direct extraction of the dipole asymmetry of the initial state, providing a strict constraint on the nonequilibrium dynamics of the early-time system. A prediction is then made for v_1 in Au-Au collisions at RHIC.

DOI: 10.1103/PhysRevLett.108.252302 PACS numbers: 25.75.Ld, 24.10.Nz

Introduction.—Azimuthal correlations between particles emitted in heavy-ion collisions are a useful observable to probe the behavior of these systems [1]. Specifically, one measures the Fourier coefficient [2]

$$V_{n\Delta} \equiv \langle \cos n\Delta\varphi \rangle, \tag{1}$$

where $\Delta\varphi$ is the relative azimuthal angle between a pair of particles, and $\langle \cdots \rangle$ denotes an average over pairs and collisions. The long-range part of this correlation (defined by a rapidity gap between the pair) is mostly generated by collective, anisotropic flow of the strongly coupled matter created in the collision [3].

The most studied Fourier component is $V_{2\Delta}$ [4–6], corresponding to elliptic flow [7]. Recently it was realized that event-by-event fluctuations [2] generate a whole series of harmonics. This has triggered detailed analyses of $V_{n\Delta}$ for $n = 3$–6 [8–13].

Neglected in these analyses is the first Fourier harmonic $V_{1\Delta}$. The observed $V_{1\Delta}$ is smaller than $V_{2\Delta}$ and $V_{3\Delta}$ [3,10], and receives a sizable contribution from global momentum conservation [14,15], which makes its interpretation less straightforward. Fluctuations are expected to create a dipole asymmetry in the system [16], resulting in a specific directed flow pattern, with high transverse momentum particles flowing in the direction of the steepest gradient and low p_T particles flowing in the opposite direction. Hints of this directed flow have been extracted from published $V_{1\Delta}$ data at the Relativistic Heavy-Ion Collider (RHIC) by two of the authors [17], and its magnitude and p_T-dependence were shown to be in agreement with ideal hydrodynamic calculations [18]. Note that this quantity is distinct from the directed flow observable that has been obtained in the past from measurements employing a rapidity-odd projection [19]. That rapidity-odd v_1 gives a negligible contribution to $V_{1\Delta}$ near midrapidity and represents different physics [20].

In this Letter, we show that data on $V_{1\Delta}$ obtained by ALICE [10] can be explained by the superposition of two effects: global momentum conservation and directed flow. This allows for the first reliable measurement of directed flow at midrapidity. We then carry out the first viscous hydrodynamic calculation of directed flow, and show that these data can be used to constrain the initial dipole asymmetry of the system for each centrality, putting strong constraints on models of initial conditions.

Directed flow from dihadron correlations.—The standard picture of heavy-ion collisions is that an approximately thermalized fluid is created, which eventually breaks up into particles. Particles are emitted independently in each event, with an azimuthal distribution that fluctuates from event to event. This yields a two-particle correlation which factorizes into the product of two single-particle distributions [21]:

$$V_{n\Delta}(p_T^t, p_T^a) = v_n(p_T^t) v_n(p_T^a), \tag{2}$$

where the superscripts t and a refer to trigger and associated particles that can be taken from different bins in transverse momentum, and $v_n(p_T)$ is the anisotropic flow coefficient. Note that it is possible for the event-averaged correlation to not factorize even if independent emission holds in each event [21], and it is also possible for intrinsic ("nonflow") pair correlations to factorize [22]. However, flow is currently the only known mechanism that produces a factorized correlation in the range of transverse momentum studied here (the bulk of particles). This factorization has been tested in Pb-Pb collisions at the Large Hadron Collider (LHC) [10,12]: this is done by fitting the left-hand side of Eq. (2), which is a $N \times N$ symmetric matrix for N bins in p_T, with the right-hand side of Eq. (2), using the N values of $v_n(p_T)$ as fit parameters. The ALICE Collaboration has shown that, while the data do factorize for $n > 1$, this factorization breaks down for $n = 1$ [10]. This is not surprising since there is expected to be an additional long-range correlation induced by momentum conservation that only affects the first harmonic [14]. The constraint that all transverse momenta add up to 0 yields a back-to-back correlation between pairs, which increases linearly with the transverse momenta of both particles. This correlation adds to the correlation from flow:

$$V_{1\Delta}(p_T^t, p_T^a) = v_1(p_T^t)v_1(p_T^a) - kp_T^t p_T^a. \qquad (3)$$

(Note that the nonflow correlation also factorizes in this particular case [22], but the sum does not.) Table I compares the quality of the fit to $V_{1\Delta}$ using Eqs. (2) or (3). Adding one single fit parameter k tremendously increases the quality of the fit for all centrality windows. We have checked that the values of the fit parameters depend little on the p_T window. However, the quality of the fit decreases as higher p_T particles are included, as observed for other harmonics [10]. Nevertheless, we include the entire range of values as a systematic uncertainty in Table I, varying the lower p_T cutoff between 0.25 and 0.75 GeV, and the upper cutoff between 2.5 and 15.0 GeV. Similarly, we use this procedure to estimate a systematic uncertainty in v_1 (see Fig. 2 below).

Next, we check whether the value of k from the fit is compatible with the value expected from momentum conservation. Assuming for simplicity that momentum conservation is the only source of correlation, one obtains [14] $k = \langle \sum p_T^2 \rangle^{-1}$, where the sum runs over all particles emitted in one event, and the angular brackets denote an average over events in the centrality class. Since experiments measure only charged particles in a restricted phase-space window, only a rough estimate of this quantity can be made, by extrapolating from existing data. We have used the preliminary identified particle p_T spectra from ALICE at midrapidity [23], and extrapolated them outside the p_T acceptance of the detector using Levy fits [24]. In order to extrapolate to all rapidities, we have assumed for simplicity that the p_T spectra are independent of rapidity, and we have used the total charged multiplicity estimated by the ALICE Collaboration [25]. Neutral particles were taken into account assuming isospin symmetry, and the contribution of particles heavier than nucleons was neglected.

The resulting estimate is shown in the last column of Table I. The fit result in general has the correct size and increases with percent centrality, as expected. The centrality dependence is steeper than expected from our rough estimate, however—the fit value is larger than the estimated value for the most peripheral bin, while it is significantly smaller for central collisions. We cannot explain this, but overall the agreement is reasonable, and a discrepancy in k of this size has a very small effect on the extracted directed flow; the extracted directed flow curves with k fixed to the estimated values were also included in the systematic error band in v_1, but only have a small effect on the two most central bins.

TABLE I. From left to right: χ^2 per degree of freedom of the fit to the ALICE $V_{1\Delta}$ [10] (restricted to $p_T < 4$ GeV/c) using Eq. (2), and using Eq. (3); value of k from the fit; estimated value of k from momentum conservation in units of $10^{-5}(\text{GeV}/c)^{-2}$.

Centrality	χ^2, Eq. (2)	χ^2, Eq. (3)	k [10^{-5} GeV^{-2}]	$\langle \sum p_T^2 \rangle^{-1}$
0%–10%	6	2.0	$2.5^{+1.1}_{-0.3}$	6.1
10%–20%	16	1.7	$4.7^{+1.3}_{-0.4}$	8.8
20%–30%	45	2.1	$10.2^{+2.1}_{-0.5}$	13
30%–40%	75	2.2	$20.6^{+3.2}_{-1.6}$	21
40%–50%	126	2.4	$41.5^{+4.7}_{-3.0}$	35

It has been suggested that the correlation from momentum conservation could be larger than our estimate because of approximate conservation of transverse momentum within smaller subsystems of the entire collision system—specifically rapidity slices of roughly unit extent [26,27]. However, we see no evidence here for such an enhancement.

Thus, by taking into account the only obvious nonflow correlation, the factorization seen in higher harmonics is restored, and we can take the resulting $v_1(p_T)$ as a reliable measurement of directed flow v_1 (presented in Fig. 2 below).

Results of hydrodynamic calculations.—Relativistic viscous hydrodynamics has been shown to successfully reproduce v_n for $n = 2, 3, 4$ [28]. Here, we present the first viscous hydrodynamic calculation for directed flow, v_1. In hydrodynamics, v_1 and the corresponding event-plane angle Ψ_1 are defined by $v_1 e^{i\Psi_1} \equiv \langle e^{i\varphi} \rangle$, where angular brackets denote an average over the momentum distribution at freeze-out [29]. A collision of identical nuclei at midrapidity has $\varphi \rightarrow \varphi + \pi$ symmetry except for fluctuations; hence, v_1 at midrapidity is solely due to event-by-event fluctuations in the initial state.

In event-by-event ideal hydrodynamic calculations, v_1 was found [18] to be approximately proportional to the dipole asymmetry of the system ε_1 defined as [16]

$$\varepsilon_1 \equiv \frac{|\{r^3 e^{i\phi}\}|}{\{r^3\}}. \qquad (4)$$

where $\{\cdots\}$ denotes an average value over the initial energy density after recentering the coordinate system ($\{re^{i\phi}\} = 0$).

Here, in order to make a systematic study, we use a smooth, symmetric density profile which we deform to introduce a dipole asymmetry of the desired size and orientation. Specifically, our calculation is a 2 + 1 dimensional viscous hydrodynamic calculation which uses as initial condition the transverse energy density ($\epsilon(r, \phi)$) profile from an optical Glauber model [30], which is deformed in a way analogous to the previous study of v_3 and higher harmonics in Ref. [31]:

$$\epsilon(r, \phi) \rightarrow \epsilon(r\sqrt{1 + \delta\cos(\phi - \Phi_1)}, \phi), \qquad (5)$$

where δ is a small parameter. Both v_1 and ε_1 are proportional to δ for $\delta \ll 1$. For noncentral collisions, v_1 depends mildly on the orientation of the dipole asymmetry Φ_1 with respect to the impact parameter. Our results are averaged over Φ_1.

Figure 1 presents the ratio v_1/ε_1 as a function of the transverse momentum p_T for central collisions. Unlike higher-order harmonics, which are usually positive for all p_T, v_1 changes sign. The reason is that the net transverse momentum of the system is zero by construction, which implies $\langle p_T v_1(p_T)\rangle = 0$: low-$p_T$ particles tend to flow in the direction opposite to high-p_T particles.

The harmonics v_n tend to probe smaller length scales with increasing n, and as a result are expected to have an increasing sensitivity to viscosity. Our results show that, indeed, v_1 is less sensitive to viscosity than v_2 [32] and higher harmonics [28,31]. This insensitivity to viscosity combined with the approximate proportionality $v_1 \propto \varepsilon_1$ provides a unique opportunity to place a direct constraint on the dipole asymmetry of the early-time system.

In a realistic Pb-Pb collision, ε_1 varies from event to event. The contribution of directed flow to $V_{1\Delta}$ scales like ε_1^2. Therefore the experimentally measured v_1 scales like the root-mean-square (rms) value of ε_1 in the centrality bin. As we shall see below, there is a wide range of predictions for this quantity. With these new data we can now quickly discern which are compatible with experiment by identifying an allowed range of values for the rms dipole asymmetry.

Figure 2 displays v_1 versus p_T extracted from ALICE correlation data using Eq. (3). The magnitude and p_T dependence of v_1 are similar at LHC and at RHIC [17], and the mild centrality dependence, reminiscent of v_3 [8,9], is expected since both are generated purely from fluctuations in the initial state.

The p_T dependence of v_1 in LHC data bears a striking resemblance to that predicted by hydrodynamics (Fig. 1). In a given centrality window and for a given value of the viscosity, one can tune the value of the dipole asymmetry ε_1 in the hydrodynamic calculation so as to obtain reasonable agreement with data. If one chooses to match data at the lowest p_T, calculation overpredicts data at high p_T. Conversely, if one matches data at high p_T, calculation underpredicts data at low p_T. The corresponding values of ε_1 can be considered upper and lower bounds on the actual value.

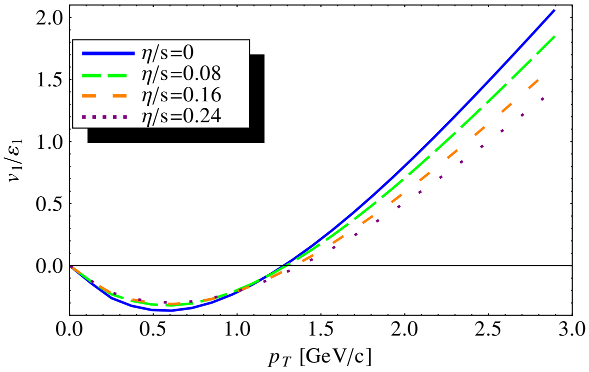

FIG. 1 (color online). Directed flow v_1, scaled by the initial dipole asymmetry ε_1, in a central Pb-Pb collision at 2.76 TeV, for different values of the shear viscosity to entropy ratio η/s.

The values of η/s (the ratio of shear viscosity to entropy density) implied by comparisons of elliptic flow data to hydrodynamic calculations all lie in the range $0 < \eta/s < 0.24$ [30,33,34]. Assuming that η/s lies in this range, we can extract an allowed range for the dipole asymmetry, using the extremal values of η/s and ε_1 that still give a reasonable fit to data (the extremal curves used are shown in Fig. 2).

Figure 3 displays the allowed values of ε_1 as a function of centrality, together with the rms ε_1 from various Monte Carlo models of initial conditions. The allowed range assuming $0.08 < \eta/s < 0.16$, representing the most common values extracted from v_2 data, are also shown in a darker band, to illustrate the small effect of viscosity. Both the order of magnitude and the centrality dependence of ε_1 from Monte Carlo models resemble the allowed values from LHC data. However, there are significant differences between the models. LHC data already exclude DIPSY [35] above 10% centrality, and the Phobos Glauber model [36] as well as a recent improved MCKT model with KNO fluctuations [37] over the entire centrality range.

Note, however, that since hydrodynamics is expected to be more reliable at low transverse momentum, the actual value of ε_1 is most likely to lie very close to our upper

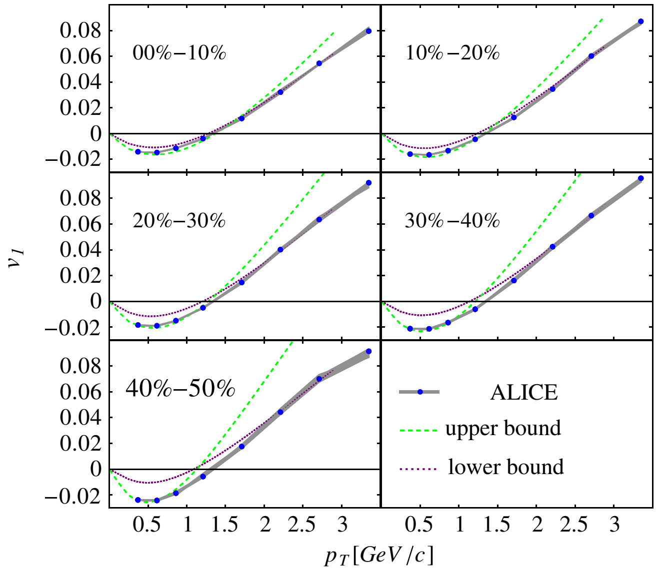

FIG. 2 (color online). $v_1(p_T)$ in Pb-Pb collisions at 2.76 TeV extracted from correlation data [10], in various centrality windows. The shaded band represents the systematic uncertainty from the choice of p_T window used for the fit. The curves are hydrodynamic calculations, where the value of ε_1 has been adjusted so as to match the data from above or below, that were used to obtain the upper and lower bound, respectively, in Fig. 3.

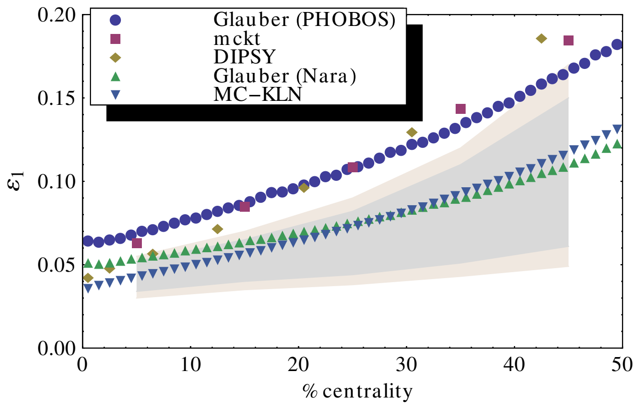

FIG. 3 (color online). Variation of ε_1 with centrality. The shaded bands indicate the allowed regions using ALICE data in combination with viscous hydrodynamics, assuming either $0 < \eta/s < 0.24$ (lighter shade) or $0.08 < \eta/s < 0.16$ (darker shade). Also shown are the prediction of several Monte Carlo models of initial conditions: DIPSY [35], MC-KLN (obtained from MCKT V1.00) [38,39], MCKT V1.25 [37,39], and two different implementations of the Glauber model utilizing pointlike nucleons [36] or uniform disks [39]. The binary collision fraction for both Glauber models was taken to be $x = 0.18$ [40].

bound. Thus it is possible that the two models with the largest dipole asymmetry may only need a slight tuning to achieve a correct value, while the value from the others may in fact be too low. We prefer here to be conservative in our claimed region of allowed values and leave it to future study for more stringent conclusions.

Models such as those presented here do not in general predict a significant change in dipole asymmetry with collision energy. By extracting a best value of ε_1 from these LHC data combined with hydrodynamic calculations of lower energy collisions, we can make predictions for Au-Au collisions at RHIC assuming little change in the average dipole asymmetry in a centrality bin. Since the change of ε_1 with collision energy predicted by each current Monte Carlo model is much smaller than the range spanned by the various models, this prediction is more reliable than any obtained by assuming a particular model for the initial conditions. These are presented in Fig. 4. The value of ε_1 at LHC is obtained by taking the best fit to the experimental v_1 for $p_T < 1.5$ GeV/c, which is the range where hydrodynamics agrees best with data [29]. Our calculations use $\eta/s = 0.16$ both at LHC and at RHIC, but the extrapolation from LHC to RHIC depends very weakly on the assumed value of η/s [30].

These predictions are compatible with the attempted extraction of v_1 [17] from a much more limited set of correlation data at 20%–60% centrality released by the STAR Collaboration, but a dedicated analysis by one of the experimental collaborations at RHIC will allow for a much more precise test, including centrality dependence.

Conclusions.—We have shown that the first Fourier component of the two-particle azimuthal correlation measured at LHC, $V_{1\Delta}$, can be explained by collective flow, much in the same way as higher harmonics, after the correlation from momentum conservation is accounted for. We have thus obtained the first measurement of directed flow, v_1, at midrapidity at the LHC. This experimental result was compared with the first viscous hydrodynamic calculation of directed flow. v_1 was found to have a weaker dependence on viscosity than v_2 and v_3, which allows for the first time a tight constraint to be placed directly on the geometry and fluctuations of the early-time system, and which rules out certain current theoretical models. The extracted values of the dipole asymmetry of the initial conditions then allow for predictions to be made for directed flow at midrapidity in lower-energy collisions at RHIC, which were presented.

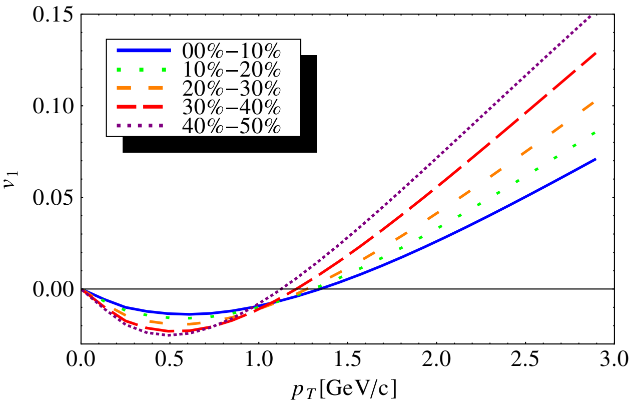

FIG. 4 (color online). Viscous hydrodynamic prediction for v_1 in Au-Au collisions at 200 GeV in various centrality windows.

For providing experimental data from the ALICE Collaboration we would like to thank Andrew Adare and Mateusz Ploskon. M. L. is supported by the European Research Council under the Advanced Investigator Grant No. ERC-AD-267258.

[1] S. A. Voloshin, A. M. Poskanzer, and R. Snellings, arXiv:0809.2949.
[2] B. Alver and G. Roland, Phys. Rev. C **81**, 054905 (2010); **82**, 039903(E) (2010).
[3] M. Luzum, Phys. Lett. B **696**, 499 (2011).
[4] K. Adcox *et al.* (PHENIX Collaboration), Phys. Rev. Lett. **89**, 212301 (2002).
[5] C. Adler *et al.* (STAR Collaboration), Phys. Rev. C **66**, 034904 (2002).
[6] K. Aamodt *et al.* (ALICE Collaboration), Phys. Rev. Lett. **105**, 252302 (2010).
[7] J. Y. Ollitrault, Phys. Rev. D **46**, 229 (1992).
[8] A. Adare *et al.* (PHENIX Collaboration), Phys. Rev. Lett. **107**, 252301 (2011).
[9] C. A. Loizides *et al.* (ALICE Collaboration), Phys. Rev. Lett. **107**, 032301 (2011).
[10] K. Aamodt *et al.* (ALICE Collaboration), Phys. Lett. B **708**, 249 (2012).

[11] J. Jia (ATLAS Collaboration), J. Phys. G **38**, 124012 (2011).
[12] CMS Collaboration, arXiv:1201.3158.
[13] P. Sorensen (STAR Collaboration), J. Phys. G **38**, 124029 (2011).
[14] N. Borghini, P. M. Dinh, and J. Y. Ollitrault, Phys. Rev. C **62**, 034902 (2000).
[15] N. Borghini, P. M. Dinh, J. Y. Ollitrault, A. M. Poskanzer, and S. A. Voloshin, Phys. Rev. C **66**, 014901 (2002).
[16] D. Teaney and L. Yan, Phys. Rev. C **83**, 064904 (2011).
[17] M. Luzum and J. Y. Ollitrault, Phys. Rev. Lett. **106**, 102301 (2011).
[18] F. G. Gardim, F. Grassi, Y. Hama, M. Luzum, and J. Y. Ollitrault, Phys. Rev. C **83**, 064901 (2011).
[19] I. Selyuzhenkov, J. Phys. G **38**, 124167 (2011).
[20] P. Bozek and I. Wyskiel, Phys. Rev. C **81**, 054902 (2010).
[21] M. Luzum, J. Phys. G **38**, 124026 (2011).
[22] D. Kikola, L. Yi, S. Esumi, F. Wang, and W. Xie, arXiv:1110.4809.
[23] R. Preghenella (for the ALICE Collaboration), Acta Phys. Pol. B **43**, 555 (2012).
[24] K. Aamodt *et al.* (ALICE Collaboration), Eur. Phys. J. C **71**, 1655 (2011).
[25] A. Toia, J. Phys. G **38**, 124007 (2011) .
[26] N. Borghini, Phys. Rev. C **75**, 021904 (2007).
[27] Z. Chajecki and M. Lisa, Phys. Rev. C **79**, 034908 (2009).
[28] B. Schenke, S. Jeon, and C. Gale, Phys. Rev. C **85**, 024901 (2012).
[29] P. F. Kolb and U. W. Heinz, arXiv:nucl-th/0305084.
[30] M. Luzum and P. Romatschke, Phys. Rev. Lett. **103**, 262302 (2009).
[31] B. H. Alver, C. Gombeaud, M. Luzum, and J. Y. Ollitrault, Phys. Rev. C **82**, 034913 (2010).
[32] M. Luzum and P. Romatschke, Phys. Rev. C **78**, 034915 (2008); **79**, 039903(E) (2009).
[33] B. Schenke, S. Jeon, and C. Gale, Phys. Lett. B **702**, 59 (2011).
[34] C. Shen, U. Heinz, P. Huovinen, and H. Song, Phys. Rev. C **84**, 044903 (2011).
[35] C. Flensburg, arXiv:1108.4862.
[36] B. Alver, M. Baker, C. Loizides, and P. Steinberg, arXiv:0805.4411.
[37] A. Dumitru and Y. Nara, Phys. Rev. C **85**, 034907 (2012).
[38] J. L. Albacete and A. Dumitru, arXiv:1011.5161.
[39] Code by A. Dumitru, a fork of MC-KLN by Y. Nara. Versions 1.00 and 1.25 obtained from http://physics.baruch.cuny.edu/files/CGC/CGC_IC.html
[40] P. Bozek, M. Chojnacki, W. Florkowski, and B. Tomasik, Phys. Lett. B **694**, 238 (2010).

PHYSICAL REVIEW C **89**, 014902 (2014)

Constraining models of initial conditions with elliptic and triangular flow data

Ekaterina Retinskaya,[1] Matthew Luzum,[2,3] and Jean-Yves Ollitrault[4]
[1]*CEA, IPhT, Institut de physique théorique de Saclay, F-91191 Gif-sur-Yvette, France*
[2]*McGill University, 3600 University Street, Montreal QC H3A 2TS, Canada*
[3]*Lawrence Berkeley National Laboratory, Berkeley, California 94720, USA*
[4]*CNRS, URA2306, IPhT, Institut de physique théorique de Saclay, F-91191 Gif-sur-Yvette, France*

(Received 22 November 2013; published 8 January 2014)

We carry out a combined analysis of elliptic and triangular flow data using viscous relativistic hydrodynamics. We show that these data allow us to put tight constraints on models of the early dynamics of a nucleus-nucleus collision. Specifically, the rms values of the initial ellipticity ε_2 and the initial triangularity ε_3 are constrained to lie within a narrow band for each centrality. We use these constraints as a filter for existing Monte Carlo models of initial state, and provide a simple test that can be performed on any candidate model to determine its compatibility with data.

DOI: 10.1103/PhysRevC.89.014902 PACS number(s): 25.75.Ld, 25.75.Gz, 24.10.Nz

I. INTRODUCTION

Anisotropic flow [1] in heavy-ion collisions is understood as the hydrodynamic response [2] of the strongly interacting medium to a spatial anisotropy created in the early stages of the collision. Elliptic flow, v_2 [3,4], originates from the almond shape of the overlap area between the colliding nuclei [5]. Similarly, triangular flow, v_3, is generated by fluctuations of the initial density profile which have a triangular shape [6].

It has long been recognized that the extraction of transport coefficients of the strongly-coupled quark-gluon plasma (in particular, its viscosity over entropy density ratio η/s [7]) from elliptic flow data is hindered by the poor knowledge of the initial geometry [8]. Specifically, different models of the initial state, supplemented with viscous hydrodynamic evolution, can be made compatible with experimental elliptic flow data at the expense of tuning η/s. More recently, a large number of new flow observables have been measured, which can add extra nontrivial constraints. For example, it was noticed that, while either elliptic flow or triangular flow data could be reasonably fit individually by tuning the viscosity in a hydrodynamic calculation, only some models of the initial state could be made compatible with both. Thus, some models can actually be ruled out [9,10].

The goal of this paper is to propose a systematic approach for constraining models of initial conditions using anisotropic flow data. Early work in this direction was done by the ALICE Collaboration, which was able to place constraints on the relative centrality dependence of the initial eccentricity for very central collisions at the Large Hadron Collider (LHC), without having to perform hydrodynamic calculations [11]. Here, by combining hydrodynamic simulations with data from Au-Au collisions at $\sqrt{s_{NN}} = 0.2$ TeV [10] and Pb-Pb collisions at $\sqrt{s_{NN}} = 2.76$ TeV [11], we are able to place strong constraints at all centralities. We then use these constraints as a filter for existing models of initial conditions, and we provide a simple test that can be applied to any future model to quickly and easily determine whether it is compatible with these data.

II. METHODOLOGY

The observable we choose for this study is the integrated [12] anisotropic flow v_n, i.e., averaged over the particle transverse momentum. The reason is twofold: First, hydrodynamics is meant to describe the bulk features of particle production, therefore its most robust predictions are for bulk observables. Second, differential anisotropic flow (i.e., its relative dependence on transverse momentum) does not depend much on the initial state:[1] predictions of ideal (nonviscous) hydrodynamics for the differential v_n are to some extent universal [9,15], while viscous corrections are determined by the late stages of the collision [16,17]. Therefore one does not lose essential information on the initial state by considering only the integrated anisotropic flow.

We only use two out of the six Fourier harmonics which have been measured [18], namely v_2 and v_3. Again, the reason is twofold: First, they are the largest harmonics for all centralities, hence they are determined with better accuracy. Second, in these two harmonics, the hydrodynamic response to the initial state is dominated by simple linear response [19]. Specifically, elliptic flow v_2 in hydrodynamics is to a good approximation [20] proportional to the participant ellipticity ε_2 [21] and triangular flow is proportional [22] to the participant triangularity ε_3 [6]. ε_n with $n > 1$ is generally defined as [2,23]

$$\varepsilon_n \equiv \frac{\left|\int r^n e^{in\phi}\epsilon(r,\phi) r\, dr\, d\phi\right|}{\int r^n \epsilon(r,\phi) r\, dr\, d\phi}, \tag{1}$$

where integration is over the transverse plane in polar coordinates, and $\epsilon(r,\phi)$ denotes the energy density at $z \sim 0$. The system is centered, so that $\int r e^{i\phi}\epsilon(r,\phi) r\, dr\, d\phi = 0$.

---

[1] Except at high transverse momentum where a granular density profile yields less anisotropic flow [13] than a smooth density profile. This effect [14] could be used to study such additional features of the initial state, but we will see that those features do not affect the conclusions in this work.

Linear response is also a reasonable approximation for v_1 [24], with a specific definition of the dipole asymmetry ε_1 [2]. The constraints on the initial state from v_1 were studied in a previous publication [25]. Higher order Fourier harmonics of anisotropic flow (v_4, v_5, v_6) have a more complicated relation to initial-state properties because of large nonlinear terms in the hydrodynamic response [15,26–28].

The linear-response approximation states

$$v_n = \left(\frac{v_n}{\varepsilon_n}\right)_h \varepsilon_n, \tag{2}$$

with $n = 2,3$, where v_n on the left-hand side is the measured flow in a given collision event. The first factor on the right-hand side is the hydrodynamic response to the initial anisotropy [2,9], which is assumed independent of the initial profile for a given centrality, while the second factor depends only on the initial state and encodes all information about event-by-event fluctuations. Experimental data for moments of the event-by-event v_2 and v_3 distribution, combined with hydrodynamical calculations of $(v_2/\varepsilon_2)_h$ and $(v_3/\varepsilon_3)_h$, thus yield the values of the same moments of the initial anisotropies ε_2 and ε_3. Here, we use ALICE data inferred from two-particle correlations [11] and PHENIX data which use an event-plane method [10]. In practice, both methods yield the root-mean-square (rms) value of the event-by-event distribution of v_n [29].[2] Equation (2) gives

$$\sqrt{\langle v_n\rangle^2} = \left(\frac{v_n}{\varepsilon_n}\right)_h \sqrt{\langle \varepsilon_n\rangle^2}\ . \tag{3}$$

Therefore the constraints we obtain on ε_n also relate to rms values.

There are several sources of uncertainties in the hydrodynamic response: once these uncertainties are taken into account, the predictions span some region in the (rms ε_3,rms ε_2) plane. As we show in Sec. III, this region turns out to be a narrow band. This puts strong constraints on existing models of initial conditions, which are scrutinized in Sec. IV.

III. UNCERTAINTIES IN THE RESPONSE

Hydrodynamical modeling [32] consists of three stages. It first uses as input an initial condition for the energy-momentum tensor of the system at an early stage of the collision, which is provided by some model of the early dynamics. Second, one evolves this initial condition through the equations of relativistic hydrodynamics. Finally, the fluid is converted into hadrons. Every step of this calculation comes with its own uncertainties. Investigating sources of uncertainty [33] in hydrodynamic modeling requires one to carry out a large number of numerical calculations, and the computational effort of a state-of-the-art calculation can become prohibitively expensive [34]. This cost can be reduced by orders of magnitude at the expense of a few simplifying assumptions. For each of the three stages, we now describe the simplifications which can be made, and identify the leading source of uncertainty.

1. Initial conditions. Our calculation uses boost-invariant initial conditions [35]. This amounts to neglecting the rapidity dependence of correlations due to anisotropic flow, which is known to be small at LHC energies [18,36] but may be larger at the Relativistic Heavy Ion Collder (RHIC) [37]. In order to compute the hydrodynamic response in the second harmonic, $(v_2/\varepsilon_2)_h$, we parametrize the transverse density with an optical Glauber model, with an impact parameter that corresponds to the rms impact parameter of each bin in a Monte Carlo Glauber calculation. The overall normalization is then set to match the observed charged multiplicity [38,39]. In a centered polar coordinate system (r,ϕ), the optical Glauber profile has $\phi \to \phi + \pi$ symmetry for a symmetric collision, hence $\varepsilon_3 = v_3 = 0$. In order to compute the response v_3/ε_3, we introduce by hand a triangularity by deforming the optical Glauber profile as follows [9]:

$$\epsilon(r,\phi) \to \epsilon(r\sqrt{1+\varepsilon_3' \cos[3(\phi-\Phi_3)]},\phi), \tag{4}$$

where ε_3' is magnitude of the deformation, and Φ_3 its orientation. The nonlinear coupling between v_2 and v_3 [27] induces a small modulation of v_3 with Φ_3, whose relative magnitude scales like $(\varepsilon_2)^3\cos(6\Phi_3)$ (the reaction plane is chosen along the x axis). We find this dependence to be 1% or less in all cases: therefore we neglect it and choose $\Phi_3 = 0$ for all calculations. We have also checked that the dependence of the ratio $(v_3/\varepsilon_3)_h$ on the values chosen for ε_3' [9] is negligible. This calculation uses the same values of ε_3' as [9]. Note that recentering the distribution after deformation shifts the center by a distance proportional to $\varepsilon_2\varepsilon_3$. This in turn results in a decrease of ε_3 of relative order $(\varepsilon_2)^2$. This recentering correction was neglected in [9] and the hydrodynamic response was therefore underestimated by up to 10% for peripheral collisions.

Within our linear-response approximation (2), the hydrodynamic response $(v_n/\varepsilon_n)_h$ is assumed independent of the fine structure of the initial profile. Event-by-event ideal hydrodynamic calculations [40] have proven that a such a "single-shot" calculation with smooth initial condition yields the same value of $(v_n/\varepsilon_n)_h$, within a few percent, as a calculation with fluctuating initial conditions averaged over many events, while event-by-event viscous hydrodynamic calculations show an even stronger correlation between initial anisotropy ε_n and v_n [19].

In order to estimate quantitatively the dependence of $(v_n/\varepsilon_n)_h$ over the initial profile, we use two different definitions of ε_n, weighted either with energy density [as in Eq. (1)] or with entropy density. Both weightings yield approximately equally good predictors of v_n [26]. So any difference in prediction from one weighting versus the other is an indication of the size of the uncertainty due to the linear approximation. For central collisions, the particular deformation that we choose to create triangular flow, Eq. (4), gives the exactly same value of ε_3 irrespective of whether one weights with entropy or energy [9]: therefore our calculation is unable to tell the difference between the two. However, values of ε_2 differ for the optical Glauber model, and we use the resulting difference in $(v_2/\varepsilon_2)_h$ as part of our error bar.

---

[2] The event-plane method gives a result which coincides with the rms value in the limit of low resolution [30], and the PHENIX analysis has a low resolution [31].

The thermalization time t_0, at which hydrodynamics becomes a good approximation [41], is poorly constrained. Early calculations [42] used to neglect transverse flow for $t \leqslant t_0$ (where t_0 is typically of order 1 fm$/c$). However, the transverse expansion starts immediately after the collision, whether or not the system thermalizes. This "initial flow" has proven essential in understanding interferometry data [43–45]. Furthermore, it is to some extent universal [46] and can be obtained simply, in a traditional calculation with vanishing flow at t_0, by letting t_0 go to unrealistically small values [44]. In order to estimate the uncertainty due to initial flow, we run two sets of calculations with $t_0 = 0.5$ fm$/c$ and $t_0 = 1$ fm$/c$; linearity of initial transverse flow at early times [47] can then be used to extrapolate to smaller values.

2. *Fluid expansion*. The main source of uncertainty in the hydrodynamic evolution itself is the value of the shear viscosity of the strongly interacting quark-gluon plasma, which is poorly constrained so far, either from theory [48] or experiment [33,49]. We take this uncertainty into account by varying η/s from 0 to 0.24 in steps of 0.04. If η/s is too large, hydrodynamics itself breaks down [50]. Effects of bulk viscosity [16,51] on the integrated flow are smaller [52], even though the bulk viscosity may be large for some values of the temperature [53]. Second-order corrections [54] have a negligible effect [8].

3. *Hadronic stage*. Eventually, the fluid expands and can be described as a gas of hadrons with collective and thermal motion. An open question in the description of the hadronic phase is to what extent hydrodynamics is a valid approach. Instead, a common approach at RHIC energies was to couple hydrodynamics to a hadronic "afterburner" simulating hadronic decays and two-body collisions [55–57]. Although these afterburners usually have little affect on integrated properties of unidentified hadrons, this approach has proven useful for reproducing the elliptic flow and momentum spectra of identified particles. Hadronic afterburners are also being implemented at LHC energies [58,59]. Besides, it has been pointed out that hydrodynamics with bulk viscosity in the hadronic phase [60] also succeeds in reproducing identified particle properties [61].

In this paper, we assume for simplicity that hydrodynamics still applies in the hadronic phase, with a single freeze-out temperature [42]. When changing the initial time in the hydrodynamic calculation, we tune the freeze-out temperature in such a way that the average transverse momentum of charged particles $\langle p_T \rangle$ is unchanged: smaller values of t_0 thus imply larger freeze-out temperatures. We neglect hadronic collisions below freeze-out, but resonance decays are taken into account.

In viscous hydrodynamics, a significant source of uncertainty is the momentum distribution at freeze-out, which deviates from a thermal distribution due to the viscous correction [62,63]. The momentum dependence of this viscous correction involves microscopic information about hadronic cross sections [64]. The quadratic ansatz [62] is the most commonly used. However, a linear ansatz gives better agreement with v_4 data [65]. In order to estimate the uncertainty associated with the modeling of freeze-out, we perform two sets of calculations with the linear and quadratic ansatz.

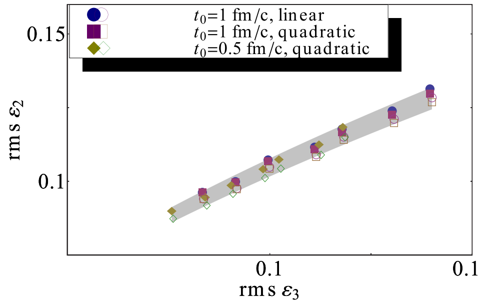

FIG. 1. (Color online) Root-mean-square values of $(\varepsilon_2,\varepsilon_3)$ implied by hydrodynamic calculations in combination with ALICE data for the 5% most central Pb-Pb collisions at $\sqrt{s_{NN}} = 2.76$ TeV. Squares: $t_0 = 1$ fm$/c$ with quadratic freeze-out. Circles: $t_0 = 1$ fm$/c$ with linear freeze-out. Diamonds: $t_0 = 0.5$ fm$/c$ with quadratic freeze-out. Closed symbols correspond to energy density weighting, open symbols to entropy density weighting. For each symbol type, the 7 points correspond to different values of η/s, from 0 to 0.24 (from left to right) in steps of 0.04. The shaded band is the area between two curves of the type (5) with $C = C_{\min}$ and $C = C_{\max}$, where the values of $C_{\min}$ and $C_{\max}$ are chosen such that all hydrodynamic points lie within the band.

The code we use to solve hydrodynamics is the same as in Ref. [38], with resonance decays taken into account after freeze-out.

We compute v_2 and v_3 for outgoing hadrons using similar experimental cuts as the experimental data that we compare to. Specifically, the ALICE Collaboration [11] analyzes v_n for all charged hadrons in transverse momentum range $0.2 < p_t < 5$ GeV$/c$ and pseudorapidity range $|\eta| < 0.8$. The PHENIX Collaboration [10] uses the cuts $0.25 < p_t < 4$ GeV$/c$ and $|\eta| < 0.35$. Since our model has longitudinal boost invariance, our results are independent of rapidity. Because of the difference in rapidity and pseudorapidity, however, the cut in η must be taken into account in a precision calculation [66]. It typically increases v_2 by 3% and v_3 by 4%.

An additional subtlety of the ALICE analysis is that the method uses pair correlations, with a pseudorapidity gap $|\Delta\eta| > 1$ between particles in the pair in order to suppress nonflow correlations [67]. The analysis thus excludes particles at $|\eta| < 0.2$, and gives more weight to particles near the boundary $|\eta| = 0.8$, since all *pairs* are weighted identically. We also take into account this additional cut in $\Delta\eta$, which typically decreases v_2 by 0.3% and v_3 by 0.4%.

Figure 1 illustrates the effects of several sources of uncertainty on the root-mean-square values of $(\varepsilon_2,\varepsilon_3)$ extracted from Eq. (3) (for the 5% most central Pb-Pb collisions at the LHC). Each point represents a hydrodynamic calculation with different parameters. As the viscosity increases, the hydrodynamic response $(v_n/\varepsilon_n)_h$ decreases, therefore the rms ε_n increases. The lines drawn in the $(\varepsilon_3,\varepsilon_2)$ plane as η/s varies are well fitted by a power law:

$$\sqrt{\langle \varepsilon_2^2 \rangle} = C\left(\sqrt{\langle \varepsilon_3^2 \rangle}\right)^k, \tag{5}$$

where $k = 0.6$, and C is fixed. k is the ratio of the relative change in v_2 to the relative change in v_3 when η/s increases.

The fact that $k < 1$ expresses that viscosity has a smaller effect on v_2 than on v_3.

Other sources of uncertainty in the hydrodynamic prediction result in uncertainties in the coefficient C in Eq. (5). Switching from the quadratic to the linear freeze-out ansatz has a very small effect, which is visible only for the largest values of η/s. Adding initial flow by starting the evolution earlier, at $t_0 = 0.5$ fm/c, yields more flow for a given value of η/s, resulting in smaller values of ε_n. Although this result may seem natural, it is not trivial as it looks: the freeze-out temperature is adjusted so as to match the p_t spectrum, so that smaller t_0 goes along with earlier freeze-out. Both effects essentially compensate each other at RHIC energies [8], so that final results were insensitive to t_0. The situation is different at LHC energies: in general, hydrodynamic results are less sensitive to the hadronic phase [68] and to the freeze-out temperature, which results in a stronger sensitivity of ε_n to initial flow.

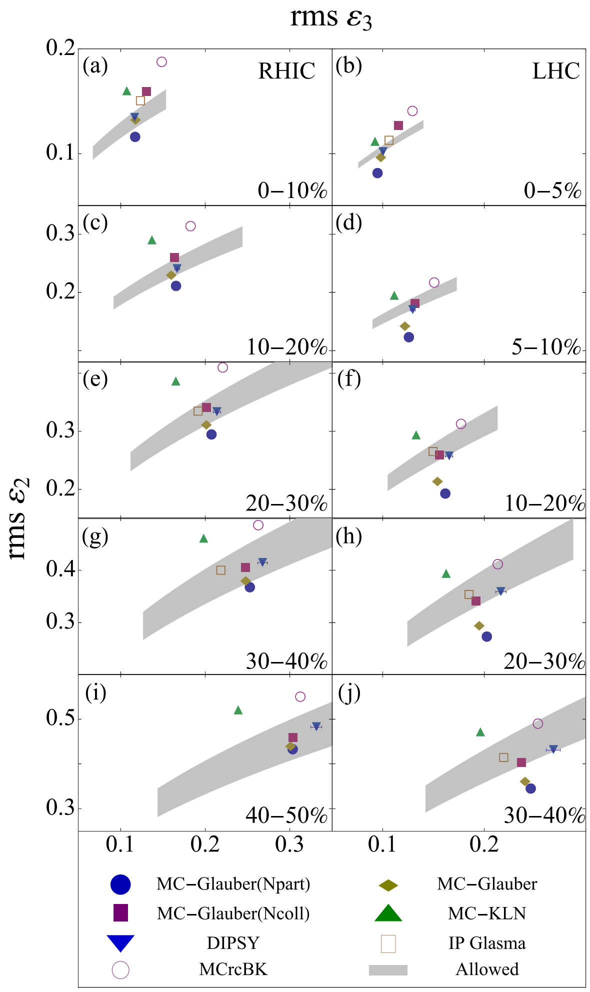

FIG. 2. (Color online) Shaded bands are root-mean-square values of (ε_2,ε_3) allowed by experimental data in combination with hydrodynamic calculations, for Au-Au collisions at $\sqrt{s_{NN}} = 0.2$ TeV (left) [10] and Pb-Pb collisions at $\sqrt{s_{NN}} = 2.76$ TeV (right) [11] in various centrality windows (from top to bottom). Symbols are predictions from various models of initial conditions (see text for details).

TABLE I. Values of the ratio $\sqrt{\langle\varepsilon_2^2\rangle}/\sqrt{\langle\varepsilon_3^2\rangle}^{0.5}$ at RHIC. First two lines: minimum and maximum values allowed by hydrodynamics and experimental data. Next lines: values predicted by various models.

% centrality	0–10	10–20	20–30	30–40	40–50
minimum	0.36	0.56	0.69	0.75	0.74
maximum	0.41	0.63	0.79	0.90	0.91
MC-Glauber	0.38	0.57	0.69	0.76	0.80
MC-Glauber (N_{coll})	0.44	0.64	0.76	0.81	0.83
MC-Glauber (N_{part})	0.34	0.52	0.64	0.73	0.78
MC-KLN	0.49	0.78	0.95	1.03	1.06
MC-rcBK	0.49	0.73	0.87	0.95	0.98
IP-Glasma	0.43		0.76	0.85	
DIPSY	0.39	0.59	0.72	0.80	0.84

In general, the takeaway message is that any effect that causes stronger collective flow tends to increase both ε_2 and ε_3 in such a way that the coefficient C in Eq. (5) is almost unchanged.

In fact, the largest contribution to the thickness of the uncertainty band comes not from properties of the medium or physical parameters, but instead from the linear-response approximation itself: weighting with entropy rather than energy yields slightly smaller values of ε_2, while ε_3 remains the same.

Once all sources of uncertainties are taken into account, one is left with an allowed region in the (ε_2,ε_3) plane, corresponding to an allowed interval for the coefficient C in Eq. (5). The same procedure can be repeated for other centrality intervals, and at lower energy. The value $k = 0.6$ in Eq. (5) gives a good fit for all centralities at LHC, while $k = 0.5$ gives a better fit at RHIC. These allowed regions are displayed as shaded bands in Fig. 2. The uncertainty becomes larger as centrality percentile increases, which is mostly due to the difference between energy and entropy weighting. The minimum and maximum values of C are listed in Tables I and II for RHIC and LHC, respectively. In the same centrality range, the allowed band at LHC is slightly higher than at RHIC, but they overlap.

IV. TESTING INITIAL STATE MODELS

We now use the values of the rms ellipticity ε_2 and triangularity ε_3 obtained from data and hydrodynamic calculations

TABLE II. Values of the ratio $\sqrt{\langle\varepsilon_2^2\rangle}/\sqrt{\langle\varepsilon_3^2\rangle}^{0.6}$ at LHC.

% centrality	0–5	5–10	10–20	20–30	30–40
minimum	0.40	0.58	0.76	0.88	0.94
maximum	0.43	0.65	0.87	1.06	1.13
MC-Glauber	0.39	0.50	0.66	0.78	0.85
MC-Glauber (N_{coll})	0.46	0.61	0.79	0.92	0.96
MC-Glauber (N_{part})	0.33	0.42	0.57	0.71	0.80
MC-KLN	0.46	0.73	0.98	1.17	1.25
MC-rcBK	0.48	0.67	0.88	1.04	1.12
IP-Glasma	0.43		0.83	0.97	1.03
DIPSY	0.40	0.58	0.76	0.90	0.95

as a filter for existing models of the initial state. Since ε_3 is solely created by fluctuations of the initial geometry [6], in order to be consistent with data there is a trivial requirement that models take these fluctuations into account—typically these are Monte Carlo models. The simplest is the Glauber model [69], where each participant nucleon adds a contribution to the initial density with Gaussian shape (in x and y) and width $\sigma = 0.4$ fm, a value commonly used in event-by-event hydrodynamic calculations [20,70,71]. We use the PHOBOS Monte Carlo Glauber model [72], though other implementations exist [73,74]. Each participant can be given equal weight (referred to as "Glauber N_{part}"), or a weight proportional to its number of collisions (referred to as "Glauber N_{coll}" scaling), or a linear combination of the two, adjusted to match observed multiplicity spectra (default version, referred to simply as "Glauber") at RHIC [75] and LHC [76].

Another class of initial state models, which generically go under the name CGC, implement the idea of parton saturation [77]. They generally predict a larger ε_2 [56,78]. In the earliest Monte Carlo implementation [79], which we denote by MC-KLN, the source of fluctuations is essentially the same as in Glauber models, resulting in similar values of ε_3. Recent works tend to incorporate additional sources of fluctuations, at the subnucleonic level [80–83], resulting in general in larger ε_3. Specifically, we test the MC-rcBK model which incorporates negative binomial fluctuations in nucleon-nucleon collisions [82], the DIPSY model [81] which incorporates a BFKL gluon cascade, and the IP-Glasma model [83] which involves a classical Yang-Mills description of early-time gluon fields.

In all cases, centrality bins are assigned according to the total entropy of each Monte Carlo event, which corresponds closely to the total multiplicity that would be obtained after hydrodynamic evolution. Since the experimental centrality selection is also closely related to multiplicity, any systematics from centrality selection adds a negligible uncertainty and does not affect any of the following conclusions

Predictions of these initial-state models are plotted in Fig. 2, together with constrains from data and hydrodynamics. They are generally in the ballpark for all centralities. All models predict a strong increase of the rms ε_2 with centrality percentile (as the overlap area between colliding nuclei becomes more elongated) and a mild increase of the rms ε_3, driven by the decrease in the system size [84]. The evolution from RHIC to LHC at the same centrality depends on the model. The Glauber model predicts a decrease of both ε_2 and ε_3 by a few percent, which is only partially explained by the increase in system size from Au to Pb. The MC-rcBK predicts similar values at RHIC and LHC. Finally, DIPSY predicts a mild increase of ε_2 while ε_3 is unchanged.

Equation (5) provides a simple criterion for checking whether or not a particular model of initial conditions is compatible with data and hydrodynamics: one computes $\sqrt{\langle\varepsilon_2^2\rangle}/\sqrt{\langle\varepsilon_3^2\rangle}^k$ for this model, with $k = 0.5$ (0.6) at RHIC (LHC), and checks whether the result falls within the allowed band. This comparison is carried out in Tables I and II. One sees that the MC-KLN is excluded for all centralities at RHIC and LHC. It has already be noted that this particular model underpredicts v_3 at RHIC if tuned to reproduce v_2 [9,10]. The MC-rcBK model is also excluded at RHIC, and marginally allowed at LHC. The Glauber model (in its default version with a superposition of number of participants and number of binary collisions) falls within the allowed band at RHIC, but is excluded at LHC, except for the most central bin. DIPSY and IP-Glasma fall within the allowed region for all centralities, and so does the Glauber model with pure binary collision scaling.

The statement of whether a particular model of initial conditions is compatible with data or not turns out to be quite robust with respect to several ambiguities in the definitions of ε_2 and ε_3. In the Glauber model, for instance, one treats each participant as a "source", whose width σ is a free parameter. There is also a similar ambiguity due to the unknown thermalization time: if one lets the system evolve for some time t_0 before evaluating ε_n, the values of ε_n depend on t_0. If one doubles the value of σ, from 0.4 to 0.8 fm [20], ε_2 decreases by 6% and ε_3 decreases by 9% for central collision, but the ratios in Tables I and II only change by 2% and 1% respectively. This can be easily understood. It can be shown [84] that the smearing of the sources only affects the denominator of Eq. (1), while leaving the numerator unchanged: thus the only effect of source smearing is a small increase in the system size, resulting in smaller ε_n. Since $\{r^3\} \propto \{r^2\}^{2/3}$, ε_n decreases in such a way that the ratio $\varepsilon_2/(\varepsilon_3)^{2/3}$ remains constant. Comparing with Eq. (5), where k is close to $2/3$, one sees that smearing results in a displacement of $(\varepsilon_2,\varepsilon_3)$ almost parallel to the allowed band; more or less smearing does not yield better or worse agreement with data.

V. CONCLUSIONS

Elliptic and triangular flow, v_2 and v_3, are determined by the ellipticity ε_2 and triangularity ε_3 of the initial density profile, and by the linear hydrodynamic response to these initial anisotropies. Experimental data on v_2 and v_3 thus allow to constrain the rms ε_2 and ε_3. By varying unknown parameters in the hydrodynamic calculations, we have obtained the corresponding uncertainties on the rms ε_2 and ε_3 at RHIC and LHC energies. They are strongly correlated, so that region allowed by data reduces in practice to a band in the (rms ε_2,rms ε_3) plane. We have described a simple test that can be performed on any candidate model of initial conditions to determine its compatibility with data.

While the main source of uncertainty in the hydrodynamic response is the viscosity over entropy ratio η/s, the uncertainty on the early stages is also significant. Both are correlated, in the sense that more initial flow can be compensated by a larger viscosity. For this reason, it is easier to constrain models of initial conditions than η/s.

We have shown that elliptic and triangular flow data can be used to exclude existing models of initial conditions. However, it is very difficult to constrain the granularity [85] of initial conditions from these data. As exemplified by Monte Carlo Glauber simulations, changing the source size has a modest effect on ε_2 and ε_3. In addition, the resulting change has almost exactly the same effect as changing the viscosity, which is unknown. Therefore it is unlikely that the granularity can be constrained with just elliptic and triangular flow data as long as η/s is not precisely known. Other data can be used for this purpose, such as the detailed structure of two-particle correlations [14].

The width of our error band is mostly due to the error on the linear response approximation itself, with the set of initial conditions that we have tested. Note that the deformation that we introduce to generate triangular flow, Eq. (4), is singular at the origin. With realistic initial conditions, one usually observes a stronger linear correlation between v_2 (v_3) and ε_2 (ε_3) than with our smooth initial conditions [19]. Repeating the calculation with realistic initial conditions could thus help reduce the width of the error band and yield tighter constraints on initial-state models.

ACKNOWLEDGMENTS

We thank the ALICE Collaboration for providing experimental data, and Jürgen Schukraft for helpful discussion. We also thank Christoffer Flensburg and Björn Schenke, for providing results from the DIPSY and IP-Glasma models. This work is funded by the European Research Council under the Advanced Investigator Grant ERC-AD-267258.

---

[1] S. A. Voloshin, A. M. Poskanzer, and R. Snellings, arXiv:0809.2949.

[2] D. Teaney and L. Yan, Phys. Rev. C **83**, 064904 (2011).

[3] K. H. Ackermann *et al.* (STAR Collaboration), Phys. Rev. Lett. **86**, 402 (2001).

[4] K. Aamodt *et al.* (ALICE Collaboration), Phys. Rev. Lett. **105**, 252302 (2010).

[5] J.-Y. Ollitrault, Phys. Rev. D **46**, 229 (1992).

[6] B. Alver and G. Roland, Phys. Rev. C **81**, 054905 (2010); **82**, 039903(E) (2010).

[7] P. K. Kovtun, D. T. Son, and A. O. Starinets, Phys. Rev. Lett. **94**, 111601 (2005).

[8] M. Luzum and P. Romatschke, Phys. Rev. C **78**, 034915 (2008); , **79**, 039903(E) (2009).

[9] B. H. Alver, C. Gombeaud, M. Luzum, and J.-Y. Ollitrault, Phys. Rev. C **82**, 034913 (2010).

[10] A. Adare *et al.* (PHENIX Collaboration), Phys. Rev. Lett. **107**, 252301 (2011).

[11] K. Aamodt *et al.* (ALICE Collaboration), Phys. Rev. Lett. **107**, 032301 (2011).

[12] N. Borghini, P. M. Dinh, and J.-Y. Ollitrault, Phys. Rev. C **63**, 054906 (2001).

[13] R. P. G. Andrade, F. Grassi, Y. Hama, T. Kodama, and W. L. Qian, Phys. Rev. Lett. **101**, 112301 (2008).

[14] F. G. Gardim, F. Grassi, M. Luzum, and J.-Y. Ollitrault, Phys. Rev. C **87**, 031901 (2013).

[15] N. Borghini and J.-Y. Ollitrault, Phys. Lett. B **642**, 227 (2006).

[16] P. Bozek, Phys. Rev. C **81**, 034909 (2010).

[17] U. W. Heinz and R. Snellings, Annu. Rev. Nucl. Part. Sci. **63**, 123 (2013).

[18] G. Aad *et al.* (ATLAS Collaboration), Phys. Rev. C **86**, 014907 (2012).

[19] H. Niemi, G. S. Denicol, H. Holopainen, and P. Huovinen, Phys. Rev. C **87**, 054901 (2013).

[20] H. Holopainen, H. Niemi, and K. J. Eskola, Phys. Rev. C **83**, 034901 (2011).

[21] B. Alver *et al.* (PHOBOS Collaboration), Phys. Rev. Lett. **98**, 242302 (2007).

[22] H. Petersen, G.-Y. Qin, S. A. Bass, and B. Muller, Phys. Rev. C **82**, 041901 (2010).

[23] R. S. Bhalerao, M. Luzum, and J.-Y. Ollitrault, Phys. Rev. C **84**, 034910 (2011).

[24] F. G. Gardim, F. Grassi, Y. Hama, M. Luzum, and J.-Y. Ollitrault, Phys. Rev. C **83**, 064901 (2011).

[25] E. Retinskaya, M. Luzum, and J.-Y. Ollitrault, Phys. Rev. Lett. **108**, 252302 (2012).

[26] F. G. Gardim, F. Grassi, M. Luzum, and J.-Y. Ollitrault, Phys. Rev. C **85**, 024908 (2012).

[27] D. Teaney and L. Yan, Phys. Rev. C **86**, 044908 (2012).

[28] D. Teaney and L. Yan, Nucl. Phys. A **904-905**, 365c (2013).

[29] M. Miller and R. Snellings, arXiv:nucl-ex/0312008.

[30] B. Alver, B. B. Back, M. D. Baker, M. Ballintijn, D. S. Barton, R. R. Betts, R. Bindel, W. Busza *et al.*, Phys. Rev. C **77**, 014906 (2008).

[31] S. Afanasiev *et al.* (PHENIX Collaboration), Phys. Rev. C **80**, 024909 (2009).

[32] C. Gale, S. Jeon, and B. Schenke, Int. J. Mod. Phys. A **28**, 1340011 (2013).

[33] M. Luzum and J.-Y. Ollitrault, Nucl. Phys. A **904-905**, 377c (2013).

[34] R. A. Soltz, I. Garishvili, M. Cheng, B. Abelev, A. Glenn, J. Newby, L. A. Linden Levy, and S. Pratt, Phys. Rev. C **87**, 044901 (2013).

[35] J. D. Bjorken, Phys. Rev. D **27**, 140 (1983).

[36] S. Chatrchyan *et al.* (CMS Collaboration), Eur. Phys. J. C **72**, 2012 (2012).

[37] L. Adamczyk *et al.* (STAR Collaboration), Phys. Rev. C **88**, 014904 (2013).

[38] M. Luzum and P. Romatschke, Phys. Rev. Lett. **103**, 262302 (2009).

[39] M. Luzum, Phys. Rev. C **83**, 044911 (2011).

[40] Z. Qiu and U. W. Heinz, Phys. Rev. C **84**, 024911 (2011).

[41] T. Epelbaum and F. Gelis, Phys. Rev. Lett. **111**, 232301 (2013).

[42] P. F. Kolb and U. W. Heinz, in *Quark-Gluon Plasma 3*, edited by R. C. Hwa and X.-N. Wang (World Scientific, Singapore, 2004), pp. 634–714.

[43] M. Gyulassy, Y. M. Sinyukov, I. Karpenko, and A. V. Nazarenko, Braz. J. Phys. **37**, 1031 (2007).

[44] W. Broniowski, M. Chojnacki, W. Florkowski, and A. Kisiel, Phys. Rev. Lett. **101**, 022301 (2008).

[45] S. Pratt, Phys. Rev. Lett. **102**, 232301 (2009).

[46] J. Vredevoogd and S. Pratt, Phys. Rev. C **79**, 044915 (2009).

[47] J.-Y. Ollitrault, Eur. J. Phys. **29**, 275 (2008).

[48] H. B. Meyer, Phys. Rev. D **76**, 101701 (2007).

[49] H. Song, Nucl. Phys. A **904-905**, 114c (2013).

[50] K. Dusling and D. Teaney, Phys. Rev. C **77**, 034905 (2008).

[51] G. S. Denicol, T. Kodama, T. Koide, and P. Mota, Phys. Rev. C **80**, 064901 (2009).

[52] K. Dusling and T. Schäfer, Phys. Rev. C **85**, 044909 (2012).

[53] F. Karsch, D. Kharzeev, and K. Tuchin, Phys. Lett. B **663**, 217 (2008).

[54] R. Baier, P. Romatschke, D. T. Son, A. O. Starinets, and M. A. Stephanov, J. High Energy Phys. 04 (2008) 100.

[55] D. Teaney, J. Lauret, and E. V. Shuryak, Phys. Rev. Lett. **86**, 4783 (2001).

[56] T. Hirano, U. W. Heinz, D. Kharzeev, R. Lacey, and Y. Nara, Phys. Lett. B **636**, 299 (2006).

[57] H. Song, S. A. Bass, and U. Heinz, Phys. Rev. C **83**, 054912 (2011); **87**, 019902(E) (2013).

[58] T. Hirano, P. Huovinen, K. Murase, and Y. Nara, Prog. Part. Nucl. Phys. **70**, 108 (2013).

[59] S. Ryu, S. Jeon, C. Gale, B. Schenke, and C. Young, Nucl. Phys. A **904-905**, 389c (2013).

[60] A. Monnai and T. Hirano, Phys. Rev. C **80**, 054906 (2009).

[61] P. Bozek and I. Wyskiel-Piekarska, Phys. Rev. C **85**, 064915 (2012).

[62] D. Teaney, Phys. Rev. C **68**, 034913 (2003).

[63] D. Teaney and L. Yan, arXiv:1304.3753.

[64] K. Dusling, G. D. Moore, and D. Teaney, Phys. Rev. C **81**, 034907 (2010).

[65] M. Luzum and J.-Y. Ollitrault, Phys. Rev. C **82**, 014906 (2010).

[66] P. F. Kolb, Heavy Ion Phys. **15**, 279 (2002).

[67] M. Luzum, Phys. Lett. B **696**, 499 (2011).

[68] H. Niemi, G. S. Denicol, P. Huovinen, E. Molnar, and D. H. Rischke, Phys. Rev. C **86**, 014909 (2012).

[69] M. L. Miller, K. Reygers, S. J. Sanders, and P. Steinberg, Annu. Rev. Nucl. Part. Sci. **57**, 205 (2007).

[70] B. Schenke, S. Jeon, and C. Gale, Phys. Rev. Lett. **106**, 042301 (2011).

[71] P. Bozek and W. Broniowski, Phys. Lett. B **718**, 1557 (2013).

[72] B. Alver, M. Baker, C. Loizides, and P. Steinberg, arXiv:0805.4411.

[73] W. Broniowski, M. Rybczynski, and P. Bozek, Comput. Phys. Commun. **180**, 69 (2009).

[74] M. Rybczynski, G. Stefanek, W. Broniowski, and P. Bozek, arXiv:1310.5475.

[75] S. S. Adler *et al.* (PHENIX Collaboration), Phys. Rev. C **71**, 034908 (2005); **71**, 049901(E) (2005).

[76] B. Abelev *et al.* (ALICE Collaboration), Phys. Rev. C **88**, 044909 (2013).

[77] D. Kharzeev and M. Nardi, Phys. Lett. B **507**, 121 (2001).

[78] T. Lappi and R. Venugopalan, Phys. Rev. C **74**, 054905 (2006).

[79] H.-J. Drescher and Y. Nara, Phys. Rev. C **76**, 041903 (2007).

[80] J. L. Albacete and A. Dumitru, arXiv:1011.5161.

[81] C. Flensburg, arXiv:1108.4862.

[82] A. Dumitru and Y. Nara, Phys. Rev. C **85**, 034907 (2012).

[83] B. Schenke, P. Tribedy, and R. Venugopalan, Phys. Rev. C **86**, 034908 (2012).

[84] R. S. Bhalerao, M. Luzum, and J.-Y. Ollitrault, Phys. Rev. C **84**, 054901 (2011).

[85] H. Petersen, C. Coleman-Smith, S. A. Bass, and R. Wolpert, J. Phys. G **38**, 045102 (2011).

Constraining models of initial state with v_2 and v_3 data from LHC and RHIC

Ekaterina Retinskaya[a,*], Matthew Luzum[b,c], Jean-Yves Ollitrault[d]

[a] *CEA, IPhT, Institut de physique théorique de Saclay, F-91191 Gif-sur-Yvette, France*
[b] *McGill University, 3600 University Street, Montreal QC H3A 2TS, Canada*
[c] *Lawrence Berkeley National Laboratory, Berkeley, CA 94720, USA*
[d] *CNRS, URA2306, IPhT, Institut de physique théorique de Saclay, F-91191 Gif-sur-Yvette, France*

Abstract

We present a combined analysis of elliptic and triangular flow data from LHC and RHIC using viscous relativistic hydrodynamics. Elliptic flow v_2 in hydrodynamics is proportional to the participant eccentricity ε_2 and triangular flow is proportional to the participant triangularity ε_3, which means $v_n = \kappa_n \varepsilon_n$, where κ_n is the linear response coefficient in harmonic n. Experimental data for v_2 and v_3 combined with hydrodynamic calculations of κ_n thus provide us with the rms values of initial anisotropies ε_2 and ε_3. By varying free parameters in the hydro calculation (in particular the shear viscosity), we obtain an allowed band in the (rms ε_2, rms ε_3) plane. Comparison with Monte-Carlo models of the initial state allows us to exclude several of these models. We illustrate that the effect of changing the granularity of the initial state is similar to changing the medium properties, making these effects difficult to disentangle.

---

1. Introduction

One of the most important topics of study in heavy-ion collisions is the observation of particle momentum anisotropy in directions transverse to the beam [1], which can provide the evidence for the formation of some strongly interacting medium, which thermalizes and expands as a liquid, which we call the quark-gluon plasma (QGP). The corresponding experimental observables are the flow coefficients v_1, v_2, v_3 etc. In these proceedings we will concentrate on v_2 and v_3 (elliptic [3, 4] and triangular) flow coefficients. While elliptic flow, v_2, is a response of the system to an initial distribution with the form of ellipse in the transverse plane [5], the triangular flow, v_3, is understood as the response of triangular deformation, which is caused by fluctuations of initial geometry [6].

In spite of the fact that v_2 and v_3 are the most studied harmonics of anisotropic flow, there are still a number of open questions. Different models of initial states give different values when trying to extract transport coefficients from data. For instance by tuning η/s (viscosity over entropy [7]) one can match the experimental data with one model or another [8]. And it was found out that although one could fit both v_2 and v_3 data separately by tuning η/s with hydro

---

[*] Corresponding author

Email addresses: `ekaterina.retinskaya@cea.fr` (Ekaterina Retinskaya), `MWLuzum@lbl.gov` (Matthew Luzum), `jean-yves.ollitrault@cea.fr` (Jean-Yves Ollitrault)

calculation, some of the models of initial state were unable to fit simultaneously v_2 and v_3 [9, 11]. This hints, that by combining v_2 and v_3 data we can constrain models of initial state even though the viscosity is unknown.

2. Monte Carlo models of initial state

By initial conditions, we mean the initial energy-density profile at thermalization time t_0 [32]. This profile is not smooth and has fluctuations from wave-functions of incoming nuclei. The magnitude of these fluctuations is still to a large extent unconstrained from data. Another open question pertaining to initial state is how elongated is the ellipse of the overlap area in non-central collisions. We will address these issues and test different Monte Carlo models of initial state. We are testing two types of models: Glauber-type models and QCD-inspired models. The Monte Carlo Glauber model is the oldest and the most classic one [14]. We use the PHOBOS Monte Carlo [15]. In this model positions of nucleons within a nuclei are sampled through Monte Carlo. These nucleons move on straight lines and interact if their distance is less then $\sqrt{\sigma_{NN}/\pi}$. Typically one then models each nucleon as a Gaussian source, so that the final energy-density is equal to a sum of Gaussians.

Among the QCD-inspired models we are going to test 4 of them: the oldest QCD model which we call MC-KLN [16, 17], which is using k_T factorization and taking into account fluctuations of the positions of the nucleons. The second model MCrcBK [19] is an improved MC-KLN model with additional KNO fluctuations in order to match multiplicity distribution in pp collisions. The third one is DIPSY [18], a QCD model which takes into account the multiple gluon cascade. And the last one is the IP Glasma model [20], which doesn't assume k_T factorization and includes non-linearities and fluctuations of color charges within a nucleon.

3. Hydro evolution

In spite of the fact that collaborations have published data for integrated v_n[13] for n=1, 2, ... 6 [21], here we only use elliptic and triangular flow. The main reason is that these two Fourier coefficients are determined by simple linear response to the initial state [22]. That means: $v_2 \propto \varepsilon_2$ [23], where ε_2 is called participant ellipticity [24] and $v_3 \propto \varepsilon_3$ [25], ε_3 is called participant triangularity [6]. The participant eccentricity ε_n for a single event is defined as [2, 26]:

$$\varepsilon_n = \frac{|\{r^n e^{in\phi}\}|}{\{r^n\}}, \tag{1}$$

where {...} denotes an average value over the initial energy density (it can also be entropy density profile though) after recentering the coordinate system $\{re^{i\phi}\} = 0$.

Assuming linear response to the initial anisotropy, the anisotropic flow in an event is $v_n = \kappa_n \varepsilon_n$. The response coefficient κ_n is the same for all events in a centrality bin, but ε_n fluctuates, so that initial-state fluctuations result in event-by-event flow fluctuations. Experiments measure the rms value of v_n over a centrality bin, thus the experimentally measured flow v_n is proportional to the rms value of ε_n. We can therefore write:

$$\sqrt{\langle \varepsilon_n^2 \rangle} = \frac{\sqrt{\langle (v_n)^2 \rangle}}{\kappa_n}, \tag{2}$$

where $\sqrt{\langle (v_n)^2 \rangle}$ is the measured root mean square value of integrated flow and $\langle ... \rangle$ represents an average over collision events. The response coefficient κ_n is calculated in hydrodynamics as $\kappa_n = (v_n/\varepsilon_n)_{hydro}$, so that we are able to extract the root mean square values of ε_2 and ε_3. We take experimental data of integrated flow from the ALICE and PHENIX collaborations [11, 12].

4. Uncertainties in hydro response

The standard hydro modeling [27] procedure consist of 3 main steps:
1) initial conditions
2) evolve these initial conditions through relativistic hydro evolution
3) convert the liquid into hadrons at freeze-out temperature.

Each of these steps obviously has its uncertainties [28]. The main uncertainty in the hydro evolution is the value of the shear viscosity of the strongly-interacting quark-gluon plasma. This value is not constrained well in theory and experiment[36, 37], so we vary η/s as a parameter from 0 to 0.24 in steps of 0.04. The value of the shear viscosity has a remarkable influence on the values of integrated flow: the flow decreases with increasing viscosity. Another big source of uncertainty is coming from initial conditions. Our hydro calculations are 2+1D viscous hydrodynamic, which uses as input initial condition the transverse energy density profile from an optical Glauber model. This profile is smooth and already has an ellipticity, so automatically gives us elliptic flow values. If we want to obtain the values of ε_3 or v_3, with this profile we get 0 for both of them, so in order to calculate κ_3 we deform the third harmonic in the profile in the following way [9] :

$$\epsilon(r, \phi) \to (r\sqrt{1 + \varepsilon'_n \cos(n(\phi - \psi_n))}, \phi) \tag{3}$$

where ε'_n is magnitude of the deformation, and ψ_n is the orientation of the deformation.

First, the linear approximation itself has an associated uncertainty, and the value of κ_n obtained from a smooth initial condition can differ from that extracted from a set of flucuating events [10]. We estimate this uncertainty by using values obtained from two definitions of ε_n: with energy density weighting and entropy density weighting.

Another free parameter is the thermalization time t_0[32, 33] which is not known. We vary it from 0.5 fm/c to 1fm/c. While we vary the thermalization time we tune the starting temperature T_{start} and the freeze-out temperature T_{fr} so as to match the p_t spectrum [30, 31].

In the hadronic part we also have some uncertainty, which is coming from the freezeout viscous correction, the momentum dependence of which is unknown[38, 39, 40], so we test 2 possible ansatzs: linear $\propto p$[41] and quadratic $\propto p^2$[38]. We use the same code as in Ref.[38] and we take into account resonance decays after hadronization.

After taking into account all types of uncertainties we can calculate ε_2 and ε_3 using Eq. (2). The resulting values are shown in the Fig. 1 for the 20–30% centrality range at the LHC.

Each point in this figure corresponds to one hydro calculation with one set of parameters. We have 6 types of symbols, corresponding different sets of parameters: thermalization time t_0, the type of ansatz and the type of ε_n weighting. These symbols are composing 6 lines with viscosity η/s changing. Each line has 7 points, corresponding to η/s = 0, 0.04, 0.08, 0.12, 0.16, 0.2, 0.24 (from left to right). The first line, composed of blue circles, uses as parameters the thermalization time 1fm/c and the linear ansatz. The line with purple squares uses thermalization time 1fm/c and quadratic ansatz. We see the line almost doesn't change, except for high viscosity, which makes values of ε_2 slightly smaller. The line composed of yellow diamonds corresponds

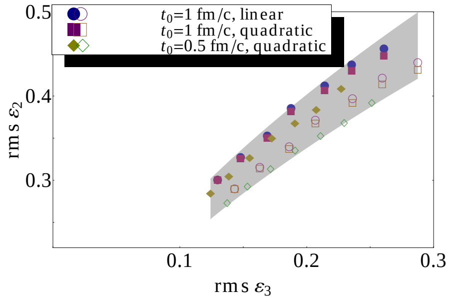

Figure 1: (Color online) R.m.s. values of $\varepsilon_2(\varepsilon_3)$ from hydro simulations + ALICE data for 20–30% centrality range. Purple squares correspond to $t_{init} = 1 fm/c$ with quadratic freezeout. Blue circles correspond to $t_{init} = 1 fm/c$ with linear freezeout. Yellow diamonds correspond to $t_{init} = 0.5 fm/c$ with quadratic freezeout. Open symbols mean entropy-density profile used. The shaded band is an allowed band encompassing uncertainty in the extracted values.

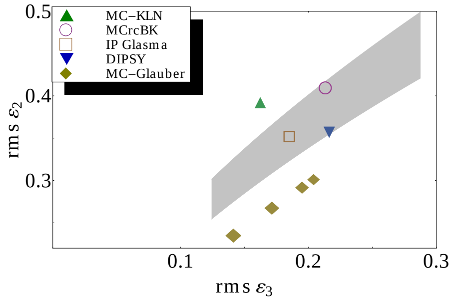

Figure 2: (Color online) The shaded band is the same as in Fig.1 and represents allowed values. Symbols are predictions from various models of initial state. The MC-Glauber model is shown for different values of the width of gaussian σ=0 fm, 0.4 fm, 0.8 fm and 1.2 fm, which are distinguished by different symbol sizes, showing that changing the smearing parameter has the same effect as changing viscosity.

to thermalization time 0.5 fm/c and quadratic ansatz. We see that ε_2 and ε_3 are both decreasing. The explanation is that since we start the hydro evolution earlier, we produce more flow, and from the ratio (2) obviously if we produce more flow, we will have smaller values of ε_2 and ε_3. Lines composed of open symbols have the same parameters, except that entropy-density weighting is used. Now we create a shaded band, such that all these points are inside this band. This band defines the allowed range. The important fact here is that even with all uncertainties taken into account, we obtain a narrow band, which eventually allows us to constrain models. These lines are noticed to be well fitted by the law $\sqrt{\langle\varepsilon_2^2\rangle}/\left(\sqrt{\langle\varepsilon_3^2\rangle}\right)^k = C$, where k=0.6 for LHC and k=0.5 for RHIC and C is fixed. By computing the maximum and minimum values of C allowed by hydrodynamics, we determine the range of allowed values for C.

By computing the values of C in various Monte Carlo models, one can check if the values predicted by models are inside the allowed region, as shown in Fig. 3. In this way the formula can be used easily by any group who has an MC model of initial states in order to see if their model is compatible with experimental data.

5. Results

We calculate the allowed region in the (rms ε_2, rms ε_3) plane for different centralities for LHC and RHIC, which we represent as a shaded band. After this we test the models, introduced in Section 2.

In Fig. 2 we display as an example the 20–30% centrality range. The MC-Glauber model is shown for different values of the width of gaussian σ=0 fm, 0.4 fm, 0.8 fm and 1.2 fm, which are distinguished by different symbol sizes. By changing this parameter the result moves parallel to the band, which has the same effect as changing the viscosity, so that compatibility with data cannot be improved by adjusting the unknown source size.

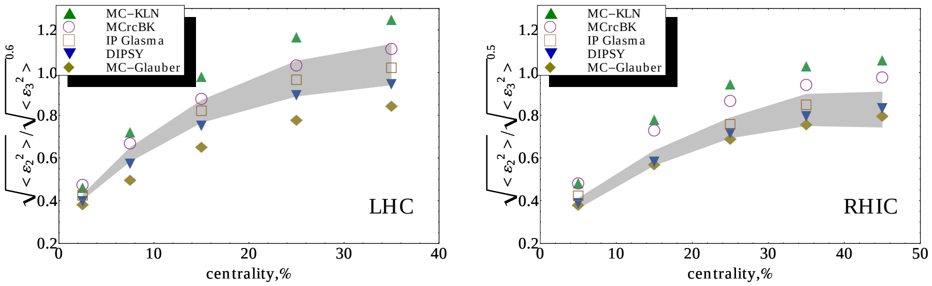

Figure 3: (Color online) Ratio of eccentricity moments $\sqrt{\langle\varepsilon_2^2\rangle}/\left(\sqrt{\langle\varepsilon_3^2\rangle}\right)^k$ versus centrality. Shaded bands are allowed by experiment values, combined with hydrodynamic calculations, for LHC and RHIC. Symbols are predictions from various models of initial state.

Our main results are presented in Fig. 3. It displays the rms values of $\sqrt{\langle\varepsilon_2^2\rangle}/\left(\sqrt{\langle\varepsilon_3^2\rangle}\right)^k$ versus centrality, where shaded bands are allowed values and symbols are predictions from different models. We can see that one can exclude the PHOBOS MC-Glauber (as was also noticed for 20–30% centrality) and MC-KLN models for LHC energies. It seems MC Glauber works better for lower energies, and MC-KLN doesn't have enough fluctuations. For RHIC energies MC-KLN can also be excluded, along with the MCrcBK model, which seems to works better at LHC energies. Note that we have not tested all possible variants of Glauber-type models. In particular, the PHOBOS MC-Glauber has only fluctuations from the random positions of nucleons in the nucleus, and neglects any extra local fluctuations in entropy production.

From the Fig.2 in our paper [42] we've seen that rms ε_2 and ε_3 values predicted by MC models both increase with centrality, but we noticed that ε_2 values are increasing faster then ε_3, which can be explained by the fact, that v_2 is growing faster with centrality then v_3: v_2 grows due to geometry, and v_3 due to the fact that fluctuations have more influence with increasing centrality, but this effect is weaker. By looking at the ε_3 values of MC models we can see which of the models have more fluctuations, for example by comparing MC-KLN and MCrcBK, obviously, the second has more fluctuations, as the result it has bigger value of ε_3. The same about DIPSY which seems to have big value of fluctuations.

Conclusions

We have extracted ellipticity ε_2 and triangularity ε_3, using experimental data and hydro calculations with different sources of uncertainties and created a narrow allowed region on the (rms ε_3, rms ε_2) plane. We have shown that we are able to constrain models of initial state. It was shown that we can exclude PHOBOS MC-Glauber and MC-KLN models for LHC and MC-KLN and MCrcBK models for RHIC. We have illustrated for the MC-Glauber model that changing the granularity of the initial condition model has the same effect as changing viscosity, so the effects are difficult to disentangle.

More details about this study can be found in our recently published paper [42].

[1] S. A. Voloshin, A. M. Poskanzer and R. Snellings, arXiv:0809.2949 [nucl-ex].
[2] D. Teaney and L. Yan, Phys. Rev. C **83**, 064904 (2011) [arXiv:1010.1876 [nucl-th]].

[3] K. H. Ackermann *et al.* [STAR Collaboration], Phys. Rev. Lett. **86**, 402 (2001) [nucl-ex/0009011].
[4] K. Aamodt *et al.* [ALICE Collaboration], Phys. Rev. Lett. **105**, 252302 (2010) [arXiv:1011.3914 [nucl-ex]].
[5] J. -Y. Ollitrault, Phys. Rev. D **46**, 229 (1992).
[6] B. Alver and G. Roland, Phys. Rev. C **81**, 054905 (2010) [Erratum-ibid. C **82**, 039903 (2010)] [arXiv:1003.0194 [nucl-th]].
[7] P. Kovtun, D. T. Son and A. O. Starinets, Phys. Rev. Lett. **94**, 111601 (2005) [hep-th/0405231].
[8] M. Luzum and P. Romatschke, Phys. Rev. C **78**, 034915 (2008) [Erratum-ibid. C **79**, 039903 (2009)] [arXiv:0804.4015 [nucl-th]].
[9] B. H. Alver, C. Gombeaud, M. Luzum and J. -Y. Ollitrault, Phys. Rev. C **82**, 034913 (2010) [arXiv:1007.5469 [nucl-th]].
[10] Z. Qiu and U. W. Heinz, Phys. Rev. C **84**, 024911 (2011) [arXiv:1104.0650 [nucl-th]].
[11] A. Adare *et al.* [PHENIX Collaboration], Phys. Rev. Lett. **107**, 252301 (2011) [arXiv:1105.3928 [nucl-ex]].
[12] K. Aamodt *et al.* [ALICE Collaboration], Phys. Rev. Lett. **107**, 032301 (2011) [arXiv:1105.3865 [nucl-ex]].
[13] N. Borghini, P. M. Dinh and J. -Y. Ollitrault, Phys. Rev. C **63**, 054906 (2001) [nucl-th/0007063].
[14] M. L. Miller, K. Reygers, S. J. Sanders and P. Steinberg, Ann. Rev. Nucl. Part. Sci. **57**, 205 (2007) [nucl-ex/0701025].
[15] B. Alver, M. Baker, C. Loizides and P. Steinberg, arXiv:0805.4411 [nucl-ex].
[16] H. -J. Drescher and Y. Nara, Phys. Rev. C **76**, 041903 (2007) [arXiv:0707.0249 [nucl-th]].
[17] J. L. Albacete and A. Dumitru, arXiv:1011.5161 [hep-ph].
[18] C. Flensburg, arXiv:1108.4862 [nucl-th].
[19] A. Dumitru and Y. Nara, Phys. Rev. C **85**, 034907 (2012) [arXiv:1201.6382 [nucl-th]].
[20] B. Schenke, P. Tribedy and R. Venugopalan, Phys. Rev. C **86**, 034908 (2012) [arXiv:1206.6805 [hep-ph]].
[21] G. Aad *et al.* [ATLAS Collaboration], Phys. Rev. C **86**, 014907 (2012) [arXiv:1203.3087 [hep-ex]].
[22] H. Niemi, G. S. Denicol, H. Holopainen and P. Huovinen, Phys. Rev. C **87**, 054901 (2013) [arXiv:1212.1008 [nucl-th]].
[23] H. Holopainen, H. Niemi and K. J. Eskola, Phys. Rev. C **83**, 034901 (2011) [arXiv:1007.0368 [hep-ph]].
[24] B. Alver *et al.* [PHOBOS Collaboration], Phys. Rev. Lett. **98**, 242302 (2007) [nucl-ex/0610037].
[25] H. Petersen, G. -Y. Qin, S. A. Bass and B. Muller, Phys. Rev. C **82**, 041901 (2010) [arXiv:1008.0625 [nucl-th]].
[26] R. S. Bhalerao, M. Luzum and J. -Y. Ollitrault, Phys. Rev. C **84**, 034910 (2011) [arXiv:1104.4740 [nucl-th]].
[27] C. Gale, S. Jeon and B. Schenke, Int. J. Mod. Phys. A **28**, 1340011 (2013).
[28] M. Luzum and J. -Y. Ollitrault, Nucl. Phys. A904-905 **2013**, 377c (2013) [arXiv:1210.6010 [nucl-th]].
[29] R. A. Soltz, I. Garishvili, M. Cheng, B. Abelev, A. Glenn, J. Newby, L. A. Linden Levy and S. Pratt, Phys. Rev. C **87**, 044901 (2013) [arXiv:1208.0897 [nucl-th]].
[30] L. Adamczyk *et al.* [STAR Collaboration], Phys. Rev. C 88, **014904** (2013) [arXiv:1301.2187 [nucl-ex]].
[31] M. Luzum and P. Romatschke, Phys. Rev. Lett. **103**, 262302 (2009) [arXiv:0901.4588 [nucl-th]].
[32] F. Gelis and T. Epelbaum, arXiv:1307.2214 [hep-ph].
[33] P. F. Kolb and U. W. Heinz, In *Hwa, R.C. (ed.) et al.: Quark gluon plasma* 634-714 [nucl-th/0305084].
[34] W. Broniowski, M. Chojnacki, W. Florkowski and A. Kisiel, Phys. Rev. Lett. **101**, 022301 (2008) [arXiv:0801.4361 [nucl-th]].
[35] S. Pratt, Phys. Rev. Lett. **102**, 232301 (2009) [arXiv:0811.3363 [nucl-th]].
[36] H. B. Meyer, Phys. Rev. D **76**, 101701 (2007) [arXiv:0704.1801 [hep-lat]].
[37] H. Song, Nucl. Phys. A904-905 **2013**, 114c (2013) [arXiv:1210.5778 [nucl-th]].
[38] D. Teaney, Phys. Rev. C **68**, 034913 (2003) [nucl-th/0301099].
[39] D. Teaney and L. Yan, arXiv:1304.3753 [nucl-th].
[40] K. Dusling, G. D. Moore and D. Teaney, Phys. Rev. C **81**, 034907 (2010) [arXiv:0909.0754 [nucl-th]].
[41] M. Luzum and J. -Y. Ollitrault, Phys. Rev. C **82**, 014906 (2010) [arXiv:1004.2023 [nucl-th]].
[42] E. Retinskaya, M. Luzum and J. -Y. Ollitrault, Phys. Rev. C **89**, 014902 (2014) [arXiv:1311.5339 [nucl-th]].

References

[1] F.-H. Liu, D.-H. Zhang, and M.-Y. Duan, *Formulation of charged-particle pseudorapidity distribution in Au Au collisions at the maximum RHIC energy*, *Europhys.Lett.* **61** (2003) 736–741.

[2] J. Greensite, *The Confinement problem in lattice gauge theory*, *Prog.Part.Nucl.Phys.* **51** (2003) 1, [`hep-lat/0301023`].

[3] B. Mohanty, *Exploring the QCD phase diagram through high energy nuclear collisions: An overview*, *PoS* **CPOD2013** (2013) 001, [`arXiv:1308.3328`].

[4] P. Huovinen and P. Petreczky, *QCD Equation of State and Hadron Resonance Gas*, *Nucl.Phys.* **A837** (2010) 26–53, [`arXiv:0912.2541`].

[5] S. Borsanyi, G. Endrodi, Z. Fodor, A. Jakovac, S. D. Katz, *et. al.*, *The QCD equation of state with dynamical quarks*, *JHEP* **1011** (2010) 077, [`arXiv:1007.2580`].

[6] J. Brachmann, S. Soff, A. Dumitru, H. Stoecker, J. Maruhn, *et. al.*, *Antiflow of nucleons at the softest point of the EoS*, *Phys.Rev.* **C61** (2000) 024909, [`nucl-th/9908010`].

[7] **STAR Collaboration** Collaboration, B. Abelev *et. al.*, *System-size independence of directed flow at the Relativistic Heavy-Ion Collider*, *Phys.Rev.Lett.* **101** (2008) 252301, [`arXiv:0807.1518`].

[8] **ALICE Collaboration** Collaboration, B. Abelev *et. al.*, *Directed flow of charged particles at midrapidity relative to the spectator plane in Pb-Pb collisions at $\sqrt{s_{NN}}$=2.76 TeV*, *Phys.Rev.Lett.* **111** (2013) 232302, [`arXiv:1306.4145`].

[9] C. Nonaka and M. Asakawa, *Modeling a Realistic Dynamical Model for High Energy Heavy Ion Collisions*, *PTEP* **2012** (2012) 01A208, [`arXiv:1204.4795`].

[10] **ALICE Collaboration** Collaboration, K. Aamodt *et. al.*, *Higher harmonic anisotropic flow measurements of charged particles in Pb-Pb collisions at $\sqrt{s_{NN}}$=2.76 TeV*, *Phys.Rev.Lett.* **107** (2011) 032301, [`arXiv:1105.3865`].

[11] **PHOBOS Collaboration** Collaboration, B. Alver *et. al.*, *System size*

dependence of two-particle angular correlations in p + p, Cu + Cu and Au + Au collisions, *J.Phys.* **G35** (2008) 104142, [`arXiv:0804.2471`].

[12] B. Schenke, P. Tribedy, and R. Venugopalan, *Fluctuating Glasma initial conditions and flow in heavy ion collisions*, *Phys.Rev.Lett.* **108** (2012) 252301, [`arXiv:1202.6646`].

[13] B. Schenke, S. Jeon, and C. Gale, *Higher flow harmonics from (3+1)D event-by-event viscous hydrodynamics*, *Phys.Rev.* **C85** (2012) 024901, [`arXiv:1109.6289`].

[14] **ALICE Collaboration** Collaboration, K. Aamodt *et. al.*, *Harmonic decomposition of two-particle angular correlations in Pb-Pb collisions at $\sqrt{s_{NN}} = 2.76$ TeV*, *Phys.Lett.* **B708** (2012) 249–264, [`arXiv:1109.2501`].

[15] **ALICE Collaboration** Collaboration, R. Preghenella, *Identified-particle production and spectra with the ALICE detector in pp and Pb-Pb collisions at the LHC*, *Acta Phys.Polon.* **B43** (2012) 555, [`arXiv:1111.7080`].

[16] **ATLAS Collaboration** Collaboration, G. Aad *et. al.*, *Measurement of the azimuthal anisotropy for charged particle production in $\sqrt{s_{NN}} = 2.76$ TeV lead-lead collisions with the ATLAS detector*, *Phys.Rev.* **C86** (2012) 014907, [`arXiv:1203.3087`].

[17] **STAR** Collaboration, Y. Pandit, *Dipole asymmetry at $\sqrt{s_{NN}} = 200$ GeV Au+Au Collisions from STAR experiment at RHIC*, *J.Phys.Conf.Ser.* **446** (2013) 012012, [`arXiv:1211.7162`].

[18] Z. Qiu and U. W. Heinz, *Event-by-event shape and flow fluctuations of relativistic heavy-ion collision fireballs*, *Phys.Rev.* **C84** (2011) 024911, [`arXiv:1104.0650`].

[19] **ATLAS Collaboration** Collaboration, J. Jia, *Measurement of Event Plane Correlations in Pb-Pb Collisions at $\sqrt{s_{\rm NN}}$=2.76 TeV with the ATLAS Detector*, *Nucl.Phys.* **A910-911** (2013) 276–280, [`arXiv:1208.1427`].

[20] R. S. Bhalerao, J.-Y. Ollitrault, and S. Pal, *Event-plane correlators*, *Phys.Rev.* **C88** (2013) 024909, [`arXiv:1307.0980`].

[21] **STAR Collaboration** Collaboration, J. Adams *et. al.*, *Experimental*

and theoretical challenges in the search for the quark gluon plasma: The STAR Collaboration's critical assessment of the evidence from RHIC collisions, *Nucl.Phys.* **A757** (2005) 102–183, [`nucl-ex/0501009`].

[22] **PHENIX Collaboration** Collaboration, K. Adcox *et. al.*, *Formation of dense partonic matter in relativistic nucleus-nucleus collisions at RHIC: Experimental evaluation by the PHENIX collaboration*, *Nucl.Phys.* **A757** (2005) 184–283, [`nucl-ex/0410003`].

[23] B. Back, M. Baker, M. Ballintijn, D. Barton, B. Becker, *et. al.*, *The PHOBOS perspective on discoveries at RHIC*, *Nucl.Phys.* **A757** (2005) 28–101, [`nucl-ex/0410022`].

[24] M. Gyulassy and L. McLerran, *New forms of QCD matter discovered at RHIC*, *Nucl.Phys.* **A750** (2005) 30–63, [`nucl-th/0405013`].

[25] E. V. Shuryak, *What RHIC experiments and theory tell us about properties of quark-gluon plasma?*, *Nucl.Phys.* **A750** (2005) 64–83, [`hep-ph/0405066`].

[26] **PHENIX** Collaboration, K. Dehmelt, *ePHENIX at eRHIC*, *PoS* **DIS2013** (2013) 266.

[27] **PHENIX Collaboration** Collaboration, J. Seele, *The sPHENIX forward upgrade (and ePHENIX)*, *Nucl.Phys.* **A904-905** (2013) 933c–936c.

[28] **PHENIX Collaboration** Collaboration, J. S. Haggerty, *The sPHENIX barrel upgrade: Jet physics and beyond*, *Nucl.Phys.* **A904-905** (2013) 925c–928c.

[29] M. A. Lamont, *The importance of e+A collisions at an Electron-Ion Collider*, *J.Phys.Conf.Ser.* **446** (2013) 012051.

[30] **PHENIX Collaboration** Collaboration, A. Bazilevsky, *ePHENIX for eRHIC.* 2012.

[31] **STAR Collaboration** Collaboration, M. A. Lamont, *The STAR experiment: The second decade and beyond.* 2012.

[32] **eRHIC Accelerator Design Collaboration** Collaboration, V. Ptitsyn, *Accelerator design of high luminosity electron-hadron collider eRHIC.* 2012.

[33] **ALICE Collaboration** Collaboration, K. Aamodt *et. al.*, *The ALICE experiment at the CERN LHC*, *JINST* **3** (2008) S08002.

[34] **CMS Collaboration** Collaboration, S. Chatrchyan *et. al.*, *The CMS experiment at the CERN LHC*, *JINST* **3** (2008) S08004.

[35] **ATLAS Collaboration** Collaboration, G. Aad *et. al.*, *The ATLAS Experiment at the CERN Large Hadron Collider*, *JINST* **3** (2008) S08003.

[36] **ALICE Collaboration** Collaboration, M. Wilde, *Measurement of Direct Photons in pp and Pb-Pb Collisions with ALICE*, *Nucl.Phys.* **A904-905** (2013) 573c–576c, [`arXiv:1210.5958`].

[37] W. Florkowski, *Phenomenology of Ultra-Relativistic Heavy-Ion Collisions*. 2010.

[38] S. A. Voloshin, A. M. Poskanzer, and R. Snellings, *Collective phenomena in non-central nuclear collisions*, `arXiv:0809.2949`.

[39] P. F. Kolb, *Hydrodynamic flow at RHIC*, *Heavy Ion Phys.* **15** (2002) 279–289, [`nucl-th/0104089`].

[40] P. Carruthers and M. Duong-Van, *New scaling law based on the hydrodynamical model of particle production*, *Phys.Lett.* **B41** (1972) 597–601.

[41] P. Carruthers and M. Doung-van, *Rapidity and angular distributions of charged secondaries according to the hydrodynamical model of particle production*, *Phys.Rev.* **D8** (1973) 859–874.

[42] **ALICE Collaboration** Collaboration, K. Aamodt *et. al.*, *Centrality dependence of the charged-particle multiplicity density at mid-rapidity in Pb-Pb collisions at $\sqrt{s_{NN}} = 2.76$ TeV*, *Phys.Rev.Lett.* **106** (2011) 032301, [`arXiv:1012.1657`].

[43] M. Luzum and P. Romatschke, *Conformal Relativistic Viscous Hydrodynamics: Applications to RHIC results at s(NN)**(1/2) = 200-GeV*, *Phys.Rev.* **C78** (2008) 034915, [`arXiv:0804.4015`].

[44] H. Song and U. W. Heinz, *Causal viscous hydrodynamics in 2+1 dimensions for relativistic heavy-ion collisions*, *Phys.Rev.* **C77** (2008) 064901, [`arXiv:0712.3715`].

[45] E. V. Shuryak, *Quark-Gluon Plasma and Hadronic Production of*

Leptons, Photons and Psions, *Phys.Lett.* **B78** (1978) 150.

[46] E. V. Shuryak, *Quantum Chromodynamics and the Theory of Superdense Matter*, *Phys.Rept.* **61** (1980) 71–158.

[47] M. Stephanov, *QCD phase diagram: An Overview*, *PoS* **LAT2006** (2006) 024, [`hep-lat/0701002`].

[48] M. G. Alford, A. Schmitt, K. Rajagopal, and T. Schoefer, *Color superconductivity in dense quark matter*, *Rev.Mod.Phys.* **80** (2008) 1455–1515, [`arXiv:0709.4635`].

[49] E. Shuryak, *Physics of Strongly coupled Quark-Gluon Plasma*, *Prog.Part.Nucl.Phys.* **62** (2009) 48–101, [`arXiv:0807.3033`].

[50] F. Karsch and E. Laermann, *Thermodynamics and in medium hadron properties from lattice QCD*, `hep-lat/0305025`.

[51] Y. Aoki, Z. Fodor, S. Katz, and K. Szabo, *The QCD transition temperature: Results with physical masses in the continuum limit*, *Phys.Lett.* **B643** (2006) 46–54, [`hep-lat/0609068`].

[52] Y. Aoki, G. Endrodi, Z. Fodor, S. Katz, and K. Szabo, *The Order of the quantum chromodynamics transition predicted by the standard model of particle physics*, *Nature* **443** (2006) 675–678, [`hep-lat/0611014`].

[53] M. Laine and Y. Schroder, *Quark mass thresholds in QCD thermodynamics*, *Phys.Rev.* **D73** (2006) 085009, [`hep-ph/0603048`].

[54] **BRAHMS Collaboration** Collaboration, I. Arsene *et. al.*, *Quark gluon plasma and color glass condensate at RHIC? The Perspective from the BRAHMS experiment*, *Nucl.Phys.* **A757** (2005) 1–27, [`nucl-ex/0410020`].

[55] J.-Y. Ollitrault, *Anisotropy as a signature of transverse collective flow*, *Phys.Rev.* **D46** (1992) 229–245.

[56] D. Teaney, J. Lauret, and E. V. Shuryak, *Flow at the SPS and RHIC as a quark gluon plasma signature*, *Phys.Rev.Lett.* **86** (2001) 4783–4786, [`nucl-th/0011058`].

[57] M. Luzum, *Flow fluctuations and long-range correlations: elliptic flow and beyond*, *J.Phys.* **G38** (2011) 124026, [`arXiv:1107.0592`].

[58] J.-Y. Ollitrault and F. G. Gardim, *Hydro overview*, *Nucl.Phys.A904-905*

2013 (2013) 75c–82c, [`arXiv:1210.8345`].

[59] I. Selyuzhenkov, *Charged particle directed flow in Pb-Pb collisions at $\sqrt{s_{NN}} = 2.76$ TeV measured with ALICE at the LHC*, *J.Phys.* **G38** (2011) 124167, [`arXiv:1106.5425`].

[60] D. Teaney and L. Yan, *Triangularity and Dipole Asymmetry in Heavy Ion Collisions*, *Phys.Rev.* **C83** (2011) 064904, [`arXiv:1010.1876`].

[61] F. G. Gardim, F. Grassi, Y. Hama, M. Luzum, and J.-Y. Ollitrault, *Directed flow at mid-rapidity in event-by-event hydrodynamics*, *Phys.Rev.* **C83** (2011) 064901, [`arXiv:1103.4605`].

[62] L. Csernai, V. Magas, H. Stocker, and D. Strottman, *Fluid Dynamical Prediction of Changed v1-flow at LHC*, *Phys.Rev.* **C84** (2011) 024914, [`arXiv:1101.3451`].

[63] J. Bleibel, G. Burau, and C. Fuchs, *Anisotropic flow in Pb+Pb collisions at LHC from the quark gluon string model with parton rearrangement*, *Phys.Lett.* **B659** (2008) 520–524, [`arXiv:0711.3366`].

[64] P. Bozek and I. Wyskiel, *Directed flow in ultrarelativistic heavy-ion collisions*, *Phys.Rev.* **C81** (2010) 054902, [`arXiv:1002.4999`].

[65] **STAR Collaboration** Collaboration, J. Adams *et. al.*, *Azimuthal anisotropy at RHIC: The First and fourth harmonics*, *Phys.Rev.Lett.* **92** (2004) 062301, [`nucl-ex/0310029`].

[66] **STAR Collaboration** Collaboration, J. Adams *et. al.*, *Azimuthal anisotropy in Au+Au collisions at s(NN)**(1/2) = 200-GeV*, *Phys.Rev.* **C72** (2005) 014904, [`nucl-ex/0409033`].

[67] **STAR Collaboration** Collaboration, J. Adams *et. al.*, *Directed flow in Au+Au collisions at s(NN)**(1/2) = 62-GeV*, *Phys.Rev.* **C73** (2006) 034903, [`nucl-ex/0510053`].

[68] **PHOBOS Collaboration** Collaboration, B. Back *et. al.*, *Energy dependence of directed flow over a wide range of pseudorapidity in Au + Au collisions at RHIC*, *Phys.Rev.Lett.* **97** (2006) 012301, [`nucl-ex/0511045`].

[69] **STAR Collaboration** Collaboration, G. Agakishiev *et. al.*, *Directed and elliptic flow of charged particles in Cu+Cu collisions at $\sqrt{s_{NN}} =$ 22.4 GeV*, *Phys.Rev.* **C85** (2012) 014901, [`arXiv:1109.5446`].

[70] **STAR Collaboration** Collaboration, L. Adamczyk *et. al.*, *Directed Flow of Identified Particles in Au + Au Collisions at* $\sqrt{s_N N} = 200$ *GeV at RHIC*, *Phys.Rev.Lett.* **108** (2012) 202301, [`arXiv:1112.3930`].

[71] **STAR Collaboration** Collaboration, Y. Pandit, *Directed flow of Identified Charged Particles from the RHIC Beam Energy Scan*, *Acta Phys.Polon.Supp.* **5** (2012) 439–444, [`arXiv:1112.0842`].

[72] **ALICE Collaboration** Collaboration, K. Aamodt *et. al.*, *Elliptic flow of charged particles in Pb-Pb collisions at 2.76 TeV*, *Phys.Rev.Lett.* **105** (2010) 252302, [`arXiv:1011.3914`].

[73] B. Alver and G. Roland, *Collision geometry fluctuations and triangular flow in heavy-ion collisions*, *Phys.Rev.* **C81** (2010) 054905, [`arXiv:1003.0194`].

[74] B. H. Alver, C. Gombeaud, M. Luzum, and J.-Y. Ollitrault, *Triangular flow in hydrodynamics and transport theory*, *Phys.Rev.* **C82** (2010) 034913, [`arXiv:1007.5469`].

[75] J.-Y. Ollitrault, *Phenomenology of the little bang*, *J.Phys.Conf.Ser.* **312** (2011) 012002, [`arXiv:1008.3323`].

[76] **STAR Collaboration** Collaboration, B. Abelev *et. al.*, *Long range rapidity correlations and jet production in high energy nuclear collisions*, *Phys.Rev.* **C80** (2009) 064912, [`arXiv:0909.0191`].

[77] **PHOBOS Collaboration** Collaboration, B. Alver *et. al.*, *High transverse momentum triggered correlations over a large pseudorapidity acceptance in Au+Au collisions at s(NN)**1/2 = 200 GeV*, *Phys.Rev.Lett.* **104** (2010) 062301, [`arXiv:0903.2811`].

[78] **PHENIX Collaboration** Collaboration, A. Adare *et. al.*, *Dihadron azimuthal correlations in Au+Au collisions at s(NN)**(1/2) = 200-GeV*, *Phys.Rev.* **C78** (2008) 014901, [`arXiv:0801.4545`].

[79] **PHENIX Collaboration** Collaboration, S. Adler *et. al.*, *Dense-Medium Modifications to Jet-Induced Hadron Pair Distributions in Au+Au Collisions at s(NN)**(1/2) = 200-GeV*, *Phys.Rev.Lett.* **97** (2006) 052301, [`nucl-ex/0507004`].

[80] A. Dumitru, F. Gelis, L. McLerran, and R. Venugopalan, *Glasma flux tubes and the near side ridge phenomenon at RHIC*, *Nucl.Phys.* **A810**

(2008) 91–108, [`arXiv:0804.3858`].

[81] S. Gavin and M. Abdel-Aziz, *Measuring Shear Viscosity Using Transverse Momentum Correlations in Relativistic Nuclear Collisions*, *Phys.Rev.Lett.* **97** (2006) 162302, [`nucl-th/0606061`].

[82] E. Shuryak, *On the origin of the 'Ridge' phenomenon induced by jets in heavy ion collisions*, *Phys.Rev.* **C76** (2007) 047901, [`arXiv:0706.3531`].

[83] S. Gavin, L. McLerran, and G. Moschelli, *Long Range Correlations and the Soft Ridge in Relativistic Nuclear Collisions*, *Phys.Rev.* **C79** (2009) 051902, [`arXiv:0806.4718`].

[84] J. Takahashi, B. Tavares, W. Qian, R. Andrade, F. Grassi, *et. al.*, *Topology studies of hydrodynamics using two particle correlation analysis*, *Phys.Rev.Lett.* **103** (2009) 242301, [`arXiv:0902.4870`].

[85] N. Borghini, P. M. Dinh, and J.-Y. Ollitrault, *Are flow measurements at SPS reliable?*, *Phys.Rev.* **C62** (2000) 034902, [`nucl-th/0004026`].

[86] **CMS Collaboration** Collaboration, V. Khachatryan *et. al.*, *Observation of Long-Range Near-Side Angular Correlations in Proton-Proton Collisions at the LHC*, *JHEP* **1009** (2010) 091, [`arXiv:1009.4122`].

[87] M. Luzum, *Collective flow and long-range correlations in relativistic heavy ion collisions*, *Phys.Lett.* **B696** (2011) 499–504, [`arXiv:1011.5773`].

[88] N. Borghini, P. M. Dinh, and J.-Y. Ollitrault, *Flow analysis from multiparticle azimuthal correlations*, *Phys.Rev.* **C64** (2001) 054901, [`nucl-th/0105040`].

[89] M. Miller and R. Snellings, *Eccentricity fluctuations and its possible effect on elliptic flow measurements*, `nucl-ex/0312008`.

[90] **PHOBOS Collaboration** Collaboration, B. Alver *et. al.*, *System size, energy, pseudorapidity, and centrality dependence of elliptic flow*, *Phys.Rev.Lett.* **98** (2007) 242302, [`nucl-ex/0610037`].

[91] R. Glauber, *HIGH-ENERGY COLLISION THEORY*. 1987.

[92] P. Kolb, U. W. Heinz, P. Huovinen, K. Eskola, and K. Tuominen, *Centrality dependence of multiplicity, transverse energy, and elliptic flow from hydrodynamics*, *Nucl.Phys.* **A696** (2001) 197–215,

[hep-ph/0103234].

[93] M. L. Miller, K. Reygers, S. J. Sanders, and P. Steinberg, *Glauber modeling in high energy nuclear collisions*, *Ann.Rev.Nucl.Part.Sci.* **57** (2007) 205–243, [nucl-ex/0701025].

[94] B. Alver, M. Baker, C. Loizides, and P. Steinberg, *The PHOBOS Glauber Monte Carlo*, arXiv:0805.4411.

[95] G.-Y. Qin, H. Petersen, S. A. Bass, and B. Muller, *Translation of collision geometry fluctuations into momentum anisotropies in relativistic heavy-ion collisions*, *Phys.Rev.* **C82** (2010) 064903, [arXiv:1009.1847].

[96] L. D. McLerran, *The Color glass condensate and small x physics: Four lectures*, *Lect.Notes Phys.* **583** (2002) 291–334, [hep-ph/0104285].

[97] D. Kharzeev, E. Levin, and M. Nardi, *QCD saturation and deuteron nucleus collisions*, *Nucl.Phys.* **A730** (2004) 448–459, [hep-ph/0212316].

[98] H.-J. Drescher, A. Dumitru, A. Hayashigaki, and Y. Nara, *The Eccentricity in heavy-ion collisions from color glass condensate initial conditions*, *Phys.Rev.* **C74** (2006) 044905, [nucl-th/0605012].

[99] *Viscous hydrodynamics code for relativistic heavy ion collisions. Originally by P. and U. Romatschke. Maintained by M. Luzum.*

[100] H. Song, S. A. Bass, U. Heinz, T. Hirano, and C. Shen, *200 A GeV Au+Au collisions serve a nearly perfect quark-gluon liquid*, *Phys.Rev.Lett.* **106** (2011) 192301, [arXiv:1011.2783].

[101] H. Song, S. A. Bass, U. Heinz, T. Hirano, and C. Shen, *Hadron spectra and elliptic flow for 200 A GeV Au+Au collisions from viscous hydrodynamics coupled to a Boltzmann cascade*, *Phys.Rev.* **C83** (2011) 054910, [arXiv:1101.4638].

[102] T. Hirano and Y. Nara, *Eccentricity fluctuation effects on elliptic flow in relativistic heavy ion collisions*, *Phys.Rev.* **C79** (2009) 064904, [arXiv:0904.4080].

[103] T. Hirano, P. Huovinen, and Y. Nara, *Elliptic flow in U+U collisions at* $\sqrt{s_{NN}} = 200$ *GeV and in Pb+Pb collisions at* $\sqrt{s_{NN}} = 2.76$ *TeV: Prediction from a hybrid approach*, *Phys.Rev.* **C83** (2011) 021902, [arXiv:1010.6222].

[104] **PHOBOS Collaboration** Collaboration, B. Alver *et. al.*, *Event-by-Event Fluctuations of Azimuthal Particle Anisotropy in Au + Au Collisions at $\sqrt{s_{NN}} = 200$ GeV*, *Phys.Rev.Lett.* **104** (2010) 142301, [`nucl-ex/0702036`].

[105] L. Pang, Q. Wang, and X.-N. Wang, *Effects of initial flow velocity fluctuation in event-by-event (3+1)D hydrodynamics*, *Phys.Rev.* **C86** (2012) 024911, [`arXiv:1205.5019`].

[106] R. Derradi de Souza, J. Takahashi, T. Kodama, and P. Sorensen, *Effects of initial state fluctuations in the final state elliptic flow measurements using the NeXSPheRIO model*, *Phys.Rev.* **C85** (2012) 054909, [`arXiv:1110.5698`].

[107] F. G. Gardim, F. Grassi, M. Luzum, and J.-Y. Ollitrault, *Anisotropic flow in event-by-event ideal hydrodynamic simulations of $\sqrt{s_{NN}} = 200$ GeV Au+Au collisions*, *Phys.Rev.Lett.* **109** (2012) 202302, [`arXiv:1203.2882`].

[108] Z. Qiu and U. Heinz, *Hydrodynamic event-plane correlations in Pb+Pb collisions at $\sqrt{s} = 2.76 ATeV$*, *Phys.Lett.* **B717** (2012) 261–265, [`arXiv:1208.1200`].

[109] A. Chaudhuri, *Influence of shear viscosity on the correlation between the triangular flow and initial spatial triangularity*, *Phys.Lett.* **B713** (2012) 91–94, [`arXiv:1112.1166`].

[110] H. Petersen, R. La Placa, and S. A. Bass, *A systematic study of the sensitivity of triangular flow to the initial state fluctuations in relativistic heavy-ion collisions*, *J.Phys.* **G39** (2012) 055102, [`arXiv:1201.1881`].

[111] P. Bozek and W. Broniowski, *Charge conservation and the shape of the ridge of two-particle correlations in relativistic heavy-ion collisions*, *Phys.Rev.Lett.* **109** (2012) 062301, [`arXiv:1204.3580`].

[112] T. Hirano, P. Huovinen, K. Murase, and Y. Nara, *Integrated Dynamical Approach to Relativistic Heavy Ion Collisions*, *Prog.Part.Nucl.Phys.* **70** (2013) 108–158, [`arXiv:1204.5814`].

[113] H. Holopainen and P. Huovinen, *Dynamical Freeze-out in Event-by-Event Hydrodynamics*, *J.Phys.Conf.Ser.* **389** (2012) 012018, [`arXiv:1207.7331`].

[114] S. Ryu, S. Jeon, C. Gale, B. Schenke, and C. Young, *MUSIC with the UrQMD Afterburner*, *Nucl.Phys.A904-905* **2013** (2013) 389c–392c, [`arXiv:1210.4588`].

[115] *L. D. Landau and E. M. Lifshitz. Fluid Mechanics, vol. 6 of Course of Theoretical Physics Butterworth-Heinemann, 2nd ed., Jan., 1987.*

[116] J.-Y. Ollitrault, *Relativistic hydrodynamics for heavy-ion collisions*, *Eur.J.Phys.* **29** (2008) 275–302, [`arXiv:0708.2433`].

[117] P. Romatschke, *New Developments in Relativistic Viscous Hydrodynamics*, *Int.J.Mod.Phys.* **E19** (2010) 1–53, [`arXiv:0902.3663`].

[118] M. Luzum, *Relativistic Heavy Ion Collisions: Viscous Hydrodynamic Simulations and Final State Interactions*, `arXiv:0908.4100`.

[119] P. Romatschke, *Relativistic Viscous Fluid Dynamics and Non-Equilibrium Entropy*, *Class.Quant.Grav.* **27** (2010) 025006, [`arXiv:0906.4787`].

[120] S. Sakai and A. Nakamura, *Lattice calculation of the QGP viscosities: Present results and next project*, *PoS* **LAT2007** (2007) 221, [`arXiv:0710.3625`].

[121] H. B. Meyer, *A Calculation of the bulk viscosity in SU(3) gluodynamics*, *Phys.Rev.Lett.* **100** (2008) 162001, [`arXiv:0710.3717`].

[122] F. Karsch, D. Kharzeev, and K. Tuchin, *Universal properties of bulk viscosity near the QCD phase transition*, *Phys.Lett.* **B663** (2008) 217–221, [`arXiv:0711.0914`].

[123] R. Baier, P. Romatschke, D. T. Son, A. O. Starinets, and M. A. Stephanov, *Relativistic viscous hydrodynamics, conformal invariance, and holography*, *JHEP* **0804** (2008) 100, [`arXiv:0712.2451`].

[124] M. Luzum and P. Romatschke, *Viscous Hydrodynamic Predictions for Nuclear Collisions at the LHC*, *Phys.Rev.Lett.* **103** (2009) 262302, [`arXiv:0901.4588`].

[125] K. Dusling, G. D. Moore, and D. Teaney, *Radiative energy loss and v(2) spectra for viscous hydrodynamics*, *Phys.Rev.* **C81** (2010) 034907, [`arXiv:0909.0754`].

[126] D. Teaney, *The Effects of viscosity on spectra, elliptic flow, and HBT*

radii, *Phys.Rev.* **C68** (2003) 034913, [`nucl-th/0301099`].

[127] M. Luzum and J.-Y. Ollitrault, *Constraining the viscous freeze-out distribution function with data obtained at the BNL Relativistic Heavy Ion Collider (RHIC)*, *Phys.Rev.* **C82** (2010) 014906, [`arXiv:1004.2023`].

[128] Z.-W. Lin, C. M. Ko, B.-A. Li, B. Zhang, and S. Pal, *A Multi-phase transport model for relativistic heavy ion collisions*, *Phys.Rev.* **C72** (2005) 064901, [`nucl-th/0411110`].

[129] M. Bleicher, E. Zabrodin, C. Spieles, S. Bass, C. Ernst, *et. al.*, *Relativistic hadron hadron collisions in the ultrarelativistic quantum molecular dynamics model*, *J.Phys.* **G25** (1999) 1859–1896, [`hep-ph/9909407`].

[130] J. Cleymans and D. Worku, *The Hagedorn temperature Revisited*, *Mod.Phys.Lett.* **A26** (2011) 1197–1209, [`arXiv:1103.1463`].

[131] X.-N. Wang and M. Gyulassy, *HIJING: A Monte Carlo model for multiple jet production in p p, p A and A A collisions*, *Phys.Rev.* **D44** (1991) 3501–3516.

[132] S. Bass, M. Belkacem, M. Bleicher, M. Brandstetter, L. Bravina, *et. al.*, *Microscopic models for ultrarelativistic heavy ion collisions*, *Prog.Part.Nucl.Phys.* **41** (1998) 255–369, [`nucl-th/9803035`].

[133] A. Shor and R. S. Longacre, *Effects of Secondary Interactions in Proton - Nucleus and Nucleus-nucleus Collisions Using the Hijet Event Generator*, *Phys.Lett.* **B218** (1989) 100.

[134] Y. Iga, R. Hamatsu, S. Yamazaki, and H. Sumiyoshi, *Monte Carlo Event Generator Mcmha for High-energy Hadron Nucleus Collisions and Intranuclear Cascade Interactions*, *Z.Phys.* **C38** (1988) 557–564.

[135] S. Voloshin and Y. Zhang, *Flow study in relativistic nuclear collisions by Fourier expansion of Azimuthal particle distributions*, *Z.Phys.* **C70** (1996) 665–672, [`hep-ph/9407282`].

[136] E. Retinskaya, M. Luzum, and J.-Y. Ollitrault, *Directed flow at midrapidity in* $\sqrt{s_{NN}} = 2.76$ *TeV Pb+Pb collisions*, *Phys.Rev.Lett.* **108** (2012) 252302, [`arXiv:1203.0931`].

[137] **CMS Collaboration** Collaboration, S. Chatrchyan *et. al.*, *Centrality dependence of dihadron correlations and azimuthal anisotropy harmonics*

in PbPb collisions at $\sqrt{s_{NN}} = 2.76$ *TeV*, *Eur.Phys.J.* **C72** (2012) 2012, [`arXiv:1201.3158`].

[138] F. G. Gardim, F. Grassi, M. Luzum, and J.-Y. Ollitrault, *Breaking of factorization of two-particle correlations in hydrodynamics*, *Phys.Rev.* **C87** (2013) 031901, [`arXiv:1211.0989`].

[139] U. Heinz, Z. Qiu, and C. Shen, *Fluctuating flow angles and anisotropic flow measurements*, *Phys.Rev.* **C87** (2013), no. 3 034913, [`arXiv:1302.3535`].

[140] D. Kikola, L. Yi, S. Esumi, F. Wang, and W. Xie, *Nonflow 'factorization' and a novel method to disentangle anisotropic flow and nonflow*, *Phys.Rev.* **C86** (2012) 014901, [`arXiv:1110.4809`].

[141] **ALICE Collaboration** Collaboration, K. Aamodt *et. al.*, *Production of pions, kaons and protons in pp collisions at* $\sqrt{s} = 900$ *GeV with ALICE at the LHC*, *Eur.Phys.J.* **C71** (2011) 1655, [`arXiv:1101.4110`].

[142] **STAR Collaboration** Collaboration, B. Abelev *et. al.*, *Strange particle production in p+p collisions at s**(1/2) = 200-GeV*, *Phys.Rev.* **C75** (2007) 064901, [`nucl-ex/0607033`].

[143] A. Toia, *Bulk Properties of Pb-Pb collisions at* $\sqrt{s_{NN}} = 2.76$ *TeV measured by ALICE*, *J.Phys.* **G38** (2011) 124007, [`arXiv:1107.1973`].

[144] P. F. Kolb and U. W. Heinz, *Hydrodynamic description of ultrarelativistic heavy ion collisions*, `nucl-th/0305084`.

[145] D. Teaney and L. Yan, *Non linearities in the harmonic spectrum of heavy ion collisions with ideal and viscous hydrodynamics*, *Phys.Rev.* **C86** (2012) 044908, [`arXiv:1206.1905`].

[146] *Azhydro version 0.2.*

[147] T. Epelbaum and F. Gelis, *Pressure isotropization in high energy heavy ion collisions*, *Phys.Rev.Lett.* **111** (2013) 232301, [`arXiv:1307.2214`].

[148] P. Kovtun, D. T. Son, and A. O. Starinets, *Viscosity in strongly interacting quantum field theories from black hole physics*, *Phys.Rev.Lett.* **94** (2005) 111601, [`hep-th/0405231`].

[149] E. Retinskaya, M. Luzum, and J.-Y. Ollitrault, *Constraining models of initial conditions with elliptic and triangular flow data*, *Phys.Rev.* **C89**

(2014) 014902, [`arXiv:1311.5339`].

[150] E. Retinskaya, M. Luzum, and J.-Y. Ollitrault, *Constraining models of initial state with v_2 and v_3 data from LHC and RHIC*, `arXiv:1401.3241`.

[151] H. Holopainen, H. Niemi, and K. J. Eskola, *Event-by-event hydrodynamics and elliptic flow from fluctuating initial state*, *Phys.Rev.* **C83** (2011) 034901, [`arXiv:1007.0368`].

[152] H. Petersen, G.-Y. Qin, S. A. Bass, and B. Muller, *Triangular flow in event-by-event ideal hydrodynamics in Au+Au collisions at $\sqrt{s_{\rm NN}} = 200A$ GeV*, *Phys.Rev.* **C82** (2010) 041901, [`arXiv:1008.0625`].

[153] R. S. Bhalerao, M. Luzum, and J.-Y. Ollitrault, *Determining initial-state fluctuations from flow measurements in heavy-ion collisions*, *Phys.Rev.* **C84** (2011) 034910, [`arXiv:1104.4740`].

[154] J. L. Albacete and A. Dumitru, *A model for gluon production in heavy-ion collisions at the LHC with rcBK unintegrated gluon densities*, `arXiv:1011.5161`.

[155] *Code by A. Dumitru, a fork of MC-KLN by Y. Nara. Versions 1.00 and 1.25.*

[156] C. Flensburg, *Correlations and Fluctuations in the Initial State of high energy Heavy Ion Collisions*, `arXiv:1108.4862`.

[157] A. Dumitru and Y. Nara, *KNO scaling of fluctuations in pp and pA, and eccentricities in heavy-ion collisions*, *Phys.Rev.* **C85** (2012) 034907, [`arXiv:1201.6382`].

[158] P. Bozek, M. Chojnacki, W. Florkowski, and B. Tomasik, *Hydrodynamic predictions for Pb+Pb collisions at $\sqrt{S_{NN}}$ = 2.76 TeV*, *Phys.Lett.* **B694** (2010) 238–241, [`arXiv:1007.2294`].

[159] **STAR Collaboration** Collaboration, K. Ackermann *et. al.*, *Elliptic flow in Au + Au collisions at (S(NN))**(1/2) = 130 GeV*, *Phys.Rev.Lett.* **86** (2001) 402–407, [`nucl-ex/0009011`].

[160] **PHENIX Collaboration** Collaboration, A. Adare *et. al.*, *Measurements of Higher-Order Flow Harmonics in Au+Au Collisions at $\sqrt{s_{NN}} = 200$ GeV*, *Phys.Rev.Lett.* **107** (2011) 252301, [`arXiv:1105.3928`].

[161] N. Borghini, P. M. Dinh, and J.-Y. Ollitrault, *A New method for measuring azimuthal distributions in nucleus-nucleus collisions*, *Phys.Rev.* **C63** (2001) 054906, [`nucl-th/0007063`].

[162] N. Borghini and J.-Y. Ollitrault, *Momentum spectra, anisotropic flow, and ideal fluids*, *Phys.Lett.* **B642** (2006) 227–231, [`nucl-th/0506045`].

[163] F. G. Gardim, F. Grassi, M. Luzum, and J.-Y. Ollitrault, *Mapping the hydrodynamic response to the initial geometry in heavy-ion collisions*, *Phys.Rev.* **C85** (2012) 024908, [`arXiv:1111.6538`].

[164] D. Teaney and L. Yan, *Plane correlations and hydrodynamic simulations of heavy ion collisions*, `arXiv:1312.3689`.

[165] H. Niemi, G. Denicol, H. Holopainen, and P. Huovinen, *Event-by-event distributions of azimuthal asymmetries in ultrarelativistic heavy-ion collisions*, *Phys.Rev.* **C87** (2013) 054901, [`arXiv:1212.1008`].

[166] C. Gale, S. Jeon, and B. Schenke, *Hydrodynamic Modeling of Heavy-Ion Collisions*, *Int.J.Mod.Phys.* **A28** (2013) 1340011, [`arXiv:1301.5893`].

[167] M. Luzum and J.-Y. Ollitrault, *Extracting the shear viscosity of the quark-gluon plasma from flow in ultra-central heavy-ion collisions*, *Nucl.Phys.* **A904-905** (2013) 377c–380c, [`arXiv:1210.6010`].

[168] R. Soltz, I. Garishvili, M. Cheng, B. Abelev, A. Glenn, *et. al.*, *Constraining the initial temperature and shear viscosity in a hybrid hydrodynamic model of $\sqrt{s_{NN}}$=200 GeV Au+Au collisions using pion spectra, elliptic flow, and femtoscopic radii*, *Phys.Rev.* **C87** (2013), no. issue 044901, [`arXiv:1208.0897`].

[169] H. B. Meyer, *A Calculation of the shear viscosity in SU(3) gluodynamics*, *Phys.Rev.* **D76** (2007) 101701, [`arXiv:0704.1801`].

[170] H. Song, *QGP viscosity at RHIC and the LHC - a 2012 status report*, *Nucl.Phys.* **A904-905** (2013) 114c–121c, [`arXiv:1210.5778`].

[171] K. Dusling and D. Teaney, *Simulating elliptic flow with viscous hydrodynamics*, *Phys.Rev.* **C77** (2008) 034905, [`arXiv:0710.5932`].

[172] K. Dusling and T. Schoefer, *Bulk viscosity, particle spectra and flow in heavy-ion collisions*, *Phys.Rev.* **C85** (2012) 044909, [`arXiv:1109.5181`].

[173] P. Bozek, *Bulk and shear viscosities of matter created in relativistic*

heavy-ion collisions, *Phys.Rev.* **C81** (2010) 034909, [`arXiv:0911.2397`].

[174] G. Denicol, T. Kodama, T. Koide, and P. Mota, *Effect of bulk viscosity on Elliptic Flow near QCD phase transition*, *Phys.Rev.* **C80** (2009) 064901, [`arXiv:0903.3595`].

[175] M. Gyulassy, Y. Sinyukov, I. Karpenko, and A. Nazarenko, *HBT and initial conditions for hydrodynamic expansion in A + A collisions*, *Braz.J.Phys.* **37** (2007) 1031–1038.

[176] W. Broniowski, M. Chojnacki, W. Florkowski, and A. Kisiel, *Uniform Description of Soft Observables in Heavy-Ion Collisions at s(NN)**(1/2) = 200 GeV**2*, *Phys.Rev.Lett.* **101** (2008) 022301, [`arXiv:0801.4361`].

[177] S. Pratt, *Resolving the HBT Puzzle in Relativistic Heavy Ion Collision*, *Phys.Rev.Lett.* **102** (2009) 232301, [`arXiv:0811.3363`].

[178] J. Vredevoogd and S. Pratt, *Universal Flow in the First Stage of Relativistic Heavy Ion Collisions*, *Phys.Rev.* **C79** (2009) 044915, [`arXiv:0810.4325`].

[179] T. Hirano, U. W. Heinz, D. Kharzeev, R. Lacey, and Y. Nara, *Hadronic dissipative effects on elliptic flow in ultrarelativistic heavy-ion collisions*, *Phys.Lett.* **B636** (2006) 299–304, [`nucl-th/0511046`].

[180] H. Song, S. A. Bass, and U. Heinz, *Elliptic flow in 200 A GeV Au+Au collisions and 2.76 A TeV Pb+Pb collisions: insights from viscous hydrodynamics + hadron cascade hybrid model*, *Phys.Rev.* **C83** (2011) 054912, [`arXiv:1103.2380`].

[181] A. Monnai and T. Hirano, *Effects of Bulk Viscosity at Freezeout*, *Phys.Rev.* **C80** (2009) 054906, [`arXiv:0903.4436`].

[182] D. Teaney and L. Yan, *Second order viscous corrections to the harmonic spectrum in heavy ion collisions*, *Phys.Rev.* **C89** (2014) 014901, [`arXiv:1304.3753`].

[183] W. Broniowski, M. Rybczynski, and P. Bozek, *GLISSANDO: Glauber initial-state simulation and more..*, *Comput.Phys.Commun.* **180** (2009) 69–83, [`arXiv:0710.5731`].

[184] M. Rybczynski, G. Stefanek, W. Broniowski, and P. Bozek, *GLISSANDO 2: GLauber Initial-State Simulation AND mOre..., ver. 2*, `arXiv:1310.5475`.

[185] H.-J. Drescher and Y. Nara, *Eccentricity fluctuations from the color glass condensate at RHIC and LHC*, *Phys.Rev.* **C76** (2007) 041903, [`arXiv:0707.0249`].

[186] B. Schenke, P. Tribedy, and R. Venugopalan, *Event-by-event gluon multiplicity, energy density, and eccentricities in ultrarelativistic heavy-ion collisions*, *Phys.Rev.* **C86** (2012) 034908, [`arXiv:1206.6805`].

[187] R. S. Bhalerao, M. Luzum, and J.-Y. Ollitrault, *Understanding anisotropy generated by fluctuations in heavy-ion collisions*, *Phys.Rev.* **C84** (2011) 054901, [`arXiv:1107.5485`].

[188] **PHENIX Collaboration** Collaboration, K. Adcox *et. al.*, *Flow measurements via two particle azimuthal correlations in Au+Au collisions at s(NN)**(1/2) = 130-GeV*, *Phys.Rev.Lett.* **89** (2002) 212301, [`nucl-ex/0204005`].

[189] **ATLAS Collaboration** Collaboration, G. Aad *et. al.*, *Measurement of event-plane correlations in* $\sqrt{s_{NN}}$*=2.76 TeV lead-lead collisions with the ATLAS detector*, `arXiv:1403.0489`.

[190] B. Alver, B. Back, M. Baker, M. Ballintijn, D. Barton, *et. al.*, *Importance of correlations and fluctuations on the initial source eccentricity in high-energy nucleus-nucleus collisions*, *Phys.Rev.* **C77** (2008) 014906, [`arXiv:0711.3724`].

[191] A. M. Poskanzer and S. Voloshin, *Methods for analyzing anisotropic flow in relativistic nuclear collisions*, *Phys.Rev.* **C58** (1998) 1671–1678, [`nucl-ex/9805001`].

[192] J.-Y. Ollitrault, A. M. Poskanzer, and S. A. Voloshin, *Effect of flow fluctuations and nonflow on elliptic flow methods*, *Phys.Rev.* **C80** (2009) 014904, [`arXiv:0904.2315`].

[193] M. Luzum and J.-Y. Ollitrault, *Eliminating experimental bias in anisotropic-flow measurements of high-energy nuclear collisions*, *Phys.Rev.* **C87** (2013), no. 4 044907, [`arXiv:1209.2323`].

[194] **STAR Collaboration** Collaboration, C. Adler *et. al.*, *Elliptic flow from two and four particle correlations in Au+Au collisions at s(NN)**(1/2) = 130-GeV*, *Phys.Rev.* **C66** (2002) 034904, [`nucl-ex/0206001`].

[195] H.-J. Drescher, A. Dumitru, C. Gombeaud, and J.-Y. Ollitrault, *The*

Centrality dependence of elliptic flow, the hydrodynamic limit, and the viscosity of hot QCD, *Phys.Rev.* **C76** (2007) 024905, [`arXiv:0704.3553`].

[196] D. Teaney and L. Yan *From the private discussion.*